MYOCARDIAL ISCHEMIA WITHOUT OBSTRUCTIVE CORONARY ARTERY DISEASE: PERFUSION MRI IN MOUSE MODELS

A Dissertation

Presented to the Faculty of

The School of Engineering and Applied Science

University of Virginia

In Partial Fulfillment

Of the Requirements for the Degree of

Doctor of Philosophy in Biomedical Engineering

NIVEDITA K. NARESH

DECEMBER 2014

APPROVAL SHEET

The dissertation

Is submitted in partial fulfillment of the requirements

For the degree of

Doctor of Philosophy

K. N. Nivedita

Author

The dissertation has been read and approved by the examining committee:

Frederick H. Epstein, Ph.D.
Advisor

Brent A. French, Ph.D.

Craig H. Meyer, Ph.D.

Jeffery W. Holmes, M.D., Ph.D.

Christopher M. Kramer, M.D.

Brian H. Annex, M.D.

Accepted for the School of Engineering and Applied Science

James H. Ayl

Dean, School of Engineering and Applied Science

December 2014

Abstract

Cardiovascular disease is the leading health disorder in the western world. Recent studies have shown that myocardial ischemia can occur even in the absence of obstructive coronary artery disease (CAD) and this is especially common in patient populations of women, diabetics, patients of metabolic syndrome and obesity. An emerging concept in this realm is abnormal myocardial perfusion reserve as quantified by non-invasive imaging, or the inadequate increase of myocardial blood flow in response to vasodilation. Impaired myocardial perfusion reserve is associated with adverse cardiovascular outcomes even in the absence of obstructive CAD. Furthermore, increased body weight is independently associated with impaired myocardial perfusion reserve. However, molecular mechanisms underlying impaired myocardial perfusion reserve in the absence of obstructive CAD in are still unclear.

Mice are widely used as models to study cardiovascular diseases and research using genetically modified mice has provided tremendous insights into the cellular and molecular mechanisms that underlie many cardiovascular diseases. Currently, no mouse model of ischemia in the absence of obstructive CAD has been established. Thus, it would be extremely useful to develop a mouse model that parallels the human clinical scenario, i.e. a mouse model of non-obstructive inducible myocardial ischemia in order to study causal mechanisms and eventually to develop therapies aimed at improving patient outcomes.

For this dissertation, Specific Aim 1 is to develop improved quantitative perfusion MRI methods for mice to measure myocardial perfusion reserve and to test the

hypothesis that these methods can detect impaired myocardial perfusion reserve in mice fed a high-fat diet. Specific Aim 2 is to compare the two perfusion MRI techniques: first-pass contrast enhanced MRI and arterial spin labeling in terms of repeatability and user variability. Specific Aim 3 is to use cardiac MRI to establish the time course of impaired myocardial perfusion reserve and left-ventricular hypertrophy in a mouse model of diet-induced obesity.

Acknowledgements

experiments in the high-fat diet mouse model (Chapter 4). I want to thank Dr. Joshua Butcher from the Isakson lab for performing the vascular reactivity studies for the project using the high-fat diet mouse model. My post-MI imaging experiments would have been impossible without the expert surgical skills of Dr. Yaqin (Carolyne) Xu and Dr. Yikui Tian (Jarod) from the French lab. I would also like to thank Joe Dimaria for his help and expertise in acquiring non-invasive blood pressure measurements in mice.

I am very thankful to Dr. Moriel Vandsburger, who has been a great friend. He also taught me mouse imaging with great patience, even when I used to jump every time the mouse moved. I am extremely grateful to Dr. Xiao Chen for all his help and expertise with compressed sensing image reconstruction. I learnt a lot about first-pass perfusion imaging and about perfusion modeling from Dr. Patrick Antkowiak, which has been very useful. Bhairav Mehta has been a great help over the past many years and I have had wide discussions with him regarding MR acquisition and image reconstruction, which has been extremely useful. Additional thanks to Dr. Daniel Auger, Xiaoying Cai and Xinyuan (Sophia) Cui for their support, encouragement and for making lab a fun place.

Finally, last but definitely not the least I would like to thank my family and friends. My parents have always encouraged me and no words can express my gratitude for their unconditional love and support throughout my life. My father and mother have always been an inspiration to me and they have been a huge positive influence on my educational and career choices. I am extremely grateful to Kaushik, who has been very kind, understanding, caring and has always been there when I needed someone to talk to. He has provided endless encouragement and has made life in Charlottesville much

more meaningful and enjoyable. I have also had a number of amazing roommates and friends in Charlottesville and they have been my second family. I greatly appreciate all the fun get-togethers, dinners, game nights, movie nights, trips, rides to airports, phone-calls, e-mails and general help, advice, support and friendship, which has truly enriched my life.

Table of Contents

CHAPTER 3: REPEATABILITY AND VARIABILITY OF PERFUSION IMAGING TECHNIQUES: FIRST-PASS MRI AND ASL IN MICE

List of Figures

Abbreviations and Symbols

CAD   Coronary artery disease

MBF   Myocardial blood flow

PET   Positron emission tomography

MRI   Magnetic resonance imaging

IHD   Ischemic heart disease

CTA   Computed tomography angiography

SPECT   Single-photon emission computed tomography

BMI   Body-to-mass index

LV   Left ventricular

MPR   Myocardial Perfusion Reserve

NMR   Nuclear magnetic resonance

RF   Radiofrequency

Gd   Gadolinium

AIF   Arterial input function

TF   Tissue function

ASL   Arterial spin labeling

FAIR   Flow-sensitive alternating inversion recovery

GLUT4   Glucose transporter subtype 4

PPAR   Peroxisome proliferator-activated receptor

CMR   Cardiac magnetic resonance

MI   Myocardial infarction

HARP   Harmonic phase

DENSE   Displacement-encoded imaging with stimulated echoes

E_{cc} Circumferential strain

CS   Compressed sensing

HFD   High-fat diet

DIO   Diet-induced obesity

BLOSM   Block low-rank sparsity with motion-guidance

k-t SLR   k-t sparsity and low-rank

GTT   Glucose-tolerance test

ROI   Region of interest

FFT   Fast fourier transform

CRG   Cardio-respiratory gated

SS   Slice-selective

NS   Non-selective

RC   Repeatability coefficient

CV   Coefficient of variability

SEM   Standard error of mean

IQ   Image quality

EDV   End-diastolic volume

ESV   End-systolic volume

EF   Ejection fraction

LVEDWT   LV wall thickness at end-diastole

LVESWT   LV wall thickness at end-systole

AUC   Area under the curve

FOV   Field of view

ARB   Angiotensin II type 1 receptor blocker

Chapter 1: Introduction

1.1. Coronary Artery Disease

Coronary artery disease (CAD) is the leading cause of death in the United States, affecting more than 13 million people. Coronary arteries are the major blood vessels that supply blood and oxygen to the heart muscle. CAD is characterized by atherosclerosis of the coronary arteries. Atherosclerosis refers to the build-up of cholesterol containing deposits (plaques) in arteries. Atherosclerotic plaques progressively narrow the coronary artery lumen and impair blood flow to the heart when under stress. The following figure is from a study by Di Carli *et al.* (1) and it shows the relationship between severity of stenosis and myocardial blood flow (MBF) at rest and after injection of a vasodilator (stress agent). It has been shown that, in regions supplied by minimally stenosed arteries where the stenosis is less than 50%, the MBF at rest and stress is similar to age-matched healthy volunteers. However, as can be seen from Figure 1.1, with increasing severity of the stenosis, stress MBF decreased while there were no changes in rest MBF even in regions where the stenosis was greater than 90%. In this study, MBF was measured using positron emission tomography (PET). In a more recent study, similar results were shown using quantitative perfusion magnetic resonance imaging (MRI) (2). Thus, in obstructive CAD, myocardial ischemia (impaired MBF) is observed at stress while baseline or resting MBF is normal. Due to this, in clinical practice, the earlier perception was that ischemic heart disease (IHD) and CAD are essentially equivalent or synonymous and that IHD is caused by CAD (3).
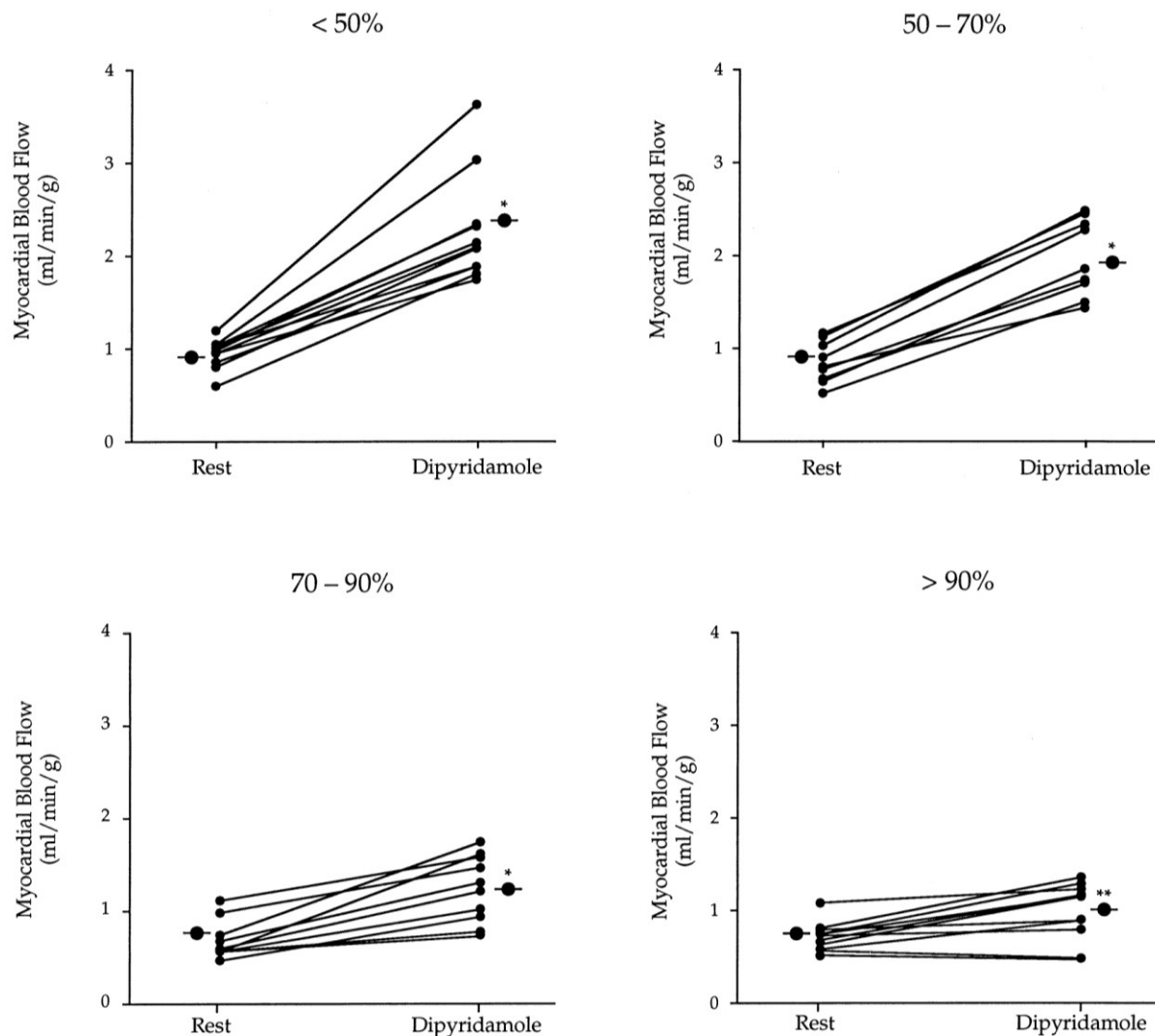
Figure 1.1: Relationship of myocardial blood flow with severity of stenosis. This figure shows changes in myocardial blood flow after dipyridamole in each coronary territory grouped by cross-sectional area of stenosis (i.e., <50%, 50% to 70%, 70% to 90%, >90%). *P<.001, **P<.05 vs. baseline myocardial blood flows. Image reprinted with permission from Di Carli M *et al.* (1).

1.2. Ischemic Heart Disease and Non-obstructive Coronary Artery Disease

Since the earlier thinking was that myocardial ischemia and obstructive CAD are one and the same, the treatment of cardiac ischemia is currently centered on the removal of coronary artery stenosis (3). However, there is mounting evidence that not all patients with obstructive CAD have ischemia and not all patients with ischemia have obstructive CAD (3). A recent study (4) showed that out of 163 symptomatic patients with chest pain who underwent both computed tomography angiography (CTA) and single-photon emission computed tomography (SPECT) for ischemia, 39 had obstructive and 105 had non-obstructive lesions. Due to the mounting evidence, a paradigm shift has been proposed for ischemic heart disease: one that takes all the factors responsible for myocardial ischemia into account (Figure 1.2) (3). An emerging concept is that several factors such as microvascular dysfunction, endothelial dysfunction, thrombosis, inflammation and coronary vasospasm are significant contributors to myocardial ischemia and that obstructive CAD is just one contributing factor (3) and this is illustrated in Figure 1.2. Myocardial ischemia in the absence of obstructive CAD is especially common in patient populations of women (5), diabetics (6), patients with metabolic syndrome (7) and patients with obesity (8). Thus, in order to advance heart therapies in patients, it is essential to put more emphasis on assessing microvasculature with resultant myocardial ischemia rather than just detecting obstructive CAD.
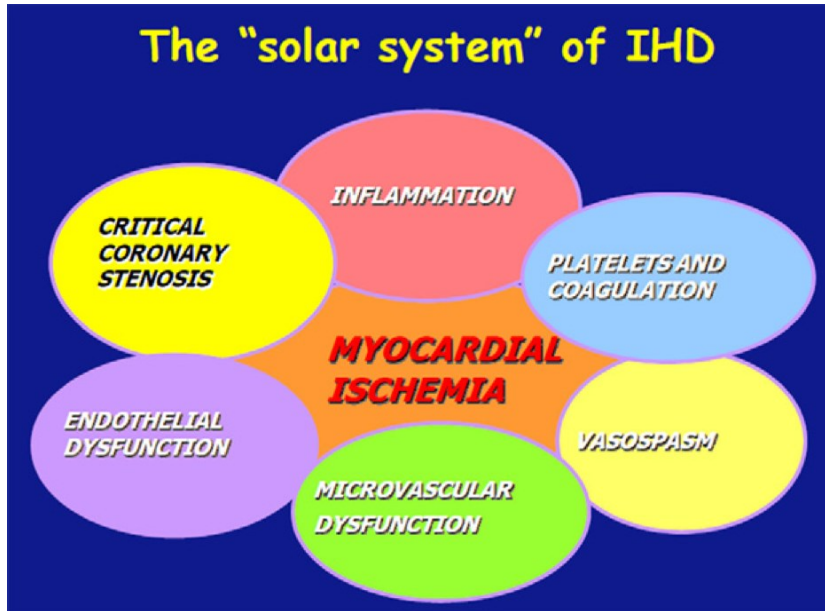
Figure 1.2: Proposed paradigm shift in ischemic heart disease. Critical coronary stenosis is just one factor responsible for myocardial ischemia. Several other factors are responsible for myocardial ischemia such as inflammation, microvascular dysfunction, endothelial dysfunction, vasospasm and platelets and coagulation. Image reprinted with permission from Marzilli *et al.* (3).

1.3. Obesity

1.3.1. Prevalence and Mortality

Obesity is a growing epidemic worldwide in both adults and children. In adults, obesity and overweight ranges are defined using body-to-mass index (BMI), which is determined using the height and weight of an individual. Any person with a BMI between 25 and 29.9 is considered overweight and any individual with a BMI greater or

equal to 30 is considered obese. In children and adolescents, overweight is defined as a BMI at or above 85th percentile and lower than 95th percentile for children of the same age and sex (9) and obesity is defined as a BMI at or above the 95th percentile for children of the same age and sex (9). According to a recent comprehensive global study published in the Lancet, more than one-third of the adult world population is either overweight or obese and about 8-10 % of the adults worldwide are obese (10). Furthermore, they also showed that the combined prevalence of overweight and obesity in children worldwide is about 13-14%. In United States alone, about 60-70% of men and women are either overweight or obese and the prevalence of obesity alone in adults is about 33% (10). In children and adolescents in the United States, about 30% are either overweight or obese and about 12-13 % are obese (10).

A recent study performed a systematic review and meta-analysis of associations between all-cause mortality and overweight and obesity defined using the standard BMI categories. Obesity was further split into different grades based on BMI (grade 1 was defined as BMI of 30-35, grade 2 = 35-40 and grade 3 > 40). Using rigorous selection criteria for inclusion of studies, the sample included more than 2.88 million individuals and more than 270,000 deaths. They showed that overall obesity (including all grades) was associated with significantly higher all-cause mortality in comparison to normal weight (11). Another recent study has shown that obesity is also associated with increased cardiovascular death (12).

1.3.2. Obesity and cardiomyopathy

In the past, obesity cardiomyopathy was defined as congestive heart failure primarily due to obesity and it was uniquely associated with morbidly obese individuals. However, there has been increasing evidence showing changes in cardiac structure and function in mildly to moderately obese individuals (13). Hence there have been calls to extend the definition of obesity cardiomyopathy to include myocardial disease in obese individuals that cannot be explained by diabetes milletus, hypertension, coronary artery disease or other etiologies (13).

The possible link between obesity and heart failure was first recognized in 1933 by Smith and Willius (14). Later in 1965, Amad *et al.* (15) reported post-mortem findings in 12 extremely obese individuals, which primarily included increased heart weight and left-ventricular (LV) wall thickness. Another study in 1983 (16) first recognized obesity as an independent risk factor for cardiovascular disease in both men and women. A number of epidemiological studies have provided evidence to link obesity with heart failure outcomes (13). A recent Framingham study (17) investigated the association between BMI and the incidence of heart failure and they showed that for each unit increment in BMI, the risk of heart failure increased by 5% in men and 7% in women after adjustment for established risk factors and this is illustrated in Figure 1.3.

A

No. at Risk							
Normal	1729	1688	1634	1568	1477	1227	295
Overweight	955	929	880	815	757	634	248
Obese	493	477	448	409	372	296	104

B

No. at Risk							
Normal	869	822	758	690	637	512	105
Overweight	1378	1322	1254	1163	1071	871	171
Obese	457	433	403	370	342	276	51
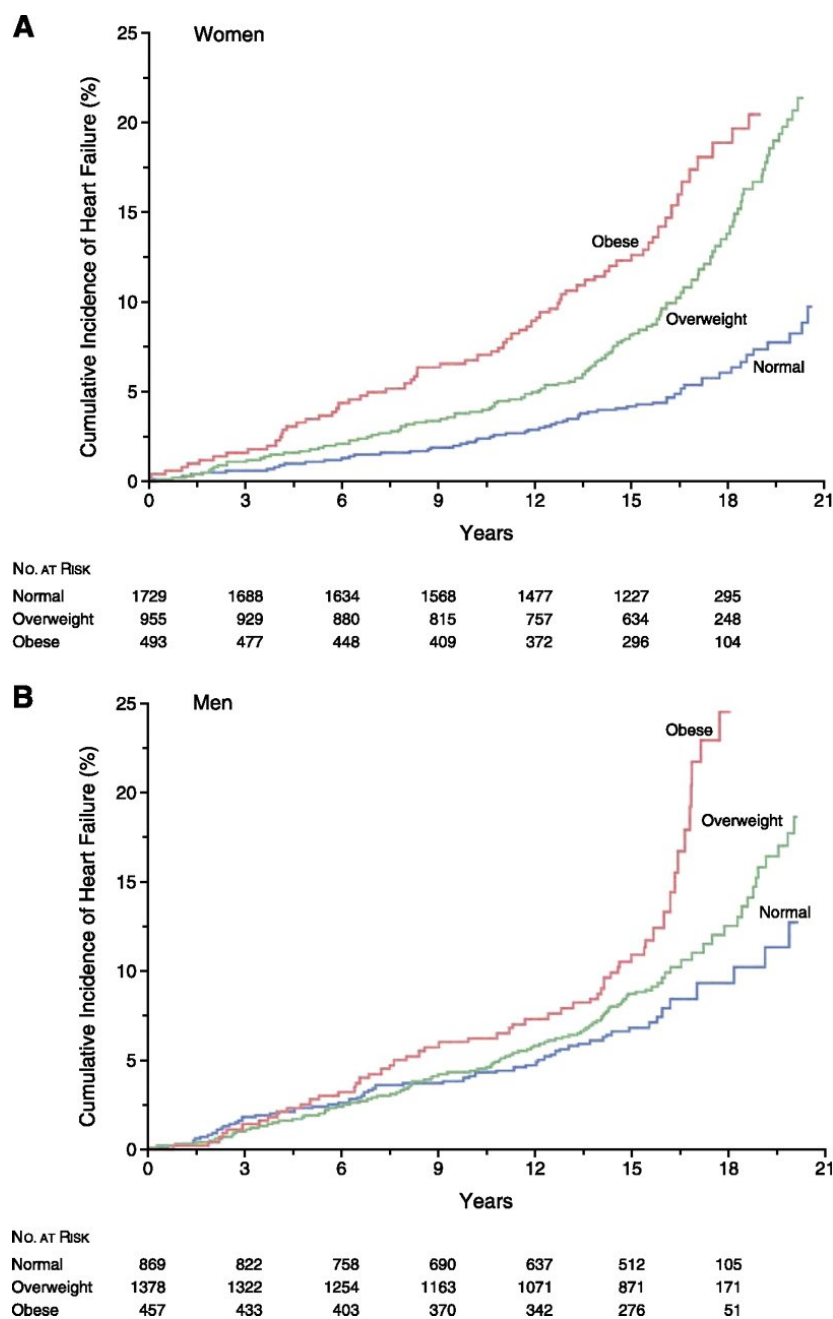
Figure 1.3: Obesity and the risk of heart failure. This figure shows the cumulative incidence of heart failure according to the category of body mass index (BMI) in both men and women. Subjects with BMI between 18.5 and 24.9 were classified as normal, BMI between 25 and 29.9 were classified as overweight and BMI above 30 were classified as obese. Image reprinted with permission from Kenchaiah *et al.* (17).

Obesity produces numerous structural and functional changes in the heart. The structural changes in the heart due to obesity include increased LV mass, increased LV wall thickness, LV dilatation, myocyte hypertrophy, increased lipid accumulation in the heart and some myocardial fibrosis (18). Obese individuals have been shown to primarily have concentric hypertrophy but some studies have also reported eccentric hypertrophy in obese individuals (18). The findings of systolic and diastolic function in obesity are variable. While some studies report normal ejection fraction and diastolic function in obese patients, a few studies have demonstrated subclinical contractile abnormalities and prolonged isovolumetric relaxation time in obese patients. Vascular dysfunction and endothelial dysfunction is also thought to be associated with obesity (18).

1.3.3. Potential Mechanisms

Several mechanisms have been implicated in obesity related cardiomyopathy such as increased haemodynamic load, insulin resistance, lipotoxicity, inflammation, interstitial fibrosis, altered cardiac substrate metabolism, mitochondrial dysfunction and increased cardiac oxidative stress (18,19). It has been shown using animal models of obesity that in obesity, one of the earliest changes is the shift in myocardial substrate utilization from glucose oxidation to fatty acid oxidation, probably due to increased availability of fatty acids in obese hearts (20). Increased exposure of fatty acids is thought to cause uncoupling of mitochondria, which may contribute to the shift in cardiac substrate utilization, reduction in cardiac efficiency and impaired myocardial energetics. Despite increased oxidation of fatty acids, there is accumulation of

triglycerides in obese hearts and this combined with mitochondrial dysfunction leads to increased lipid burden in the heart, which could ultimately lead to cardiac dysfunction (21). Neurohumoral factors may also play a role in obesity related cardiomyopathy. It has been shown that there is increased activation of renin angiotensin system in obesity (22) and that this may contribute to cardiac hypertrophy. Inflammation is also linked with obesity and inflammatory cytokines may also lead to hypertrophy.

1.4.   Perfusion Imaging and Ischemic Heart Disease

The conventional diagnostic technique for IHD is coronary angiography. However, coronary angiography is an invasive technique and it is not readily used to examine the function of microvasculature. Myocardial perfusion imaging is a well-established tool to non-invasively assess blood flow to the heart and is also commonly used to diagnose CAD. Myocardial perfusion reserve (MPR) is the amount by which myocardial perfusion increases during maximal coronary vasodilation. MPR is defined as the ratio of MBF at baseline to MBF at maximal hyperemia, which can be achieved by intravenous injection of vasodilator adenosine or Regadenoson. Since the coronary arterioles primarily determine coronary vascular resistance, in the absence of obstructive CAD, MPR assesses the function of the small blood vessels (coronary vascular function) and it is a sensitive indicator of the capacity of the coronary circulation to supply oxygen to the myocardium. An impaired MPR thus, is a surrogate marker of myocardial ischemia (23). In the presence of obstructive CAD, MPR is a measure of the severity of the stenosis (1,24-27). However, it can also occur in the

absence of obstructive CAD (28-31), where it is a marker of coronary vascular dysfunction. Reduced MPR as measured by PET has been shown to be prognostic of adverse cardiovascular outcomes and is an independent predictor of cardiac mortality in patients with known or suspected CAD (24). Abnormal coronary vascular function in the absence of obstructive CAD is especially common in patient populations of women (32), diabetics (6) and patients with metabolic syndrome (7).

1.4.1. Quantitative Perfusion Imaging in Ischemic Heart Disease

Myocardial perfusion can be assessed either qualitatively or quantitatively. Qualitative or semi-quantitative assessment of myocardial perfusion however has reduced sensitivity for detecting perfusion defects in patients with multi-vessel CAD or microvascular disease (33). MPR, which is obtained using fully quantitative perfusion imaging, is an independent predictor of cardiac mortality and can also be used to detect microvascular dysfunction in women, diabetics, and patients of metabolic syndrome in the absence of non-obstructive CAD. Hence, there is a growing interest to quantify MBF. Additionally, quantitative assessments of myocardial perfusion enable the clinicians to accurately and objectively assess the injury to the myocardium.

Various modalities may be used to image the functional response of the myocardium such as single-photon emission computed tomography (SPECT), echocardiography, positron-emission tomography (PET) and magnetic resonance imaging (MRI). SPECT is widely available, however, SPECT has poor spatial resolution, soft-tissue attenuation artifacts, requires a significant dose of ionizing radiation and it is not truly quantitative (34). Echocardiography can also be used to detect perfusion with

no ionizing radiation. However, it has limited acoustic windows and it is not quantitative. PET overcomes some of the shortcomings of SPECT as it has a higher spatial resolution, eliminates attenuation artifacts and provides a quantitative assessment of perfusion. Currently, PET is the gold standard for non-invasive quantification of myocardial blood flow. However, it uses radioactive tracers, which can be potentially harmful, and the availability of PET is limited to sites with a cyclotron for providing short half-life radiotracers. Thus, MRI has advantages as compared to the other imaging modalities, most notably high spatial resolution as well as absolute quantification of myocardial blood flow (34).

1.4.2. MRI

Magnetic Resonance Imaging (MRI) was invented in the 1970s and is based on the principles nuclear magnetic resonance (NMR). In brief, MRI utilizes the magnetic properties possessed by certain atoms to create high-resolution images. Atoms with odd number of protons or neutrons possess a magnetic moment. Hydrogen (^{1}H), for example is composed of one proton and hence possesses a magnetic moment. Approximately 60% of an average adult human body is composed of water, which in turn is made up of hydrogen atoms. Normally, the magnetic moments of the hydrogen nuclei in the body are randomly oriented. However, when the human body is placed in an external magnetic field (B_0), the magnetic moments of the hydrogen nuclei align along the direction of the external magnetic field. Slightly more than half of the magnetic moments align parallel to B_0 and the remaining align antiparallel to B_0. Thus, the sum total of the magnetic moments, also called the net magnetization is aligned parallel to B_0

and this contributes to the MRI signal. The net magnetization precesses around the direction of the external magnetic field (also known as the longitudinal direction) with a frequency known as the Larmor frequency. Thereafter, a radio frequency (RF) pulse tuned at the resonant frequency (Larmor frequency) is applied in the transverse plane, which transfers energy to the magnetic moments in the body, and this tips the net magnetization to the transverse plane. After the transmitting RF pulse is switched off, the net magnetization returns to its resting state or equilibrium state (along longitudinal direction) by emitting energy, which is then detected by receiver coils and used to construct MR images. Furthermore, gradient coils are used to spatially encode the positions of the nuclei by varying the magnetic field linearly, thereby causing the nuclei at different positions to precess with different frequencies. T_1 is the time-constant governing the exponential recovery of longitudinal magnetization. When the tipped spins precess about B_0, they dephase due to interactions with nearby protons and the transverse magnetization decays. T_2 is the time-constant governing the exponential decay of the transverse magnetization. Since each tissue has a distinct intrinsic T_1 and T_2 relaxation value, the imaging protocol can be altered to enhance contrast and emphasize a particular tissue. Additionally, pathologies also alter the relaxation rates of a tissue and this can be further exploited to distinguish pathological tissues from normal tissues.

1.4.2.1.   Quantitative Perfusion MRI

Perfusion is the rate of blood flow to the capillary bed in a tissue per unit gram tissue. Perfusion in MRI can be quantified by two different techniques – first-pass contrast enhanced MRI and arterial spin labeling.

(a) First-pass contrast-enhanced MRI:

In this technique, a bolus of MR detectable tracer such as gadolinium (Gd) chelate is injected intravenously and its first pass through the chambers of the heart is detected. First-pass contrast-enhanced MRI is typically performed using a dynamic T1-weighted pulse sequence following the injection of a bolus of contrast agent to visualize its transit through the tissue. A set of T1-weighted images is acquired starting before the bolus injection and continuing while the contrast agent washes into and out from the tissue. The term first-pass refers to the first passage of the bolus of contrast agent through the heart. The contrast agent Gd-DTPA, which is typically used for these studies, is injected intravenously due to which it first appears in the right ventricle. Thereafter it passes through the lungs and then reaches the left ventricle, thereby causing signal enhancement in the LV blood pool. After a short delay, it enters the myocardium.

The pulse sequences used for first-pass MRI are typically cardiac gated and consist of magnetization preparation followed by the image readout. The magnetization preparation can be a saturation or inversion preparation. However, inversion recovery is sensitive to heart rate variations, due to which saturation recovery is the current standard (34). The saturation preparation is implemented using an adiabatic non-

selective 90^0 RF pulse. Typically, there is a delay between the magnetization preparation and image readout, which controls the T1 weighting of the first-pass images. For the image readout, typically fast imaging is used to minimize corruption of images due to motion. Acceleration techniques are also used to further shorten the image acquisition time.

In order to perform quantitative perfusion analysis, a measurement of the contrast enhancement in the LV blood pool is necessary. Furthermore, the signal intensity in the LV blood pool and myocardium is required to be linear with the concentration of contrast agent for accurate perfusion quantification. The LV blood pool signal is distorted by $T2^*$ effects at peak enhancement, which occurs due to passage of high contrast agent concentrations through the LV and this, affects the measurement of the signal. In order to address this, two different imaging strategies were introduced 1) dual-bolus (35,36) and 2) dual contrast (37). In the dual bolus sequence, a low dose injection of the contrast agent is used to measure the LV blood pool signal, followed by a second high dose contrast agent injection to measure the myocardial signal (35,36). On the other hand, the dual-contrast acquisition uses a single high dose contrast-agent injection to measure both the blood pool signal using a short saturation delay and the myocardial signal using a longer saturation delay (37). A dual-contrast acquisition simplifies the procedure (one Gd injection) and may provide more accurate results than the dual-bolus method because the blood pool and myocardial signals are acquired under identical conditions.

The signal intensities are then converted into absolute gadolinium concentration-time curves. The conversion to gadolinium concentrations can be done either using a

look-up table, which is created using phantoms containing various known concentrations of Gd or using a theory-based signal calibration approach (38). The theory-based signal calibration approach estimates T1 from a single image and uses the known relaxivity of Gd to calculate the absolute Gd concentration. It uses the relationship between the normalized signal (calculated as the signal of the T1-weighted image normalized to the signal of a proton density image) and known imaging parameters to estimate T1. The LV blood pool Gd concentration function is known as arterial input function (AIF) and the myocardial tissue Gd concentration function is known as the tissue function (TF).

MBF can be assessed semi-quantitatively or quantitatively. Semi-quantitative measures of MBF include upslope analysis where the upslope refers to the slope of the signal intensity curve in the early contrast enhancement phase. The upslope of the myocardial signal intensity curve normalized to the blood pool signal intensity curve has been used in some studies for perfusion assessment (39). Myocardial blood flow can be quantified using either a deconvolution method or a by using a compartment model approach (40). The deconvolution method is derived from the Central Volume Principle. Using this method, the tissue function can be obtained by a convolution integral between the arterial input function and an impulse response:

$C_{TF}(t) = C_{AIF}(t) \otimes h(t)$, where $C_{TF}(t)$ is the tissue function, $C_{AIF}(t)$ is the arterial input function and $h(t)$ is the tissue impulse response.

Several mathematical models have been proposed to estimate $h(t)$ such as Fermi function model (41), series of B-spline functions (42), series of exponential

functions (43) and autoregressive moving average model (44). Fermi function model is most commonly used to quantify MBF.

(b) Arterial Spin Labeling (ASL):

ASL is an alternative approach to measure perfusion non-invasively using water protons in blood as an endogenous tracer. It is based on labeling water in blood using a spatially selective inversion pulse and measuring the signal changes that occur when the inverted blood water spins flow in and out of an adjacent region. The technique is generally divided into continuous ASL and pulsed ASL. In continuous ASL, the labeling is applied over a much longer time and it establishes a steady state in the tissue of interest. On the other hand, in pulsed ASL, a bolus of arterial blood is labeled and it passes through the tissue as a transient. There are different types of pulsed ASL techniques depending on the way the labeling is applied such as EPISTAR (45), PICORE (46), FAIR (47,48) and TILT (49). ASL is more commonly used to image perfusion in the brain.

Flow-sensitive alternating inversion recovery (FAIR) ASL employs two sets of images: a control and a tagged image set. The control image is acquired using a non-selective inversion pulse where all spins in the body are inverted and the tagged image is acquired using a slice-selective inversion pulse where only the spins in the imaging slice or slightly beyond are inverted. Thus, in the control image, both the inflowing blood water protons and the water protons in the tissue in the imaging slice are inverted. Since the T1 of arterial blood is only slightly longer than the T1 of myocardial tissue, the inflow of blood water protons into the myocardial tissue does not affect the T1 of the

tissue in the control image. However, in the tagged image, the inflowing blood water protons are not inverted, while the water protons in the tissue in the imaging slice is inverted. This inflow and exchange of non-inverted blood water protons into the imaging slice causes an apparent T1 shortening effect, which can be used to quantify perfusion.

The FAIR technique has advantages as compared to the other ASL techniques. In the tagged image, arterial blood flowing from both proximal and distal sides of the imaging slice is non-inverted. Thus, the estimated perfusion using FAIR technique is sensitive to inflow of blood from all directions. This is especially useful in the heart, where there are many coronary arteries supplying blood to the myocardial tissue and the blood distribution of these arteries is complicated.

Perfusion in ASL can be quantified using the modified Bloch equation (50):

$\frac{dM(t)}{dt} = \frac{M_0 - M(t)}{T_1} + fM^A(t) - fM_v(t)$, where M(t) is the longitudinal magnetization of the tissue, M_0 is the equilibrium tissue magnetization, M^A(t) is the longitudinal magnetization of the inflowing blood, M_v(t) is the longitudinal magnetization of the outflowing blood, f is the flow and T1 is the relaxation time constant of the myocardium. Here the first term accounts for T1 relaxation, the second term accounts for inflow of blood and third term accounts for outflow. If we assume a well-mixed single compartment, then the magnetization of the outflowing venous blood can be written as:

$M_v(t) = \frac{M(t)}{\lambda}$, where λ is the blood-tissue partition coefficient and can be expressed as

$$\lambda = \frac{\text{Quantity of water per gram of tissue}}{\text{Quantity of water per milliliter of blood}}$$. For myocardial tissue, this ratio is assumed

to be 0.95. Bauer *et al.* (51) and Belle *et al.* (52) extended this to a two compartment

tissue model and derived a simple expression for perfusion for the FAIR ASL technique.

This model assumes fast exchange between the two compartments, which is

appropriate for the myocardial tissue. If $T1_{ss}$ is the T1 of myocardial tissue after slice-

selective inversion, $T1_{NS}$ is the T1 of myocardial tissue after non-selective inversion and

$T1_{blood}$ is the T1 of arterial blood, then perfusion (P) can be estimated as follows (52):

$$P = \lambda \frac{T1_{NS}}{T1_{blood}} \left(\frac{1}{T1_{SS}} - \frac{1}{T1_{NS}} \right)$$, where λ is the blood-tissue partition coefficient for water.

A mathematical model for ASL can also be derived using tracer kinetic

methodology, where water is the endogenous tracer. Using this methodology, Buxton *et*

al. (53) derived a general kinetic model for ASL where the difference in longitudinal

magnetization between the control and tagged image (ΔM) can be expressed as a

convolution integral between an arterial input function, c(t) and a residue function, r(t):

$$\Delta M = 2\alpha M_b^0 \int_0^t c(\tau) r(t - \tau) d\tau$$, where α is the inversion efficiency and M_b^0 is the

equilibrium blood magnetization. In the original formulation, Buxton *et al.* assumed the

AIF to be plug flow. Thereafter, other studies have derived modified mathematical

models using more realistic assumptions for the shape of AIF (54).

ASL has the advantage of not requiring exogenous contrast agents. Hence, it

can be used repeatedly and it can also be used in patients who have compromised

renal function since gadolinium based contrast agents are contraindicated in these patients. However, a major disadvantage of ASL is its inherent low sensitivity to blood flow. In humans, MBF is about 0.5 - 4 ml/g/min and at typical magnetic strengths of 1.5 - 3T, this corresponds to ASL signal of 1% to 8%. However, ASL is widely used to quantify MBF in rodents since MBF in rodents ranges between 5 – 12 ml/g/min.

1.5. Mouse models

1.5.1. Mouse models in cardiovascular research

Mouse models are one of the most commonly used animal models in cardiovascular research. There are several reasons for this, some of them being: low cost, high reproduction rate, short gestation period, low breeding and housing cost, ease and success of genetic manipulation and ease of maintenance and handling. Furthermore, the mouse genome has been recently sequenced and this has made genetic manipulation of mice easier and increased the availability of transgenic and gene-knockout mouse models. Research using transgenic and knockout mice has provided tremendous insights into the genetic, molecular, and cellular mechanisms underlying every major cardiovascular disease, and has contributed extensively to the development of new clinical medical therapies (55-58).

Reduced MPR is a marker of IHD and has been shown to be prognostic of adverse cardiovascular outcomes. Impaired MPR has been detected in patients even in the absence of obstructive CAD. However, the mechanisms that cause reduction in MPR in the absence of obstructive CAD are not entirely clear. Thus, there is a need for

experimental studies investigating molecular mechanisms that underlie abnormal coronary vascular function in the absence of obstructive CAD. Currently, there is no mouse model of abnormal coronary vascular function in the absence of obstructive CAD. A mouse model that recapitulates coronary vascular dysfunction documented by impaired MPR in the absence of obstructive CAD will enable the investigation of mechanisms that underlie abnormal coronary vascular function and promise to be useful in the assessment of therapies for IHD.

1.5.2. Mouse models in obesity

Several mouse models have been used to investigate and understand mechanisms underlying obesity related cardiac dysfunction. The mouse models can be divided into two types: 1) transgenic or knockout mouse models, where specific genes are manipulated or genetic mutations are induced in order to cause obesity and 2) diet induced obesity mouse models, where wild type mice are fed diets rich in fat. Recent studies have provided a comprehensive review of the commonly used mouse models to study obesity related cardiac dysfunction (18,59).

Some of the common knockout mouse models that have been previously used to study obesity include ob/ob mice (deficient in leptin gene), adiponectin gene knockout mice, neuronal insulin receptor knockout mice, β3 adrenergic receptor knockout mice and serotonin 5-HT-2c receptor knockout mice (18,59). A prior study used ob/ob mice to show that deficiency of leptin gene results in cardiomyocyte contractile dysfunction (60). Some of the common transgenic mouse models used in obesity research include db/db mice (mutation in leptin gene), UCP-DTA mice (which result in brown adipose tissue

ablation) and transgenic mice overexpressing glucose transporter subtype 4 (GLUT4) (18,59). A previous study published in Nature used UCP-DTA mice to genetically ablate brown adipose tissue and showed that this resulted in obesity in the mice and that these mice eventually developed hyperphagia (61). This study provided evidence to the critical role played by brown adipose tissue in maintaining energy balance. Several non-obese transgenic mouse models have also been used to probe important pathways that are implicated in cardiac dysfunction due to obesity. For example, cardiac lipotoxicity is believed to be one of the mechanisms responsible for causing cardiac dysfunction in obesity related cardiomyopathy. A prior study used transgenic mice with cardiomyocyte overexpression of peroxisome proliferator-activated receptor (PPAR)-α and showed that the mice developed diabetes induced cardiac hypertrophy and they further fed some of the mice with diet rich in long chain fatty acid and showed that cardiac lipotoxicity is partly mediated by long-chain fatty acids (62).

Along with genetic and environmental factors, consumption of high amounts of dietary fat has also been associated with development of obesity and type 2 diabetes in humans (63-66). Hence, mouse models with diet-induced obesity have been used to explore the effects of different types of high-fat diets on obesity and its comorbidities such as hypertension, type 2 diabetes, hypercholesterolemia, hyperlipidemia and atherosclerosis (59,67). A variety of rodent diets with varying nutrient compositions exist. The amount of fat in a high-fat diet usually ranges from 30-78%. Diets with varying amounts of carbohydrate, protein, fatty acids and diets rich in both sugar and fat content are also available. The diet composition plays a major role in the induction of obesity. A

recent article provides a comprehensive review of the various types of animal diets available and their macronutrient compositions and their ability to induce obesity (68).

Prior studies investigating cardiac dysfunction due to obesity in animal models have been either *in vivo* or *in vitro* using isolated cardiomyocytes or in isolated perfused hearts (18). The *in vivo* studies have primarily used echocardiography to study cardiac function in murine models. Very few studies have used cardiac MRI to explore these mouse models and there has been no prior published work looking at *in vivo* quantitative myocardial perfusion in these mouse models.

1.6.   Cardiac Magnetic Resonance (CMR) in Mice

Cardiac magnetic resonance imaging has become a standard modality for non-invasive imaging of the human heart and is considered the gold standard for quantification of myocardial mass, volumes and function (33). CMR of the mouse heart has also been extensively used for various applications and has proved to be a great tool in cardiovascular research in mice. A comprehensive review of the various emerging CMR techniques in mice can be found in a recent review article by Vandsburger *et al.* (69). Briefly, CMR has been used by prior studies to assess *in vivo* LV structure (70), contractile function (71,72), the presence and extent of myocardial infarction (MI) (73,74), myocardial viability, fibrosis in the heart (75), edema after MI (76) and myocardial perfusion (77). CMR in mice has also been used to track labeled cells in heart (78), to assess cardiac regeneration (79) and calcium function in the heart (80).

Thus, CMR in mice has proved to be a powerful research tool in cardiovascular research and the knowledge gained from the preclinical experiments can be a great aid in furthering our understanding of the heart and various disease processes.

1.6.1. CMR of LV mass and volumes in mice

CMR has been used in several prior studies to measure LV volumes, ejection fraction, LV mass and LV wall thickness in mice (73). Because of its excellent image quality and high spatial resolution, CMR has also been used in post-MI mice to serially assess LV remodeling (73). The following Figure 1.4 demonstrates the typical image quality obtained using cine imaging in mice.
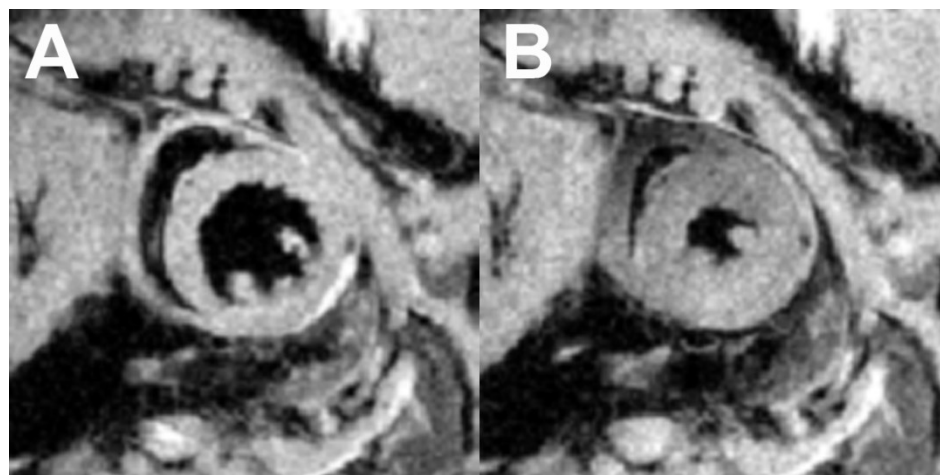
Figure 1.4: Cine MRI in mice. This figure shows example black-blood cine images obtained from a mouse heart at end-diastole (A) and at end-systole (B).

Cine MRI is often performed using bright blood multi phasic spoiled gradient echo techniques (81). However in our study, multi-slice cine MRI in mice has been performed using a previously developed black-blood gradient echo sequence which

uses a double inversion recovery strategy to nullify the signal in the blood pool (70). This provides better delineation of the endocardium over the entire cardiac cycle and thereby improves the accuracy of the LV volume and LV mass measurements. Using image analysis software such as Segment, the end-diastolic and end-systolic frames for all the slices can be identified and the endocardium and epicardium can be easily contoured. Thereafter using the Segment software, LV end-diastolic volume, end-systolic volume, ejection fraction, LV mass and LV wall thickness can be easily quantified.

1.6.2. CMR of contractile function in the mouse heart

Quantitative wall motion imaging has been performed previously in mice using various techniques such as myocardial tagging, velocity-encoded phase-contrast imaging, harmonic phase (HARP) analysis and displacement-encoded imaging with stimulated echo's (DENSE) (55). Using these techniques, circumferential strain (E_{cc}) and the rate of circumferential strain (dE_{cc}/dt) can be quantified *in* vivo and these correspond to the shortening and shortening velocity of the cardiomyocyte respectively. Myocardial tagging is well-established technique and has been previously used both in humans and in mouse models. Prior studies have used myocardial tagging in mice to quantify regional contractile function after MI (73,82) and to demonstrate the roles of individual genes in contractile function in transgenic and knockout mouse models (73,83).

Cine DENSE MRI is a more recent technique that was built on the concepts of myocardial tagging and provides higher spatial resolution. It has been used previously

to quantify circumferential displacement and strain in mice (72,78) and humans (84-86).

Using a spiral cine DENSE sequence (85,86), regional myocardial displacement and

strain for the entire cardiac cycle can be quantified in 2D and 3D in mice at 7T with high

spatial resolution (87). Using a semi-automatic (88) or automatic DENSE analysis tool

(89), the DENSE images can be easily analyzed to quantify displacement and strain for

all phases of the cardiac cycle. Figure 1.5 shows example images obtained using a cine

DENSE sequence in a mouse heart. Using strain-time curves, peak circumferential

strain and strain rate (dE_{cc}/dt) can be quantified.
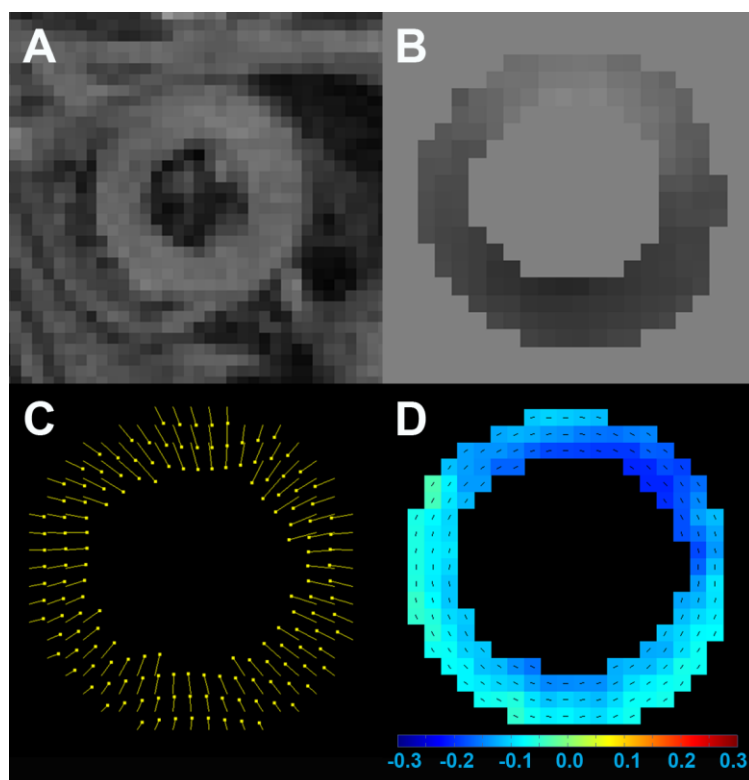
Figure 1.5: Cine Dense MRI in mice. This figure shows an example short-axis cine

DENSE magnitude image (A) and phase image (B) obtained from a mouse heart. (C):

An example short-axis displacement map obtained from a wild type mouse heart. (D):

An example short-axis circumferential strain map obtained from a wild type mouse heart.

1.6.3. Assessment of myocardial perfusion in the mouse heart

PET and MRI are the only two quantitative perfusion imaging modalities and MRI has significant advantages for assessment of myocardial perfusion in the mouse heart, most notably the high spatial resolution. The following Figure 1.6 shows the image quality obtained by myocardial perfusion imaging in the mouse heart using PET and two different imaging techniques in MRI: ASL and First-pass contrast-enhanced MRI.
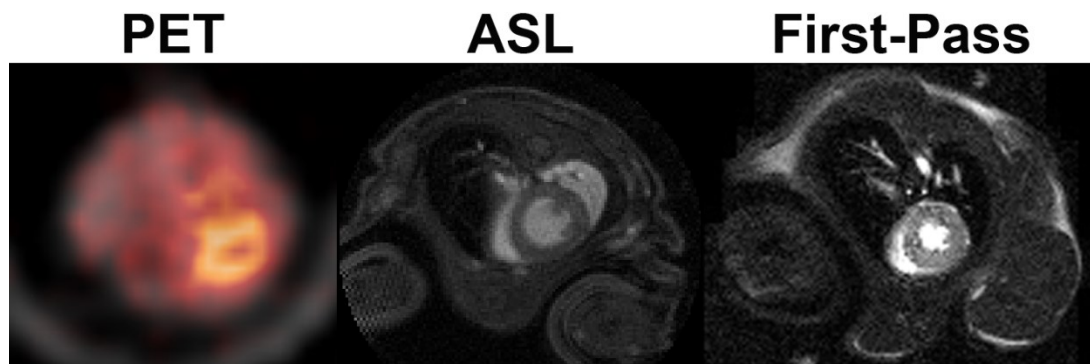
Figure 1.6: Myocardial perfusion imaging in the mouse heart using PET and MRI. This figure demonstrates the image quality and spatial resolution obtained with myocardial perfusion imaging in mice using PET and two MRI techniques: ASL and First-pass.

1.6.3.1.   First-pass contrast-enhanced MRI in Mice

First-pass Gd-enhanced MRI is a well-established non-invasive technique to measure perfusion in humans, however the method is less mature in mice and has only been recently investigated in these animals (38-41). This is because the rapid heart

rate, small heart size and free breathing in mice make quantitative first-pass imaging in mice challenging. The heart rate in mice is 400-600 bpm (R-R interval is ~120 ms at rest and ~100 ms with vasodilation), which implies that there is about 80-90 ms to acquire both the AIF and TF. Thus, a fast imaging protocol is essential. The left ventricle in mice is about 5-6 mm in diameter. This implies that high spatial resolution is necessary to obtain images that capture the transit of contrast agent through the heart. The systemic circulation time in mice is extremely rapid (4-5 sec), which implies that high temporal sampling is necessary. Thus, respiratory gating is not possible due to which there are artifacts in images.

Due to technical limitations for temporal and spatial resolutions, it was not possible to perform first-pass MRI until recently. With recent advances in compressed sensing (CS) (90) and parallel imaging (91), it has been possible to accelerate the imaging times in mice. Recently, a few groups have performed first-pass MRI in the mouse heart using segmented acquisitions with parallel imaging (92,93) and k-t undersampling techniques with k-t principle component analysis reconstruction (94,95).

1.6.3.2.   ASL in Mice

ASL is another perfusion MRI technique that allows quantitation of MBF. The use of this method in the heart is however limited in humans because of the relatively modest changes in signal due to spin labeling and cardiac motion artifacts. However, in mice, where MBF is higher than in humans, ASL has been used to measure myocardial perfusion at rest (77,96-102), after vasodilation (77,98,102) and after MI (77,99,100). ASL has also been used previously to investigate myocardial perfusion in knockout

mouse models (99,102). Our group has previously implemented ASL using the FAIR preparation scheme combined with a cardio-respiratory Look-Locker spiral gradient echo (77). Shown below are example images obtained using this technique. These images were acquired using a low flip angle of 3^0, which minimizes perturbation of the longitudinal magnetization and allows for accurate quantifications of T1.
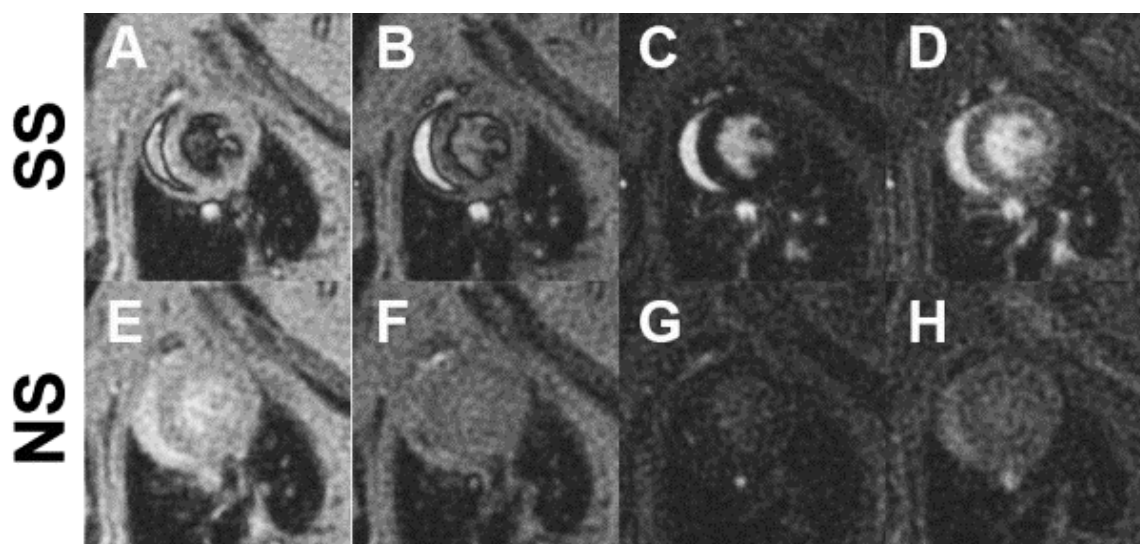
Figure 1.7: ASL in mice. (A-D): Images obtained after a slice-selective inversion from a mouse heart. (E-H): Images obtained after a non-selective inversion from a mouse heart.

1.7. Specific Aims

For this dissertation, <u>Specific Aim 1 is (a) to develop improved quantitative first-pass perfusion MRI for mice and to evaluate this method at rest and with vasodilation and (b) to use these methods to test the hypothesis that C57Bl/6 mice fed a high-fat diet</u>

have impaired myocardial perfusion reserve. First-pass Gd-enhanced MRI is a well-established non-invasive technique to measure perfusion in humans, however the method has only been recently investigated in these animals (92-95) due to technical challenges. A fast imaging protocol is essential and we achieved this by undersampling the images. In order to overcome motion artifacts due to free-breathing in mice, we used a motion-compensated CS algorithm to reconstruct the undersampled images, a dual-contrast acquisition simplifies the procedure (one Gd injection) and may provide more accurate results than previous methods because the AIF and TF are acquired under identical conditions. Thus, an accelerated dual-contrast sequence was developed for first-pass perfusion imaging in mice and the sequence was evaluated in wild type mice at rest and after vasodilation. Furthermore, we also used this sequence to investigate whether mice fed a high-fat diet have impaired MPR after 24 weeks of diet. The material for this aim is covered in Chapter 2 and this has been previously published in Naresh *et al.* (103).

Specific Aim 2 is to compare the reproducibility and intra and inter-user variability of the two perfusion imaging methods, arterial spin labeling (ASL) and first-pass MRI, in mice under the conditions of rest, stress and infarct. Perfusion in MRI can be quantified using two techniques: first-pass contrast enhanced MRI and ASL. In humans, first-pass contrast enhanced MRI is routinely used for perfusion studies because it is quick and reproducible. However, it has only been recently investigated in mice (92-95) because of technical challenges as mentioned earlier. ASL is not clinically used in humans for myocardial perfusion imaging because of its lengthy imaging times and low sensitivity. However, it has been previously used to study myocardial perfusion in mice at rest, after

vasodilation and after MI (77,96,98-102,104,105). There is no published work comparing the two imaging techniques for myocardial perfusion imaging in mice. For this aim, wild type mice were studied at rest, stress and on day 1 post-MI using both first-pass and ASL. To assess reproducibility, perfusion imaging using both the techniques was repeated on a different session. The two techniques were also compared for image quality, intra-user and inter-user variability. The material for this specific aim is covered in Chapter 3, and it is not yet published.

Specific Aim 3 is to establish the time course of impaired myocardial perfusion reserve and LV hypertrophy in C57Bl/6 mice fed a high-fat diet. Obesity has become increasing prevalent in western society and is independently associated with impaired myocardial perfusion reserve. In this aim, we used methods developed in Specific Aim 1 in a mouse model of diet-induced obesity to establish the time course of MPR and we further used *ex vivo* histological and vascular reactivity studies to elucidate factors underlying the MRI results. Wild type mice were fed a high-fat diet or a low-fat diet and imaged at 6, 12, 18 and 24 weeks post-diet. The MRI protocol included multi-slice cine imaging to assess ejection fraction, LV mass, LV wall thickness, and LV volumes, cine-DENSE to assess peak circumferential strain and first-pass imaging to quantify MPR. Vascular reactivity of isolated coronary arterioles was assessed in a sub-group of the mice. Histology of the aorta detected the presence or absence of systemic atherosclerosis, and myocardial capillary density and interstitial and perivascular fibrosis were quantified. The material of this specific aim is covered in Chapter 4, and it is not yet published

Chapter 2: Accelerated Dual-contrast First-pass Perfusion MRI of the Mouse Heart: Development and Application to Diet-induced Obese Mice

2.1. Introduction

Assessing myocardial perfusion or perfusion reserve (MPR) is of value in the diagnosis of ischemic heart disease, and impaired MPR has been shown to be prognostic of adverse cardiovascular outcomes (24). Furthermore, myocardial perfusion or perfusion reserve may be reduced due to obstructive epicardial atherosclerosis or due to microvascular disease. MPR is defined as the ratio of myocardial blood flow at maximal hyperemia to myocardial blood flow at rest. In patient populations of diabetics, women, and individuals with the metabolic syndrome, the mechanisms underlying reduced perfusion or MPR are not completely understood (6,7,32). Research using transgenic and knockout mice has provided tremendous insights into the genetic, molecular, and cellular mechanisms underlying every major cardiovascular disease, and has contributed extensively to the development of new medical therapies (55-58). Quantitative myocardial perfusion imaging in gene-modified mice may be used to elucidate molecular mechanisms underlying insufficient perfusion and to assess the efficacy of experimental therapies. Currently, quantitative myocardial perfusion imaging in mice can be performed using arterial spin labeling (ASL) MRI (77,97,98,100,101), however, ASL requires long acquisition times.

First-pass gadolinium (Gd)-enhanced MRI is a well-established technique to quantify MBF and MPR in humans and it has only been recently investigated in mice (92-95,106). First-pass MRI in mice is challenging due to the rapid heart rate and small size of the mouse heart, and because image acquisition occurs during free breathing, which can lead to image artifacts. Recent MRI acceleration techniques have made first-pass imaging in mice possible. Quantitative first-pass MRI relies on the accurate

measurement of both the myocardial tissue function (TF) and the arterial input function (AIF), which is usually measured in the LV blood pool. Quantitative first-pass MRI in humans is often performed using either a dual-bolus technique or a dual-contrast technique. A dual-bolus technique uses a low dose injection of the contrast agent to measure the AIF followed by a high dose contrast-agent injection to measure the myocardial tissue function (TF) (35,36). On the other hand, a dual-contrast acquisition uses a single high dose contrast-agent injection to measure both the AIF using a short saturation delay and the TF using a longer saturation delay (37). A dual-contrast acquisition simplifies the procedure (one Gd injection) and may provide more accurate results than the dual-bolus method because the AIF and TF are acquired under identical conditions.

Our goals for this study were to develop a dual-contrast first-pass sequence for mice and to use these methods to test the hypothesis that C57Bl/6 mice fed a high-fat diet (HFD) for 24 weeks have reduced MPR. This diet-induced obesity (DIO) model was recently shown to recapitulate many hallmarks of human diabetic cardiomyopathy after 8 months on diet, including obesity, hyperglycemia, insulin resistance, and hyperinsulinemia, all in the absence of epicardial coronary artery disease (107). For the first time, we sought to establish another hallmark of human diabetic cardiomyopathy, namely reduced MPR, in these mice.

2.2. Methods

2.2.1. MRI Hardware and First-pass Pulse Sequence

MRI was performed on a 7T Clinscan system (Bruker, Ettlingen, Germany) equipped with actively shielded gradients with a full strength of 650 mT/m and a slew rate of 6666 mT/m/ms. Additional equipment included a 30 mm diameter birdcage RF coil and an MR-compatible physiological monitoring and gating system for mice (SA Instruments, Inc., Stony Brook, NY).

A dual-contrast saturation-recovery Cartesian sequence with a gradient-echo readout and k_y- and time domain (k_y-t) undersampling was implemented. The acquisition scheme is illustrated in Figure 2.1. The saturation pulse was chosen to be an adiabatic BIR4 pulse with a duration of 9 ms, in order to achieve uniform saturation (108). Two short-axis slices (slice gap = 0.2 mm) were acquired within each cardiac cycle, one to obtain the AIF and the other to obtain the TF. Respiratory gating was not applied. For both slices, the center of k-space was acquired at the Nyquist sampling rate while the higher spatial frequencies were randomly undersampled in the k_y-t domain. This undersampling scheme was employed in order to facilitate image reconstruction using compressed sensing (90). The AIF slice was undersampled at rate six while the TF slice was undersampled at rate four. These acceleration rates of 6 and 4, respectively, have previously been shown to provide good image quality for human first-pass images reconstructed using a motion-compensated compressed sensing algorithm, even when respiratory motion occurs (109). Undersampled proton density images were acquired toward the end of the acquisition in order to normalize signal

intensities for perfusion analysis. Other relevant imaging parameters were: TE/TR = 1.2/2.1 ms, FOV = 25.6 x 18-20 mm^2, phase FOV = 72%, percent sampling = 80%, image resolution = 200 μm^2, matrix = 128 x 74-104, excitation flip angle = 15^0, slice thickness = 1 mm, AIF saturation delay = 15 ms, TF saturation delay = 57-74 ms, AIF image acquisition time = 25-34 ms/image and TF image acquisition time = 36-53 ms/image. 12-16 phase-encode lines were acquired for each AIF image and 17-25 lines were acquired for each TF image. For the AIF images centric k-space filling was used to enable a short saturation delay, while for the TF images linear k-space filling was used.
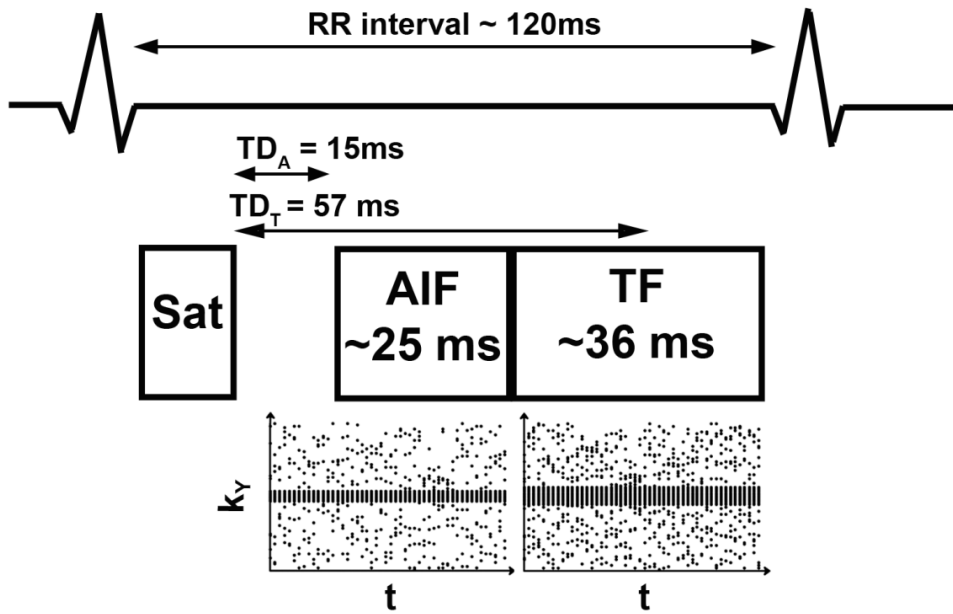
Figure 2.1: Diagram for the CS-accelerated dual-contrast first-pass MRI pulse sequence. A saturation pulse is applied after detection of the R wave and thereafter two slices are acquired in each cardiac cycle: 1) the AIF slice at acceleration rate 6 and at a saturation delay of 15 ms, with centric k-space ordering; 2) the TF slice at acceleration rate 4 and at a saturation delay of about 57 ms, with linear k-space ordering. The k_y-t sampling patterns for the two slices are also shown.

2.2.2. Compressed Sensing Reconstruction

A motion-compensated compressed-sensing technique called Block LOw-rank Sparsity with Motion-guidance (BLOSM) was recently developed to reconstruct undersampled dynamic images, including images acquired during breathing (109). This method utilizes the concept of spatiotemporal low rank sparsity, as used in the k-t Sparsity and Low-Rank (k-t SLR) technique (110). In BLOSM, the image is divided into regions (or blocks), motion tracking of the blocks is embedded within the iterative algorithm, and regional low-rank sparsity is applied to the motion-tracked blocks. BLOSM achieved very good results in human first-pass images, including those with respiratory motion (109). Because first-pass MRI in mice occurs during breathing, BLOSM was chosen to reconstruct undersampled first-pass data in this context.

2.2.3. Experimental Design

The experimental design was divided into two parts: 1) evaluation of the sequence over a range of vasodilator doses and using two different vasodilator agents using wild-type C57Bl/6 mice fed a standard chow diet, and 2) use of the sequence to test the hypothesis that MPR is reduced in DIO mice. For the first part, 20 – 24 week old wild type C57Bl/6 mice were imaged using the dual-contrast first-pass sequence at rest (n = 6) and with the vasodilators Regadenoson (n = 6) (Lexiscan, Astellas Pharmis, 0.1 µg/g body weight) and ATL313 (separate group, n = 6) (Adenosine Therapeutics, 0.025 µg/g body weight). In addition to these doses, 12 week old wild type mice (n = 5) were imaged with different doses of Regadenoson (0.01, 0.02 and 0.05 µg/g body weight) in order to test whether first-pass MRI could detect incremental increases in MBF. The

different doses of Regadenoson were administered in different imaging sessions that were performed on separate days. The reason for this is that the terminal half-life of Regadenoson is very long (33-108 minutes) (111). Thus the wait time for the effect of Regadenoson to wear off would be long, thereby making the imaging session too long. Finally, C57Bl/6 mice fed a HFD (Diet # D12492, Research Diets, Inc., New Brunswick, NJ) were studied. Specifically, DIO mice fed a HFD for 24 weeks (n = 6) and age-matched wild type C57Bl/6 mice (n = 5) fed standard chow diet were imaged at rest and with Regadenoson (0.1 µg/g body weight) using the dual-contrast sequence. DIO mice were started on the diet at 6 weeks of age and the imaging was performed after continuing the diet for 24 weeks. Only DIO mice that were glucose intolerant were selected for imaging. For the glucose-tolerance test (GTT) (112), mice were injected intraperitoneously with 1 g/kg glucose in milli-Q water after overnight fasting. A tail vein blood sample was taken before and at 10, 30, 60, 90 and 120 minutes post-injection of the glucose solution for determination of blood glucose. The blood glucose values were then plotted versus time and the area under the curve was calculated to evaluate glucose tolerance.

2.2.4. Animal Handling

All animal studies were performed under protocols that comply with the *Guide for the Care and Use of Laboratory Animals* (NIH publication no. 85-23, Revised 1996) and were approved by the Animal Care and Use Committee at our institution. An indwelling tail vein catheter was established to deliver Gd-DTPA (Magnevist, 0.1 mM/kg body weight) and Regadenoson, while ATL313 was delivered by an intraperitoneal (IP) bolus

injection. Mice were positioned supine in the magnet and body temperature was maintained at 36 ± 0.5 ^{0}C using thermostated water. Anesthesia was maintained using 1.25% isoflurane in O_2 inhaled through a nose cone during imaging. The ECG, body temperature and respiration were monitored during imaging using an MR-compatible system (SA Instruments, Stony Brook, New York).

2.2.5. MRI Protocol

In all mice, localizer cine imaging was performed to select a mid-ventricular short axis slice. For first-pass imaging, the CS-accelerated dual-contrast first-pass sequence was used as described above. A series of 250 first pass images were acquired using the dual-contrast sequence. Ten seconds after the acquisition started, the contrast agent was injected i.v. while imaging continued in order to capture first-pass kinetics. For the stress-perfusion acquisition, Regadenoson was injected through a tail vein catheter and 10 minutes later first-pass imaging was performed while injecting Magnevist through the same tail vein catheter. We waited for 10 minutes after the injection of the stress agent for the heart rate to stabilize before injecting Magnevist and performing the first-pass acquisition.

2.2.6. Perfusion analysis

All data analysis was based on Fermi function deconvolution, implemented in MATLAB (Mathworks, Inc). To generate signal intensity vs. time curves, one region of interest (ROI) was placed in the LV blood pool in the images with the short saturation delay to obtain the AIF, while the TF was generated using a ROI covering the entire

myocardial tissue in the images acquired using the longer saturation delay. These signal intensities were normalized by the signal intensities of the proton density images and thereafter were converted to T1 values using the methods described by Axel *et al* (38). Since the accuracy of this method is poor at long T1 values (38), prior ASL measurements were used to fix pre-contrast T1 values for the blood (1.55 s) and for the myocardium (1.45 s). Precontrast T1 was measured in 6 wild type mice (separate group) using a Look-Locker sequence with a 3° excitation flip angle (77,78). The T1-relaxation measurements were fit to this equation: $M_z = M_0 exp(-t/T_1)$. Precontrast blood T1 was found to be 1.55 ± 0.04 s which is in agreement with prior studies (77,100) while the precontrast myocardial T1 was found to be 1.45 ± 0.02 s, which is also in agreement with prior studies (77,78). Relaxivity was assumed to be 3.8L/mmol.s (113) which was used to convert T1 values to gadolinium concentrations. Absolute MBF was calculated from the LV blood pool and myocardial tissue gadolinium concentration-time curves (AIF and TF) using Fermi constrained deconvolution (41). To demonstrate the ability of the CS-accelerated dual-contrast sequence to quantify regional perfusions, the myocardium was divided into 6 sectors which were identified clockwise starting from the RV insertion point as: anterior, anterolateral, inferolateral, inferior, inferoseptal, and anteroseptal. Regional tissue functions were obtained by placing ROIs in these sectors and regional perfusions were quantified using Fermi function deconvolution.

2.2.7. Statistical analysis

All MBF values are expressed as mean ± standard error. For comparing rest and stress perfusion in wild type and DIO mice the student t-test was used. One-way

analysis of variance was used to compare perfusions with different stress doses for the dose-response. Two-way analysis of variance was used to compare rest and stress perfusions within the same sector and between the different sectors. P< 0.05 was considered to be statistically significant.

2.3. Results

2.3.1. Evaluation of the sequence

Example AIF images obtained from a free-breathing mouse at rest using a short saturation delay are shown in Figure 2.2 (A-F), and representative TF images from the same mouse obtained using a longer saturation delay are shown in Figure 2.2 (G-L). Figure 2.2 (A-C) shows example AIF images undersampled at rate 6 and reconstructed using 2D Fast Fourier Transform (FFT), while Figure 2.2 (D-F) shows these AIF images reconstructed using the BLOSM technique. Figure 2.2 (G-I) shows example TF images undersampled at rate 4 and reconstructed using 2D FFT, and Figure 2.2 (J-L) shows these images reconstructed using the BLOSM technique (109). Since the AIF uses a short saturation delay, the images are acquired during systole, when the LV blood pool is only a few pixels wide (especially after vasodilation). Accordingly, a high-resolution AIF acquisition is necessary in order to resolve the LV blood pool. Figure 2.3A shows representative AIF and TF data and fits from Fermi function deconvolution obtained from a mouse at rest while Figure 2.3B shows TF data and fits obtained from mice at rest and after vasodilation. Average peak gadolinium concentration in the LV blood pool

was found to be 2.3 ± 0.2 mM at rest and 2.9 ± 0.3 mM after vasodilation for the 6 mice that were studied. Average peak gadolinium concentration in the myocardial tissue was found to be 0.4 ± 0.03 mM at rest and 0.6 ± 0.09 mM after vasodilation. The first-pass kinetics in mice occurred rapidly, over approximately 2-3 s. The average mouse heart rate in our study was 455 ± 15 bpm at rest and 563 ± 3 bpm with vasodilation (R-R interval ~ 120 ms at rest and 100 ms with vasodilation). The average breathing rate in the mice was 188 ± 19 breaths/min.
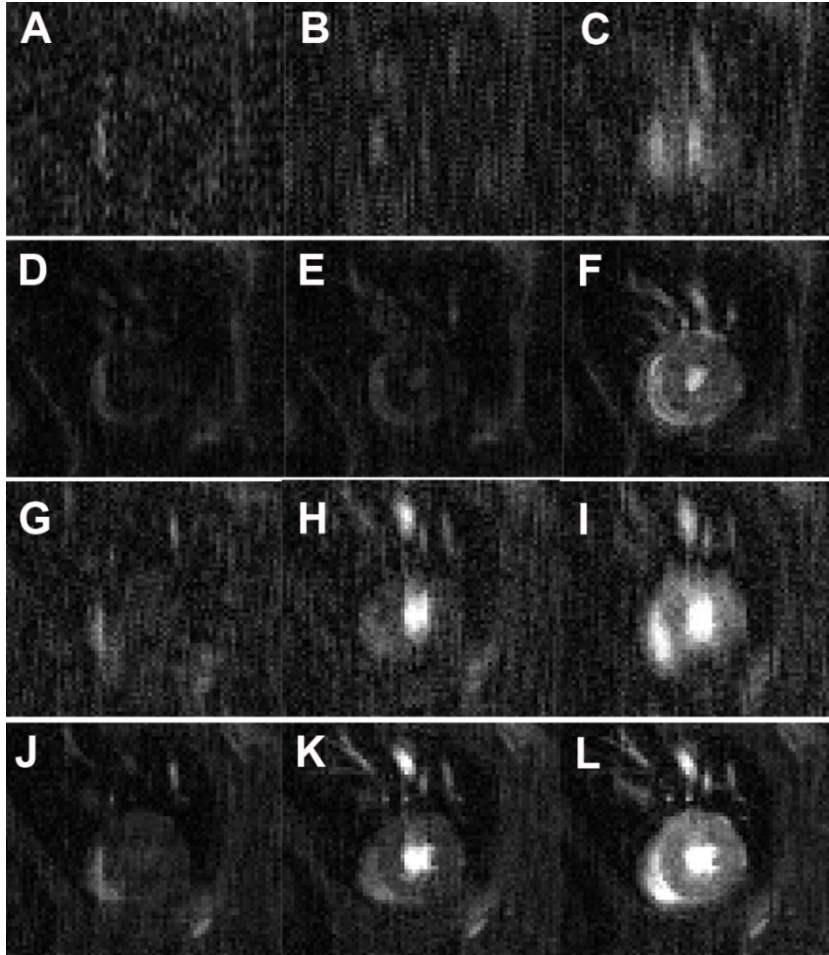
Figure 2.2: First-pass MR images from a mouse heart. This figure shows example images obtained from a mouse at rest. AIF images obtained using a short saturation delay (A-F) and TF images obtained using a longer saturation delay (G-L) show the arrival of contrast agent in the right ventricle (A, D, G, J), left-ventricular blood pool (B, E, H, K) and the myocardium (C, F, I, L). (A-C): Rate 6 undersampled AIF images reconstructed using a 2D- Fast Fourier Transform (FFT). (D-F): BLOSM-reconstructed AIF images. (G-I): Rate 4 undersampled TF images reconstructed using a 2D-FFT. (J-L): BLOSM-reconstructed TF images.
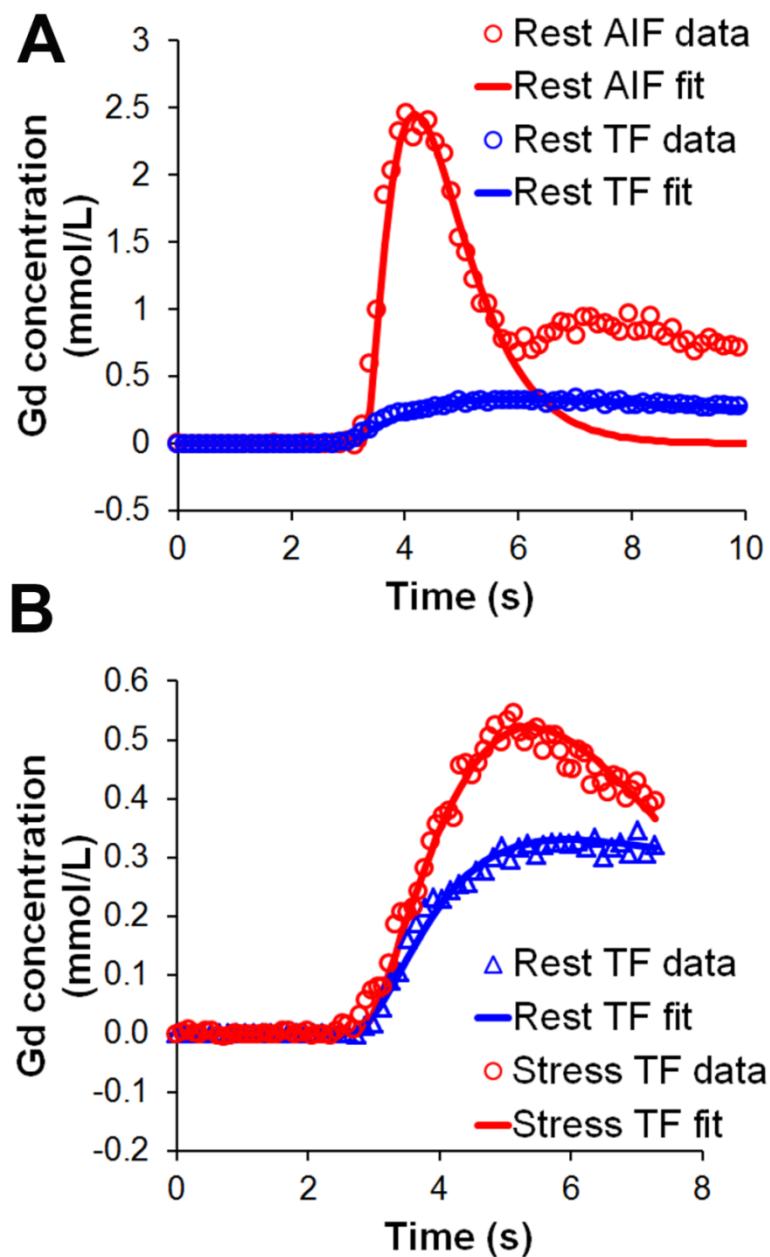
Figure 2.3: Arterial input function and tissue function data in mice. (A): Example AIF and TF data and fits obtained from a mouse at rest. (B): Example TF data and fits obtained from mice at rest (blue) and after vasodilation (red).

Perfusion was measured in wild-type mice at rest and with the vasodilators ATL313 (0.025 µg/g body weight) and Regadenoson (0.1 µg/g body weight), and these

results are summarized in Figure 2.4. Mean baseline perfusion was found to be 5.7 ± 0.8 ml/g/min and it increased to 11.8 ± 0.6 ml/g/min with ATL313 (p<0.05 vs. rest) and to 10.4 ± 0.3 ml/g/min with Regadenoson (p<0.05 vs. rest). Perfusion reserve was found to be 2.2 with ATL313 and 2.0 ± 0.3 with Regadenoson. Since separate groups of mice were used for rest and ATL313 studies, there is no standard error value reported for perfusion reserve with ATL313. We were also able to detect incremental changes in perfusion using incremental doses of Regadenoson, as shown in Figure 2.5. In this group of wild type C57Bl/6 mice, baseline perfusion was 6.1 ± 0.5 ml/g/min. Perfusion increased to 7.8 ± 0.4 ml/g/min with 0.01 µg/g body weight dose of Regadenoson, which then increased to 9.8 ± 0.7 ml/g/min with 0.02 µg/g body weight dose of Regadenoson (p < 0.05 vs. rest) and thereafter to 11.7 ± 0.3 ml/g/min with 0.05 µg/g body weight dose of Regadenoson (p < 0.05 vs. rest, p < 0.05 vs. 0.01 µg/g). With 0.1 µg/g body weight dose of Regadenoson, MBF did not increase further, and was measured as 10.8 ± 0.9 ml/g/min (p < 0.05 vs. rest, p < 0.05 vs. 0.01 µg/g).
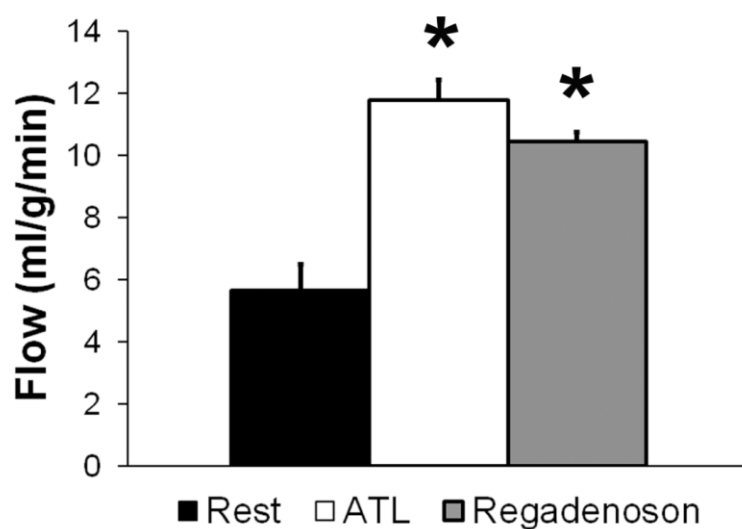
Figure 2.4: Perfusion values obtained using first-pass MRI in mice. This figure shows perfusion results obtained in wild type mice at rest and after vasodilation with ATL313 and Regadenoson. Perfusion was significantly increased with ATL313 and Regadenoson (*$p<0.05$ vs. Rest).
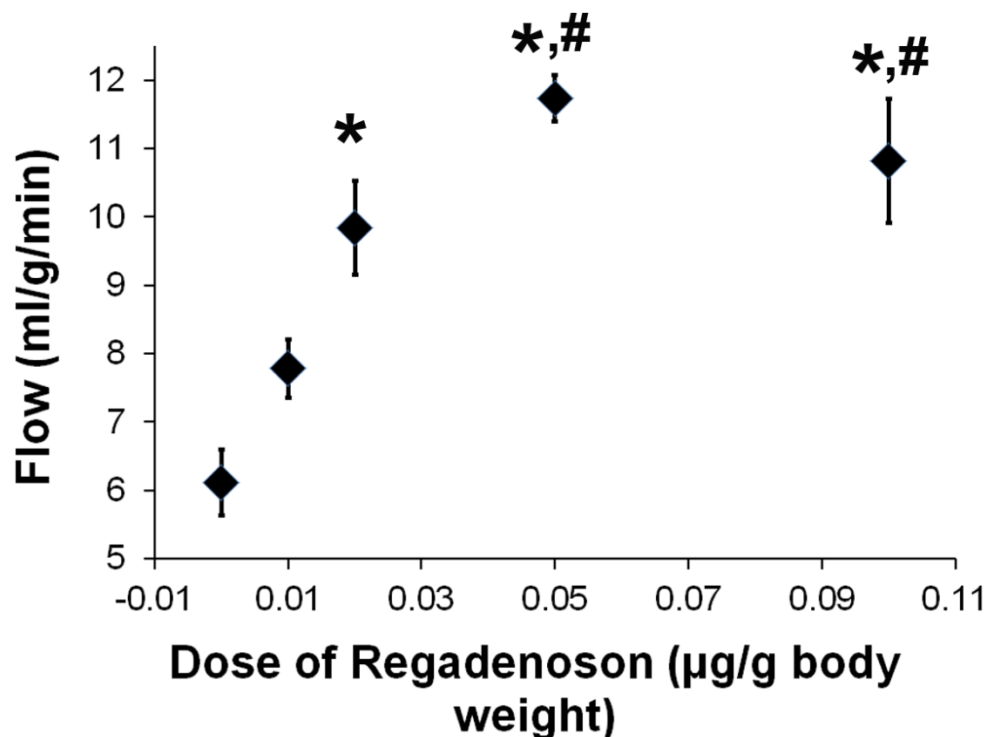
Figure 2.5: Dose-response curve with Regadenoson. This figure shows dose-response curve obtained from wild-type mice at different doses of Regadenoson. MBF increased with increasing doses of Regadenoson, until a plateau was reached above 0.05 µg/g (*$p < 0.05$ vs. rest, #$p < 0.05$ vs. 0.01 µg/g).

To demonstrate the advantage of acquiring a separate AIF acquisition with a short saturation delay when using a standard dose of gadolinium (as used in this study), Figure 2.6 compares LV blood pool gadolinium concentration estimates obtained using images acquired with a short (10 ms) and a long saturation delay (57 ms). These data show that with a Gd-DTPA dose of 0.1 mmol/kg body weight, the AIF obtained with a long saturation delay of 57 ms markedly underestimates the peak concentration. Table 2.1 compares calculated perfusion values at rest and with Regadenoson (0.1 µg/g body weight) estimated using AIFs measured from images with a short and a long saturation

delay. These results demonstrate that perfusion is overestimated when the AIF is obtained using images acquired with a long saturation delay. The error in the estimate of the AIF calculated using the images acquired with a long saturation delay may be due to signal errors arising from high blood velocities that occur in certain diastolic phases (114). This blood motion can cause dephasing during the echo time (115), leading to signal loss and lower AIF estimates. Placing the AIF acquisition near end systole provides less sensitivity to signal dephasing.
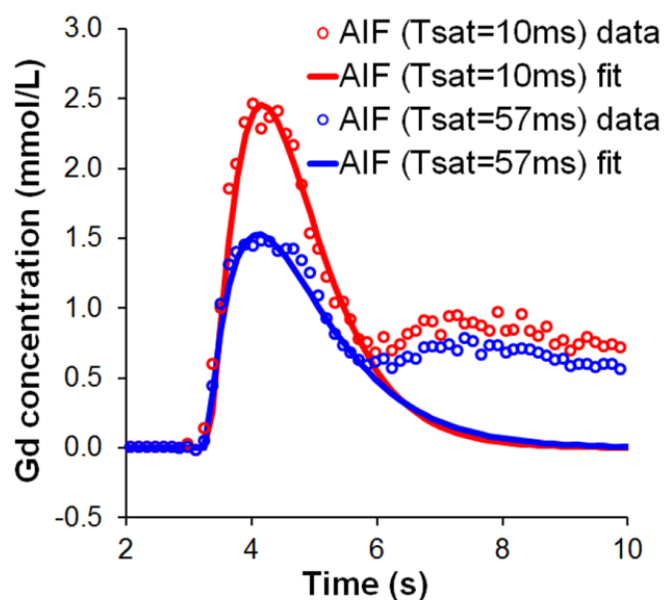
Figure 2.6: Effect of saturation delay on AIF. Example left-ventricular blood pool data and fits obtained from a mouse at rest using a short (10 ms, red circles and solid red line) and a long saturation delay (57 ms, blue circles and solid blue line). These curves demonstrate that the AIF is underestimated when using a long saturation delay.

Table 2.1: Quantitative perfusion values (mean ± standard error) at rest and after Regadenoson administration when AIF is obtained using images with saturation delay 10 ms/57 ms

	Rest	Regadenoson (0.1 µg/g bodyweight)	Perfusion Reserve
Perfusion [ml/g/min] (AIF from images with Tsat = 10 ms)	5.7 ± 0.8	10.4 ± 0.3	2.0 ± 0.3
Perfusion [ml/g/min] (AIF from images with Tsat = 57 ms)	8.6 ± 1.4	18.4 ± 2	2.3 ± 0.4

To demonstrate the ability of the CS-accelerated dual-contrast sequence to quantify regional perfusions, Figure 2.7 shows example regional TF curves obtained from mice at rest and after vasodilation with Regadenoson. Table 2.2 shows the average regional perfusions that were obtained in the mice at rest and after vasodilation. There were no significant differences in the rest and stress perfusion values between the different sectors. Stress perfusion was significantly increased within the same sector ($p < 0.05$ vs. rest).
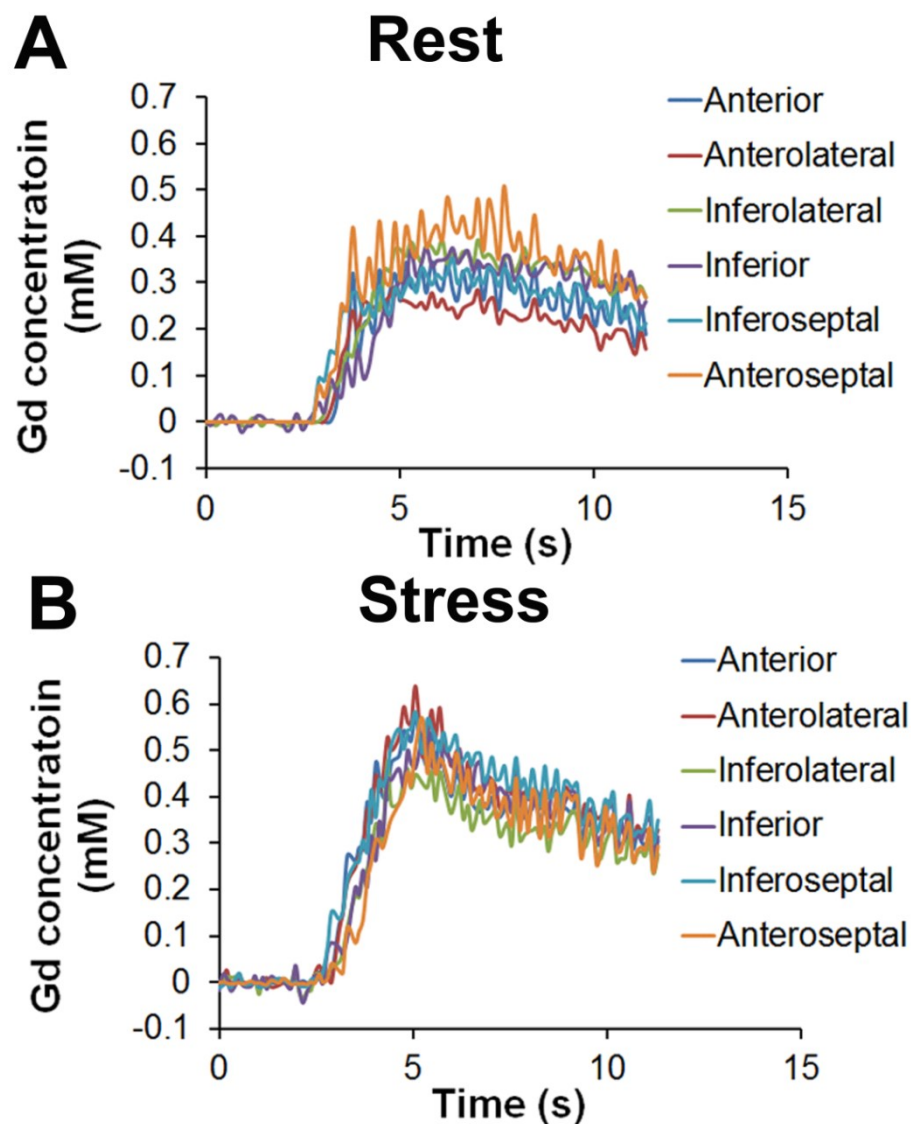
Figure 2.7: Regional tissue function curves obtained from mice. (A): Example regional tissue function curves obtained from a mouse at rest. (B): Example regional tissue function curves obtained from a mouse after vasodilation. The myocardium was divided in 6 sectors (named clockwise starting from the right ventricular insertion point): anterior, anterolateral, inferolateral, inferior, inferoseptal and anteroseptal. These curves demonstrate the ability of the CS-accelerated dual-contrast sequence to assess regional perfusions.

Table 2.2: Regional perfusion values (mean ± standard error) obtained in the different myocardial sectors at rest and after Regadenoson administration

	Anterior	Antero-lateral	Infero-lateral	Inferior	Infero-septal	Antero-septal
Rest	5.9±0.8	6.1±1.8	5.5±0.9	6.5±0.8	6.8±1.0	6.8±0.6
Stress	16.1±1.0[*]	11.3±1.6[*]	10.8±1.1[*]	11.8±0.9[*]	14.3±1.8[*]	13.8±1.5[*]

*p < 0.05 vs. rest perfusion within the same sector

2.3.2. Myocardial perfusion reserve in DIO mice

Using the dual-contrast first-pass sequence with BLOSM reconstruction, we were able to detect reduced MPR in DIO mice fed a HFD for 24 weeks. These results are summarized in Figure 2.8. Baseline perfusion in DIO mice was found to be 5.6 ± 0.4 ml/g/min and this was similar to the baseline perfusion in wild type mice (5.7 ± 0.8 ml/g/min). Stress perfusion was reduced (p<0.05) in DIO mice (7.7 ± 0.4 ml/g/min) as compared to the wild type mice (10.4 ± 0.3 ml/g/min). Thus, MPR was reduced in DIO mice due to reduced stress perfusion. Specifically, MPR was 2.0 ± 0.3 in wild type mice and 1.4 ± 0.2 in DIO mice (p<0.05).
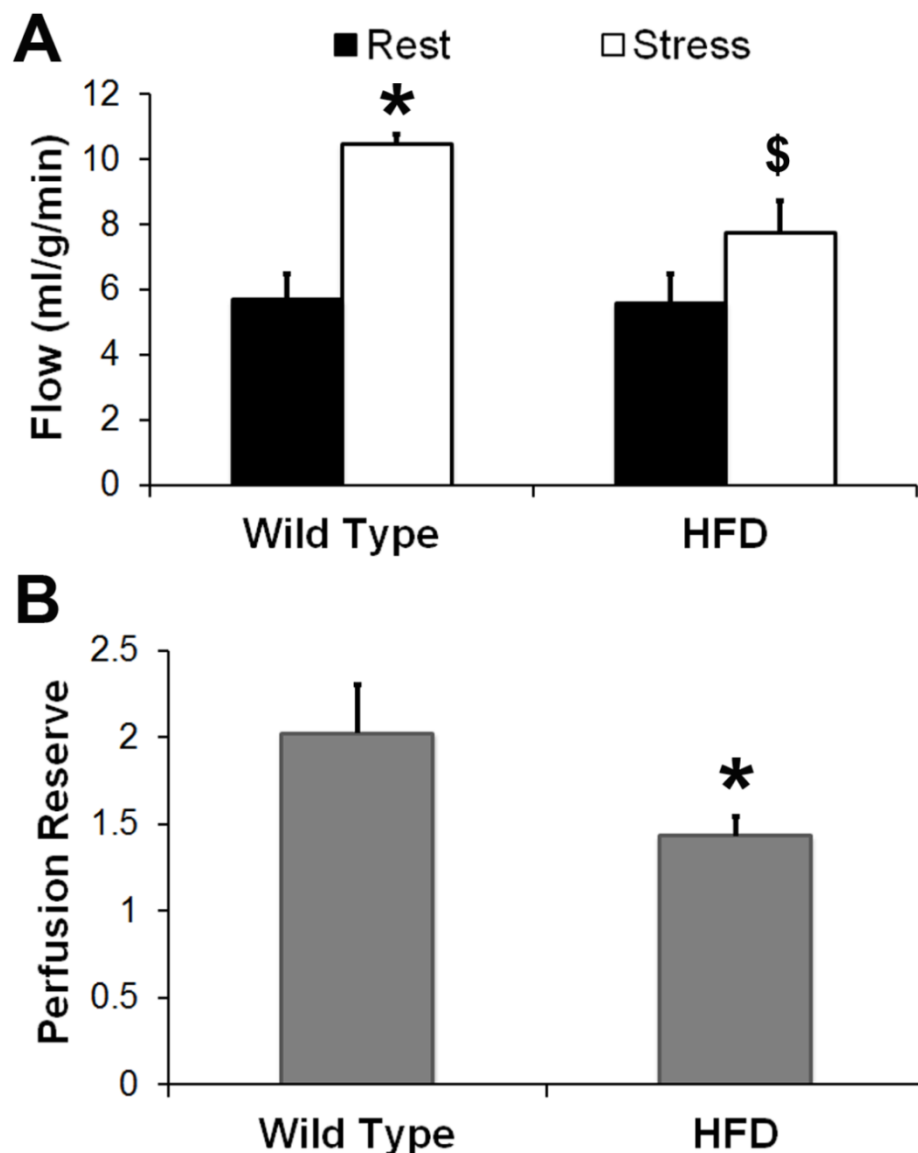
Figure 2.8: Myocardial perfusion and perfusion reserve in high-fat diet mice. (A): Rest and stress MBF results obtained in wild type and HFD mice after 24 weeks of diet. Rest MBF was similar in wild type and HFD mice. Stress MBF was increased in wild type mice (*$p<0.05$ vs. wild type rest perfusion) and was reduced in HFD mice as compared to wild type mice ($$p<0.05$ vs. wild type stress perfusion). (B): MPR results obtained in wild type and HFD mice after 24 weeks diet. MPR was reduced in the HFD mice (*$p<0.05$ vs. wild type).

2.4. Discussion

In this study, we developed a dual-contrast first-pass perfusion MRI method for mice, which allowed sampling of both the AIF and TF within every R-R interval. This method employed a CS-accelerated dual-contrast gradient-echo pulse sequence to acquire undersampled first-pass images and the motion-compensated BLOSM CS reconstruction technique to reconstruct the undersampled free-breathing data in the presence of respiratory motion (109). Using this technique, we measured MBF in mice at rest and with two vasodilators, ATL313 and Regadenoson. We also detected increments in perfusion with increasing doses of Regadenoson and obtained a dose-response curve. Using this method, for the first time we measured a reduction in MPR in DIO mice.

The dual-contrast first-pass MRI sequence enables acquisition of both the AIF and TF using a single gadolinium injection in mice. There are several challenges to performing first-pass imaging in mice. The average mouse heart rate in our study was 455 ± 15 bpm at rest and 563 ± 3 bpm with vasodilation (R-R interval ~ 120 ms at rest and 100 ms with vasodilation). Using a fast saturation-recovery gradient-echo sequence with rectangular FOV and acceleration rates of 6 and 4 for the AIF and TF respectively, the total imaging time was 80 ms/R-R interval. This protocol enabled us to sample both the AIF and the TF every R-R interval, both at rest and with vasodilation. The second challenge was the small size of the mouse heart. The dual-contrast first-pass images were acquired with an in-plane resolution of 200 μm^2, which enabled us to clearly resolve the LV blood pool and myocardium. The third challenge was the free breathing

of the mice, which can introduce artifacts in images. Since mice have a fast systemic circulation time of just a few seconds, it is essential to sample the AIF and TF every heart beat and hence respiratory gating cannot be used. In order to reduce respiratory motion artifacts, we used a recently developed CS reconstruction technique called BLOSM. This technique uses motion tracking to guide the CS sparsity transform and compensates for respiratory motion (109).

In this study, we evaluated the sequence at rest and with two vasodilators, ATL313 and Regadenoson. Regadenoson is an A2A receptor agonist that is used clinically. This agent has been shown to have fewer side effects as compared to adenosine and it can be injected as a bolus before contrast agent administration (116). Our results show the feasibility of using this agent for stress first-pass MRI in preclinical studies. The MBF values obtained at rest and with ATL313 agree closely with our prior ASL data (105). Both ATL313 and Regadenoson provided comparable perfusion values during vasodilation. The peak concentration of Gd-DTPA in the LV blood pool with 0.1 mmol/L.kg body weight dose (bolus concentration = 50mM) was 2.3 ± 0.2 mM. This concentration is similar to the concentration obtained by Nierop *et al*. (1.9 mM) (93), who used a dual-bolus technique in mice with a full bolus concentration of 40 mM. Using the dual-contrast sequence with different doses of Regadenoson, we were able to obtain a dose-response curve. Thus, using this dual-contrast sequence, we were able to measure incremental increases in MBF with incremental doses of Regadenoson until it plateaued at approximately 11 ml/g/min with 0.05 - 0.1 µg/g body weight dose. This result demonstrates that maximal vasodilation was achieved with 0.05 µg/g body weight of Regadenoson.

In this study we also demonstrated the ability of the sequence to quantify regional perfusions. Though there were no statistically significant differences in the rest and stress perfusion values between the different sectors, the perfusion in the anterior wall after vasodilation was slightly increased as compared to the other sectors. The high value in the anterior wall after vasodilation occurs because this area is prone to artifacts related to the nearby ascending and descending aorta, which has very high pulsatile flow after administration of Regadenoson.

Using the dual-contrast first-pass MRI sequence we detected reduced MPR in DIO mice fed a HFD for 24 weeks. A recent study looked at the long-term effects of a HFD in C57Bl/6 mice and showed that these mice exhibit several hallmarks of diabetic cardiomyopathy. In this study they showed that DIO mice fed a HFD for 8 months were overweight, hyperglycemic, insulin resistant, hypercholesterolemic, and hyperinsulinemic, and exhibited cardiomyocyte hypertrophy, cardiac fibrosis and a reduction in cardiac contractile reserve. In addition, these conditions worsened after 16 months of diet (107). Another recent study showed that DIO mice fed a HFD for 5 months have subtly abnormal cardiac mechanics (117). In the present study, we have shown that DIO mice fed a HFD for 24 weeks have reduced MPR, and this is consistent with prior data showing that human diabetic patients have reduced coronary flow reserve, even without obstructive coronary atherosclerosis (6). We also found that the DIO mice were severely overweight as compared to the wild type mice (55 ± 4 g vs. 31 ± 1g, p<0.05) and this is in agreement with prior studies (107,117). As the present study focused on technique development and evaluation, we did not investigate the mechanisms underlying reduced perfusion reserve in the DIO mice.

First-pass contrast-enhanced MRI in mice has only recently been investigated (92-95,106). Coolen *et al.* (92) used a segmented acquisition with parallel imaging to perform first-pass MRI in mice with a temporal resolution of about 300 - 400 ms. They used this method to measure perfusion semi-quantitatively in mice at rest and post – myocardial infarction (MI) and showed that they could detect regional differences in the myocardium post-MI. However, they did not perform absolute quantification. Makowski *et al.* (94) used 10-fold k-t undersampling with a k-t principle component analysis image reconstruction technique to perform first-pass MRI in mice at rest and post-MI. They measured perfusion both semi-quantitatively and using Fermi-function deconvolution and reported MBF of 7.3 ± 1.5 ml/g/min in mice at rest, 7.1 ± 1.5 ml/g/min in the post-infarct remote myocardium and a reduced perfusion of 1.2 ± 0.8 ml/g/min in the infarcted segments of the myocardium. Our resting MBF value of approximately 5.7 ml/g/min is approximately 25% lower than Makowski's value. This difference could be due to the slightly lower isoflurane level used in our study (1.25% in our study vs. 1.4% in Makowski *et al.*), as isoflurane is known to be a potent vasodilator and has specifically been shown to increase MBF in the mouse heart (98). In addition, Makowski *et al.* did not use a dual-bolus or dual-contrast technique, but rather assessed both the TF and AIF from a single slice acquired at a saturation delay of 100ms. Using our methods for computing MBF, we demonstrated that MBF will be overestimated using a single slice for the AIF and TF with a 100 ms delay. Jogiya *et al.* (95) used essentially identical methods as Makowski *et al.* to measure perfusion semi-quantitatively and used Fermi function deconvolution in mice at rest and after vasodilation with dipyridamole. They reported a resting MBF of 4.1 ± 0.5 ml/g/min that

increased to 9.6 ± 2.5 ml/g/min after hyperemia, yielding a perfusion reserve of 2.4 ± 0.54. Our rest and stress perfusion estimates are somewhat higher than the values reported in that study. Nierop *et al.* (93) used a dual-bolus approach to measure resting MBF in a cohort of 9 C57Bl6 mice, where the AIF was measured using a separate acquisition with a low dose of Gd-DTPA. They reported a mean MBF of 7.3 ± 0.9 ml/g/min at rest and demonstrated good repeatability of the method for measuring resting MBF in mice. Our measurement of resting MBF is lower than that reported in their study and this is likely due to the higher isofluorane level used in their study (1.5-2% vs. 1.25 % in our study).

Prior studies have measured MBF quantitatively in mice using other techniques such as arterial spin labeling (ASL) (77,97,98,100,101) and microspheres (118-120). Previously published studies using other techniques reported mean resting MBF of 4.3 – 7 ml/g/min and stress MBF of 8.2 – 14 ml/g/min in mice. Our perfusion estimates are centered within the ranges of these published values. The large variation in stress perfusion values is because of the different vasodilators and different doses used in the various studies. Our data is in good agreement with prior ASL data acquired in mice at rest (77,105) and after administration of ATL313 (105). Since ASL requires longer acquisition times and perfusion estimation using microspheres is a terminal experiment in mice, first-pass MRI has significant advantages compared to both of these methods. Because first-pass MRI is performed so rapidly, it can easily be integrated into a comprehensive cardiac MRI exam for mice that assesses left-ventricular anatomy, function (70), strain (72,80), and late gadolinium enhancement (55).

A limitation of this study is that no additional independent perfusion measurements were performed to validate the dual-contrast first-pass MRI technique. However, our perfusion estimates are within the ranges of previously published values. Another limitation is that our current imaging protocol only allows for perfusion measurement in a single slice. Increasing slice coverage is an important challenge for future technical development, which may be facilitated by using short echo-planar (121) or spiral trajectories (122). Image resolution may further be improved by using other k-space trajectories like radial or spiral, and by using higher acceleration rates possibly with phased-array coils and combining compressed sensing with parallel imaging (91). A further limitation of this study is that the dose-response studies were not all performed in the same set of mice and a separate set of mice was used for perfusion estimation using ATL313. In this manuscript, we have not studied perfusion in infarcted mice, however other groups have used first-pass MRI to image perfusion in post-infarct mice (94,106). The heart rate in wild type C57Bl6 mice on day 1 post-infarct is typically around 550 – 600 bpm (77), which is similar to the heart rate we observed after vasodilation in non-infarcted mice (563 ± 3 bpm). Given that the acquisition time for our dual-contrast sequence is 80 ms (using the sequence parameters stated in this study), we would not expect major problems in measuring perfusion in an acute infarct mouse model using the CS-accelerated dual-contrast sequence. However, in chronic infarcts after wall thinning occurs, the image resolution may be insufficient to accurately measure perfusion in the infarct scar.

2.5. Conclusions

In conclusion, k_y-t undersampled dual-contrast first-pass MRI with BLOSM reconstruction provides the spatial resolution, temporal resolution, and motion compensation suitable for quantifying myocardial perfusion in free-breathing mice using a single injection of a contrast agent. The dual-contrast approach uses separate slices with short and long saturation delays, and provides accurate measurements of MBF. With these methods, the scan time is sufficiently short so as to allow first-pass imaging at either rest or stress with vasodilation, providing for the assessment of MPR. Furthermore, we measured reduced MPR in DIO mice, which establishes an additional important abnormal parameter in this emerging mouse model of human diabetic cardiomyopathy. These techniques applied in gene-modified mice may be used to study mechanisms that underlie abnormal perfusion in cardiovascular diseases such as obesity and diabetes.

2.6. Acknowledgements

We thank Li-ming Gan, M.D. for insightful discussions on perfusion imaging in mouse models of heart disease.

Chapter 3: Repeatability and Variability of Perfusion

Imaging Techniques: First-Pass MRI and ASL in Mice

3.1. Introduction

The assessment of myocardial blood flow (MBF), or perfusion, is central to the evaluation of ischemic heart disease. Blood flow is markedly reduced in myocardial infarction, and the recovery of blood flow to injured tissue is critical to infarct healing and to emerging strategies for cardiac regeneration. Abnormal myocardial perfusion reserve (MPR), the ratio of blood flow at stress compared to rest, is widely used to evaluate ischemia and detect obstructive coronary artery disease (CAD). MPR can also be reduced in the absence of obstructive CAD (3,123,124), such as in diabetes (6,124), obesity (8), the metabolic syndrome (7), and other conditions where microvascular dysfunction limits the ability to augment MBF. Reduced MPR is prognostic of adverse cardiac events in patients with and without obstructive CAD (6), and in many diseases involving microvascular dysfunction the molecular and cellular mechanisms underlying reduced MPR are not well understood.

Preclinical research across the full spectrum of heart diseases, including infarct healing, cardiac regeneration, and microvascular disease, is largely performed in small animals such as mice and rats. Recent examples where quantitative MRI of MBF provided critical data include a study by Zhang *et al.* (125) where MRI quantified temporal changes in MBF after transplantation of endothelial cells to the infarcted heart, a study by Banquet *et al.* (126) where MRI perfusion imaging demonstrated the therapeutic benefit of a growth factor combination therapy in a chronic heart failure mouse model, and a study by Hiller *et al.* (127) where MRI showed an improvement in microvascular function after treatment with a tissue specific ACE inhibitor after coronary stenosis.

Two different MRI methods, first-pass contrast-enhanced MRI and arterial spin labeling (ASL), can both be used to quantify MBF in small animals. Although first-pass contrast-enhanced imaging is the MRI method of choice to assess myocardial perfusion in humans, due to technical limitations, until recently the clearly superior option for imaging myocardial perfusion in small animals was arterial spin labeling (ASL). More recently, with the development of acceleration methods, first-pass perfusion imaging has become technically feasible in mice and rats, and first-pass methods that quantify MBF in small animals have recently been reported (92-95,103). Since two methods, ASL and first-pass contrast-enhanced MRI, are now available, we sought to evaluate them for imaging MBF in mice over a wide range of blood flows, and to compare their advantages and disadvantages under a variety of conditions. The specific purpose of this study was to compare the repeatability and variability of ASL and first-pass MRI for quantifying myocardial perfusion in mice under a range of conditions.

3.2. Methods

3.2.1. Experimental Design

Wild-type male C57Bl/6 mice (n = 7) were imaged at rest, with vasodilation using Regadenoson (Lexiscan, Astellas Pharmis, 0.1 µg/g body weight) and after myocardial infarction (MI), representing conditions of intermediate, high, and low MBF, respectively. Under each condition, mice were imaged using both a first-pass sequence (103) and an ASL sequence. To assess repeatability, perfusion imaging for each technique was

performed at two different sessions. The repeated rest and stress imaging sessions were separated by approximately one week in order to allow the mice sufficient time to recover between imaging sessions. The infarcted mice underwent the two sessions on day 1 and day 2 post-MI in order to allow sufficient time for Gd to wash out from the infarcted tissue and to minimize changes in perfusion due to infarct healing. Perfusion estimates at rest, stress and post-MI obtained using both techniques were compared for between-session repeatability, intra-user and inter-user variability and inter-animal variability. Overall image quality of the perfusion images was also assessed by two readers using a 5 point scale (1-very poor, 2-poor, 3-good, 4-very good, 5-excellent), where judgment of high quality was largely influenced by low levels of aliasing and motion artifacts.

3.2.2. Animal Handling

All animal studies were performed under protocols that comply with the Guide for the Care and Use of Laboratory Animals (NIH publication no. 85-23, Revised 1996) and were approved by the Animal Care and Use Committee at our institution. An indwelling tail vein catheter was established to deliver gadolinium (Magnevist, 0.1 mM/kg body weight) and Regadenoson. Mice were positioned supine in the scanner, body temperature was maintained at 36 ± 0.5^0C and anesthesia was maintained at 1.25 % isoflurane in O_2 during imaging. The ECG, body temperature and respiration were monitored during imaging using an MR-compatible system (SA Instruments, Stony Brook, New York). MI was induced by permanent ligation of the left anterior descending coronary artery as described previously (128).

3.2.3. MRI Hardware

MRI was performed on a 7T Clinscan system (Bruker, Ettlingen, Germany) equipped with actively shielded gradients with a full strength of 650 mT/m and a slew rate of 6666 mT/m/ms. A 30 mm diameter birdcage RF coil was also used.

3.2.4. MRI Pulse sequences and Imaging Protocol

3.2.4.1.   ASL

ASL was performed using a compressed sensing (CS) accelerated spiral flow-sensitive alternating inversion-recovery (FAIR) Look-Locker sequence. This sequence is an accelerated version of a cardio-respiratory gated (CRG) FAIR ASL sequence, which was previously described and used to measure perfusion in the mouse heart at rest, with vasodilation and post-MI (77). Using this sequence, upon detection of a CRG trigger, a non-selective or slice-selective inversion was performed. For 50-60 triggers after the inversion, an RF pulse was applied and a spiral gradient echo was acquired. Imaging parameters included: acceleration rate = 2, time between inversions = 7 s, slice thickness = 1 mm, number of spiral interleaves for full Nyquist sampling = 87, pixel size = 100 x 100 μm^2, averages = 3. A hyperbolic secant RF pulse was used for inversion. A 3° RF excitation pulse was used to minimize perturbation of recovering longitudinal magnetization. The total acquisition time for one session of CS-accelerated ASL was about 40 min.

In all mice, localizer cine imaging was performed to select a mid-ventricular short-axis slice. Rest ASL imaging was performed first, followed by stress ASL. For

stress ASL imaging, Regadenoson was injected i.v. and about 7-10 minutes later, the slice selective acquisition was performed followed by the non-selective acquisition.

3.2.4.2.   First-Pass MRI

First-pass MRI was performed using a CS accelerated dual-contrast saturation-recovery gradient echo sequence that has recently been described in detail (103). Briefly, two short-axis slices (slice gap = 0.2 mm) were acquired within each cardiac cycle, one to obtain the arterial input function (AIF) and the other to obtain the tissue function (TF). Pulse sequence parameters included: FOV = 25.6 x 18 mm^2, phase resolution = 80%, matrix = 128 x 74, nominal pixel size = 200 µm^2, TE/TR = 1.2/2.1 ms, excitation flip angle = 15^0, slice thickness = 1 mm, AIF saturation delay = 15 ms, TF saturation delay = 57 ms, acceleration rate = 6 for AIF and 4 for TF, AIF acquisition time = 25ms/image and TF acquisition time = 36 ms/image. 12 phase-encode lines were acquired for each AIF image and 17 lines were acquired for each TF image. For the AIF images centric k-space filling was used to achieve a short saturation delay, while for the TF images linear k-space filling was used.

In all mice, localizer cine imaging was performed to select a mid-ventricular short-axis slice. A series of 250 first pass images were acquired using the dual-contrast sequence. Ten seconds after the acquisition started, the contrast agent was injected i.v. while imaging continued in order to capture the first-pass kinetics. For the stress-perfusion acquisition, Regadenoson was injected i.v. and first-pass imaging was performed 10 minutes later.

3.2.5. Compressed Sensing Reconstruction

First-pass MRI and ASL both utilized data undersampling for acceleration, and both were reconstructed using a recently-developed CS algorithm called Block LOw-rank Sparsity with Motion-guidance (BLOSM) (109). This method applies low rank sparsity to regions of images, and can also use inter-frame region tracking for motion compensation. BLOSM with motion compensation was used to reconstruct the undersampled free-breathing first-pass images, and BLOSM without motion compensation was used to reconstruct the CRG undersampled ASL images. The advantages of regional low rank sparsity for perfusion imaging have been described previously (110).

3.2.6. Image Analysis

Tracer-kinetic modeling was used to quantify MBF from both first-pass and ASL images. For first-pass perfusion analysis, the signal intensity – time curve for the AIF was generated by placing a region of interest (ROI) in the LV blood pool in the images acquired using a short saturation delay. Similarly, the signal intensity – time curve for the TF was generated by placing a ROI in the myocardial tissue in the images acquired using the longer saturation delay. The signal intensities of the T1-weighted first-pass images were normalized by the signal intensities of proton density images (acquired at the end of the first-pass acquisition) and then converted into T1 values using methods described by Cernicanu and Axel (38). The relaxivity of gadolinium was assumed to be 3.8 L/mmol.s, which was then used to convert the T1 values to gadolinium concentrations. The AIF curve was fit using a gamma-variate function in order to

denoise the data and remove the effects due to recirculation of gadolinium. Using data representing first-pass kinetics (but not recirculating gadolinium), the fitted AIF and TF were analyzed using Fermi function deconvolution (41) to estimate myocardial perfusion (103).

For ASL analysis, ROIs comprising the myocardial tissue of the Look-Locker images acquired after slice-selective (SS) and non-selective (NS) inversions were used to generate signal intensity-time curves ($S_{SS}(t)$ and $S_{NS}(t)$). The blood signal intensity-time curve ($S_b(t)$) was measured by placing a ROI in the LV blood pool of the non-selective images. $T1_{NS}$, $T1_{SS}$ and $T1_{blood}$ were estimated by fitting $S_{NS}(t)$, $S_{SS}(t)$ and $S_b(t)$ to a two- parameter exponential curve (Eq. 1) using a non-linear least squares fitting algorithm.

$$S(t) = S_0 \left(1 - 2 \times exp\left(\frac{-t}{T_1}\right) \right) \qquad \text{(Eq. 1)}$$

In this equation, S(t) denotes the signal intensity and S_0 is the proton density. The proton densities for the myocardium and blood were also determined from the two-parameter fits. The signal intensities for the myocardium ($S_{NS}(t)$, $S_{SS}(t)$) and blood ($S_b(t)$) were then normalized by the respective proton densities (S_0) to generate longitudinal magnetization-time curves for myocardium ($M_{NS}(t)$ and $M_{SS}(t)$) and blood ($M_b(t)$). Cubic splines were then used to interpolate $M_{NS}(t)$ and $M_{SS}(t)$ in time, and the difference curve, D(t) was then generated using the difference between the spline fits of $M_{NS}(t)$ and $M_{SS}(t)$. D(t) was then fit to an ASL kinetic model (derived in section 3.2.7) in order to estimate perfusion. If we define T_{1app} as the apparent T_1 of the myocardium given by

$$\frac{1}{T_{1app}} = \frac{1}{T_1} + \frac{f}{\lambda},$$ then, using the kinetic model, the difference function D(t) can be

written as:

$$D(t) = 2fS_B^0 W(t)e^{-t/_{T1B}} * e^{-t/_{T1app}} \text{ where } W(t) = \int_{\tau=0}^{t} h(\tau)d\tau \text{ and } h(t) = (t - t_{delay})^\alpha e^{-(t-t_{delay})/_\beta}$$

where f is flow in s^{-1}, S_B^0 is the proton density of blood, λ =0.95 is the blood/tissue water

partition coefficient, T_{1B} is the relaxation time constant of blood, W(t) is the input

function, and h(t) is the blood-transit time distribution (dispersion function) that takes

the form of a gamma-variate. For h(t), α determines the upslope, β determines the

decay of h(t) and t_{delay} is the transit delay. All image analysis was performed using

MATLAB (The Mathworks, Natick, MA, USA). The derivation of this model is given in

the following section.

3.2.7. ASL Quantitative Perfusion Analysis

Multi-inversion-time ASL data were analyzed using a kinetic model based on the

formalism developed by Hrabe *et al.* (54) which we modified to use a gamma-variate

function to describe the distribution of transit times for arterial water flowing through the

coronary arterial circulation. The gamma-variate distribution has for many years been

used to model blood flow through vascular beds (129-131), and was recently applied to

ASL of the heart (105) and brain (132). Here we develop an expression for the ASL

signal, which is the difference between the magnetization sampled after a slice-selective

inversion and a nonselective inversion. Optimal fitting of this expression to the acquired

data enables the computation of MBF.

3.2.7.1. Theory

The Bloch equations for longitudinal magnetization in the presence of perfusion can be written as follows (133):

$$\frac{dM}{dt} = \frac{M_0 - M(t)}{T_1} + fM^A(t) - \frac{f}{\lambda}M(t)$$

where M(t) is the longitudinal magnetization of the tissue, M_0 is the equilibrium tissue magnetization, M^A(t) is the longitudinal magnetization of the inflowing blood, f is the flow in s^{-1}, λ =0.95 is the blood/tissue water partition coefficient and T_1 is the relaxation time constant of myocardium. Here the first term accounts for T_1 relaxation, the second term accounts for the inflow of arterial water, and the third term accounts for outflow.

The ASL approach employed in this study uses a FAIR preparation scheme, where the tagged image is acquired after application of a slice-selective inversion, and the control image is acquired after application of a nonselective inversion. The equations for tissue longitudinal magnetization after a slice-selective (M_{SS}) and nonselective (M_{NS}) inversion can be written as:

$$\frac{dM_{SS}}{dt} = \frac{M_0 - M_{SS}(t)}{T_1} + fM^A_{SS}(t) - \frac{f}{\lambda}M_{SS}(t), \qquad M_{SS}(0) = 0$$

$$\frac{dM_{NS}}{dt} = \frac{M_0 - M_{NS}(t)}{T_1} + fM^A_{NS}(t) - \frac{f}{\lambda}M_{NS}(t), \qquad M_{NS}(0) = 0$$

where M^A_{SS} (t) and M^A_{NS} (t) are the arterial blood magnetizations after slice-selective and a nonselective inversions, respectively.

Following the formalism of Hrabe *et al.* (54), if we define the difference function *D(t)* = *M~SS~(t)* – *M~NS~(t)*, then the differential equation for the difference function can be written as follows:

$$\frac{dD(t)}{dt} = \frac{dM_{SS}}{dt} - \frac{dM_{NS}}{dt}, \quad D(0) = 0$$

This can then be rewritten using the respective equations for $M_{SS}(t)$ and $M_{NS}(t)$ as :

$$\frac{dD(t)}{dt} = \frac{M_{NS}(t) - M_{SS}(t)}{T_1} + f\left(M_{SS}^{A}(t) - M_{NS}^{A}(t)\right) - \frac{f}{\lambda}\left(M_{SS}(t) - M_{NS}(t)\right)$$

$$\therefore \frac{dD(t)}{dt} = -\frac{D(t)}{T_1} + f\left(M_{SS}^{A}(t) - M_{NS}^{A}(t)\right) - \frac{f}{\lambda}D(t) = -D(t)\left(\frac{1}{T_1} + \frac{f}{\lambda}\right) + f\left(M_{SS}^{A}(t) - M_{NS}^{A}(t)\right)$$

Using $\dfrac{1}{T_{1app}} = \left(\dfrac{1}{T_1} + \dfrac{f}{\lambda}\right)$ and $D^{A}(t) = f\left(M_{SS}^{A}(t) - M_{NS}^{A}(t)\right)$, the above equation can be shortened as :

$$\frac{dD(t)}{dt} + \frac{D(t)}{T_{1app}} = fD^{A}(t)$$

where T_{1app} is the apparent T1 of the tissue.

For the slice-selective scan, the incoming arterial blood is not inverted, while for the nonselective scan the incoming arterial blood is inverted. Thus $D^{A}(t)$ can be rewritten as follows:

$$D^{A}(t) = f\left(M_{SS}^{A}(t) - M_{NS}^{A}(t)\right) = f\left(M_{B}^{0}W(t) - M_{B}^{0}W(t)\left(1 - 2e^{-t/T_{1B}}\right)\right)$$

where M^0_B is the proton density of blood, W(t) describes the arterial blood input function and T_{1B} is the T_1 relaxation constant for blood. The equations can then be solved as follows:

$$D^A(t) = 2fM^0_B W(t)e^{-t/T_{1B}}$$

The differenti al equation for the difference equation as described above was

$$\frac{dD(t)}{dt} + \frac{D(t)}{T_{1app}} = D^A(t)$$

To sove the above equation, we multiply it by integratin g Factor : $e^{t/T_{1app}}$

$$\frac{d\left(D(t)e^{t/T_{1app}}\right)}{dt} = D^A(t)e^{t/T_{1app}}$$

$$D(t) = 2fM^0_B \int_0^\infty W(\tau)e^{-\tau/T_{1B}} e^{-(t-\tau)/T_{1app}} d\tau$$

$$\Rightarrow D(t) = 2fM^0_B W(t)e^{-t/T_{1B}} * e^{-t/T_{1app}}$$

where $*$ stands for convolutio n operation

If we assume the impulse response is a gamma - variate function

$$h(t) = (t - t_{delay})^\alpha e^{-(t-t_{delay})/\beta} \text{ and } W(t) = \int_{\tau=0}^t h(\tau)d\tau$$

then the gamma- variate-based solution to the ASL equation can be shown to be:

$$D(t) = 2fM_B^0 W(t)e^{-t/T_{1B}} * e^{-t/T_{1app}} \text{ where } W(t) = \int_{\tau=0}^{t} h(\tau)d\tau \text{ and } h(t) = (t - t_{delay})^\alpha e^{-(t-t_{delay})/\beta}$$

For these equations, *h(t)* is the blood transit time distribution with the form of a gamma-variate, α determines the upslope of *h(t)*, β determines the decay of *h(t)*, and t_{delay} determines the transit delay of *h(t)*. By measuring *D(t)* = $M_{SS}(t)$ − $M_{NS}(t)$ using Look-Locker or multi-TI ASL and performing an optimal 4- parameter fit of *D(t)*, MBF and *h(t)* can be determined.

3.2.8. Repeatability and data variability

Bland-Altman analysis was used to compare the between-session repeatability and the intra- and inter-user variability of the two techniques. The Bland-Altman repeatability coefficient (RC) which represents the 95% confidence interval of the differences in perfusion estimates between sessions was calculated and normalized to the mean perfusion estimate and expressed as a percentage. The coefficient of variability (CV) is defined as the standard deviation of the datasets normalized by the mean value and expressed as a percentage.

The between-session CV (CV_{bs}) was calculated for each animal by comparing the perfusion estimates between session 1 and session 2 and the mean CV_{bs} and standard error of mean (SEM) was expressed for both the techniques.

The perfusion estimates from both sessions were analyzed by the same user twice and the mean and SEM for the intra-user CV ($CV_{intra-user}$) was calculated by comparing the perfusion estimates between the two analysis sessions. Similarly, all the

datasets were analyzed by two different users and the inter-user CV ($CV_{inter-user}$) was calculated by comparing the perfusion estimates between the two users.

The inter-animal CV (CV_a) for each session was calculated by normalizing the standard deviation of perfusion values from different animals to the mean perfusion value of that session. Using CV_a from both the sessions, a mean and SEM was estimated for both first-pass MRI and ASL.

3.2.9. Statistical Analysis

All values in the text, tables and figures are expressed as mean ± SEM. The between-session CV, intra-user CV, and inter-user CV of the two techniques were compared using one-way analysis of variance. Image quality scores were compared using the Mann-Whitney rank-sum test. P<0.05 was considered to be statistically significant.

3.3.   Results

3.3.1. ASL

Example Look-Locker images at multiple inversion times after application of a slice-selective inversion RF pulse obtained from a mouse and reconstructed using BLOSM are shown in Figure 3.1 (A-D). These images represent typical image quality from the present study.   Figure 3.2A shows example longitudinal magnetization

relaxation curves for the myocardium obtained from a mouse at rest after non-selective (NS, blue circles) and slice-selective (SS, red circles) inversions. Figure 3.2B shows example NS and SS longitudinal relaxation curves obtained from a mouse after vasodilation. Figure 3.2C shows example difference curves and fits to the kinetic model for mice at rest (blue) and after vasodilation (red). A greater difference between the SS and NS curves is easily observed at vasodilation compared to rest. Figure 3.2D shows an example perfusion map obtained from a mouse at rest.
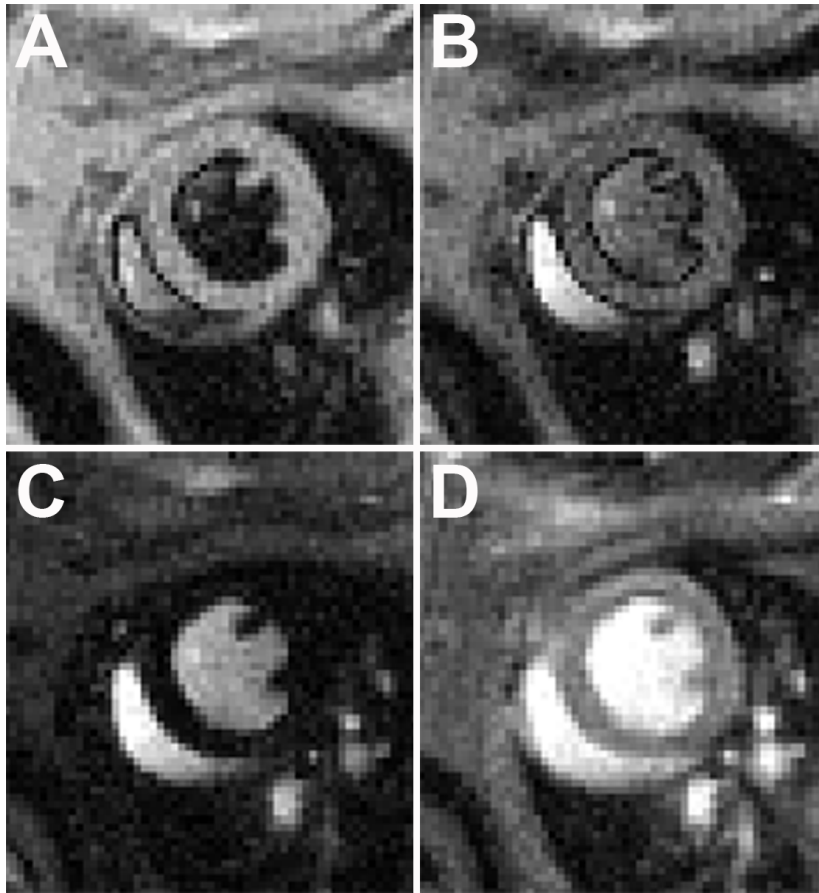
Figure 3.1: ASL images from a mouse heart. (A-D): Example CS-accelerated Look-Locker ASL images obtained from a mouse at rest and reconstructed using BLOSM.
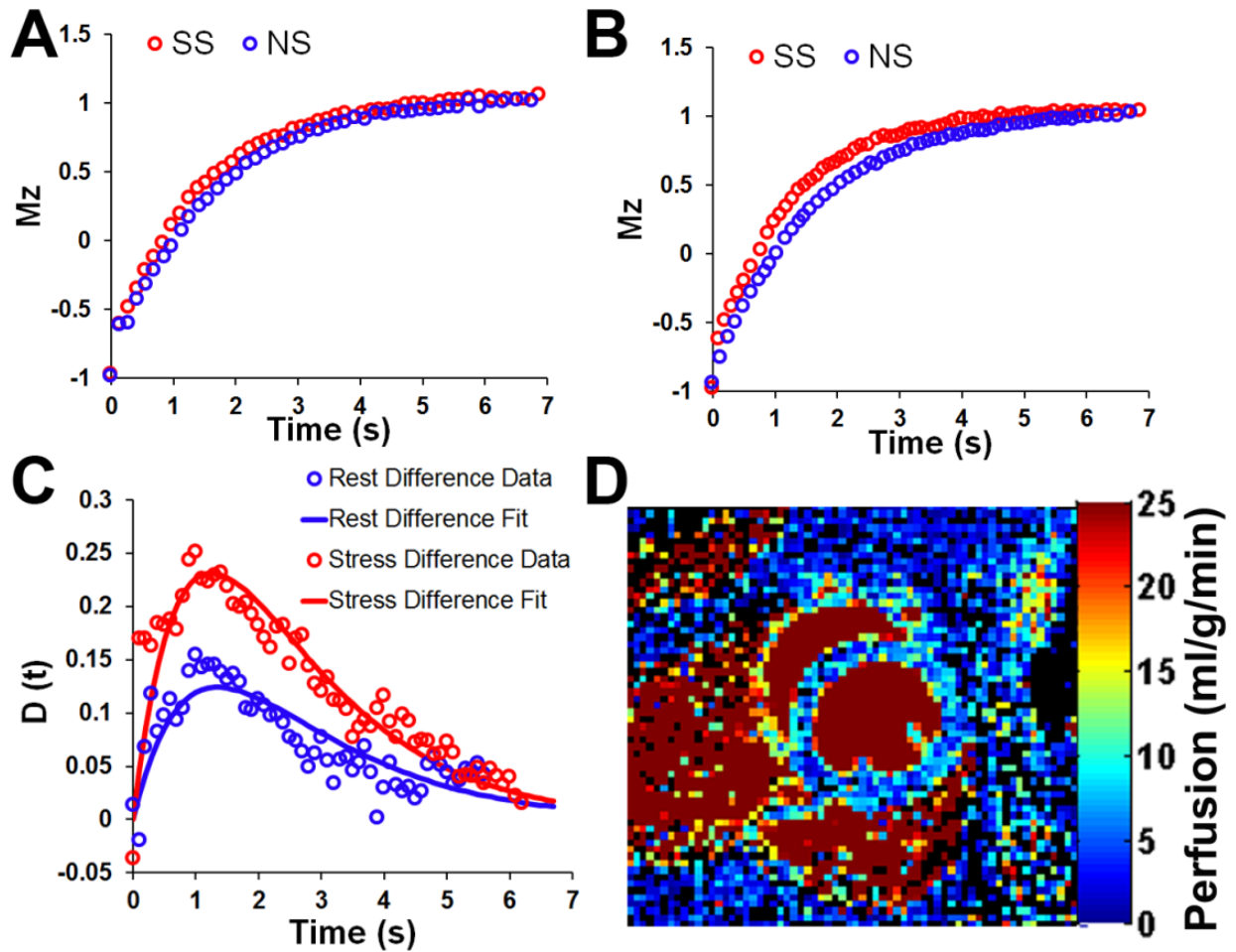
Figure 3.2: Quantification of perfusion using ASL. (A): Representative myocardial longitudinal magnetization curves obtained from a mouse at rest after a non-selective (blue circles) and slice-selective (red circles) acquisition. (B): Representative myocardial longitudinal magnetization curves obtained from a mouse after vasodilation after a non-selective (blue circles) and slice-selective (red circles) acquisition. The slice-selective T1 is reduced after vasodilation. (C): Example difference data and fits to the kinetic ASL model obtained from a mouse at rest (blue) and at stress (red). (D): Example pixel-by-pixel perfusion map obtained using CSASL from a mouse at rest.

3.3.2. First-Pass MRI

Figure 3.3 (A-D) shows example first-pass images obtained from a mouse at rest using the CS-accelerated dual-contrast sequence and reconstructed using the BLOSM technique. Figure 3.4A shows example AIF (blue) and TF (red) data and fits obtained from a mouse at rest. Figure 3.4B shows example TF data and fits obtained from mice at rest (blue) and after vasodilation (red), and Figure 3.4C shows an example perfusion map obtained from a mouse at rest.
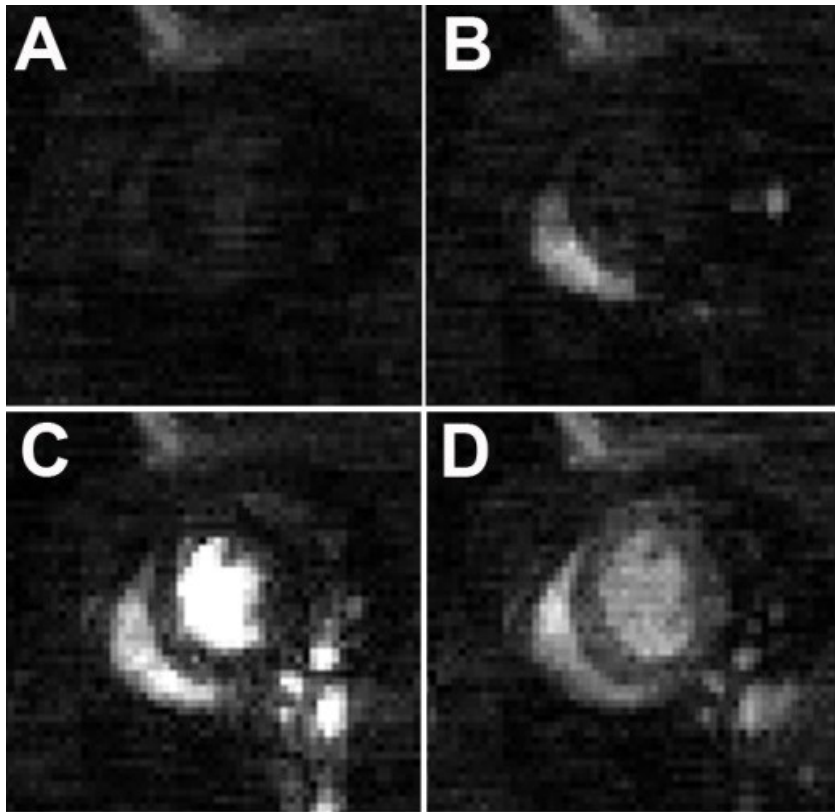
Figure 3.3: First-pass images from a mouse heart. (A-D): Example CS-accelerated dual-contrast first-pass MR images obtained from a mouse at rest and reconstructed using BLOSM.
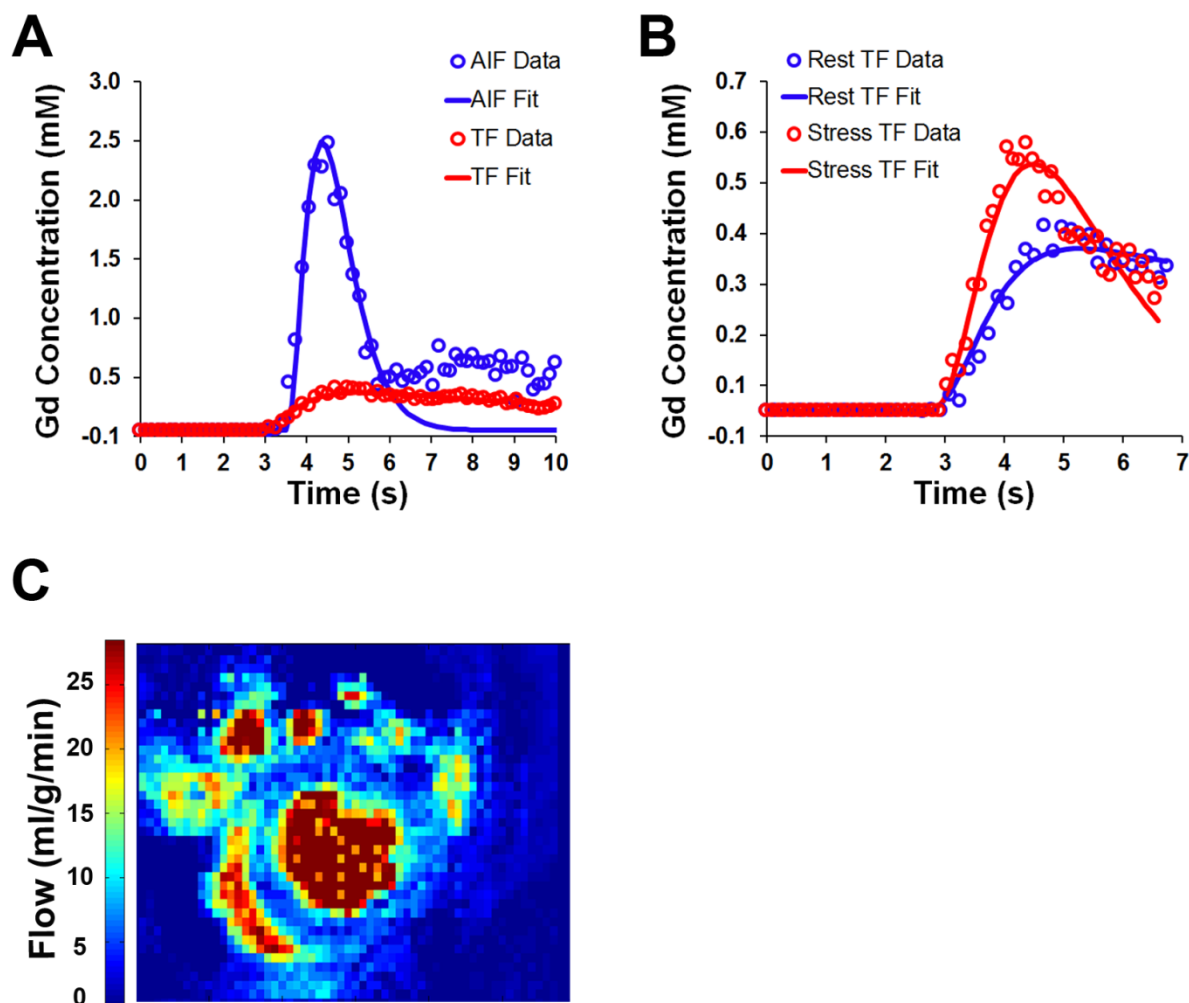
Figure 3.4: Quantification of perfusion using first-pass MRI. (A): Example arterial input function (AIF, blue) and tissue function (TF, red) data and fits obtained from a mouse at rest. (B): Example TF data and fits obtained from a mouse at rest (blue) and at stress (red). (C): Example pixel-by-pixel perfusion map obtained using first-pass MRI from a mouse at rest.

3.3.3. Perfusion values and image quality results

The mean rest, stress, post-MI infarct zone and remote zone perfusion estimates obtained using the ASL and first-pass methods are summarized in Figure 3.5. As can be seen from the figure, the absolute perfusion values obtained using first-pass MRI are lower than the values obtained using ASL. Previously published studies reported mean resting MBF of 4.1 – 7.3 ml/g/min (77,93-95,98,100-103) and stress MBF of 8.2 – 16.9 ml/g/min (77,95,96,98,102,103) in mice, and our perfusion estimates for both techniques are within the ranges of these published values. The image quality (IQ) scores from the two readers are shown in Table 3.1. The IQ was higher for ASL than first-pass for all conditions and both readers ($p < 0.05$).
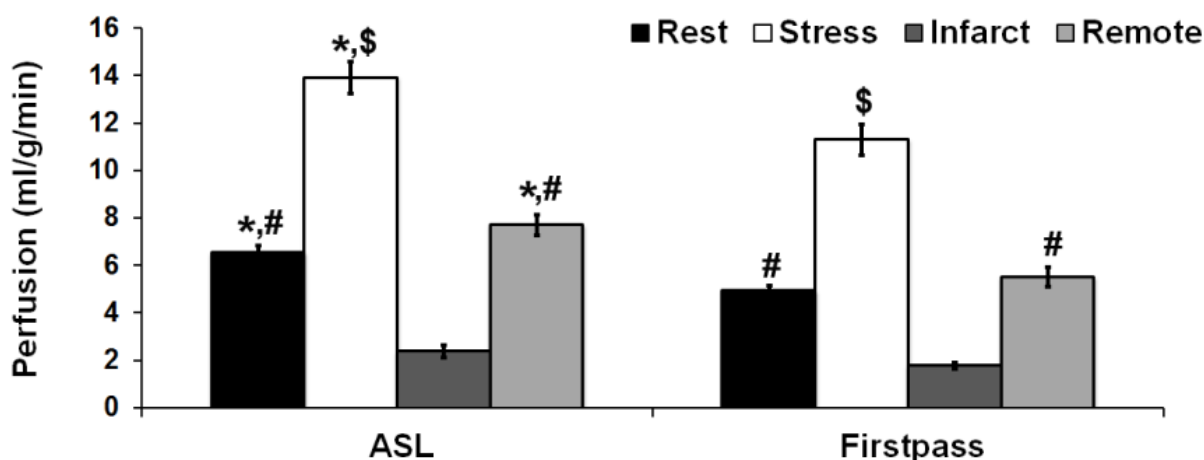
Figure 3.5: Perfusion values with ASL and First-pass MRI in mice. Perfusion results obtained in wild-type mice at rest, stress, in infarct zone and remote zone using both CSASL (analyzed with the kinetic ASL model) and CS-accelerated first-pass MRI technique (*p <0.05 vs. first-pass, #p < 0.05 vs. Infarct using same technique, $p <0.05 vs. rest, infarct and remote using the same technique).

Table 3.1: Image quality scores for both the techniques

		First-pass MRI	**ASL**
Reader 1	**Rest**	3.07 ± 0.20	3.86 ± 0.21*
	Stress	2.14 ± 0.18	3.71 ± 0.19*
	Infarct	3.36 ± 0.23	4.00 ± 0.28*
Reader 2	**Rest**	3.36 ± 0.23	4.00 ± 0.28
	Stress	2.43 ± 0.23	3.5 ± 0.23*
	Infarct	3.21 ± 0.24	4.14 ± 0.21*

* $p < 0.05$ vs. First-pass MRI

3.3.4. Repeatability and between-session coefficient of variability

Bland-Altman plots of between-session repeatability are used to illustrate the mean difference in perfusion between sessions and to compute the RC. These Bland-Altman plots for our between-session ASL and first-pass data are shown in Figure 3.6A and Figure 3.6B, respectively. The overall RC (including the rest, stress, infarct and remote data) was similar for both techniques, with RC = 55% for both ASL and first-pass MRI. The RC estimates for ASL and first-pass under specific conditions of infarct (low flow), rest (normal flow), and stress (high flow) are summarized in

Table 3.2. For ASL, RC decreased with increasing flows. For first-pass MRI, RC was fairly similar at rest, stress and in the post-MI remote zone, however it was higher in infarcted regions. When comparing ASL and first-pass imaging, we found that RC was much lower with first-pass than ASL in the low blood-flow condition (infarct), slightly lower with first-pass compared to ASL in mid-range flows such as rest, and comparable in high blood flow conditions (vasodilation).
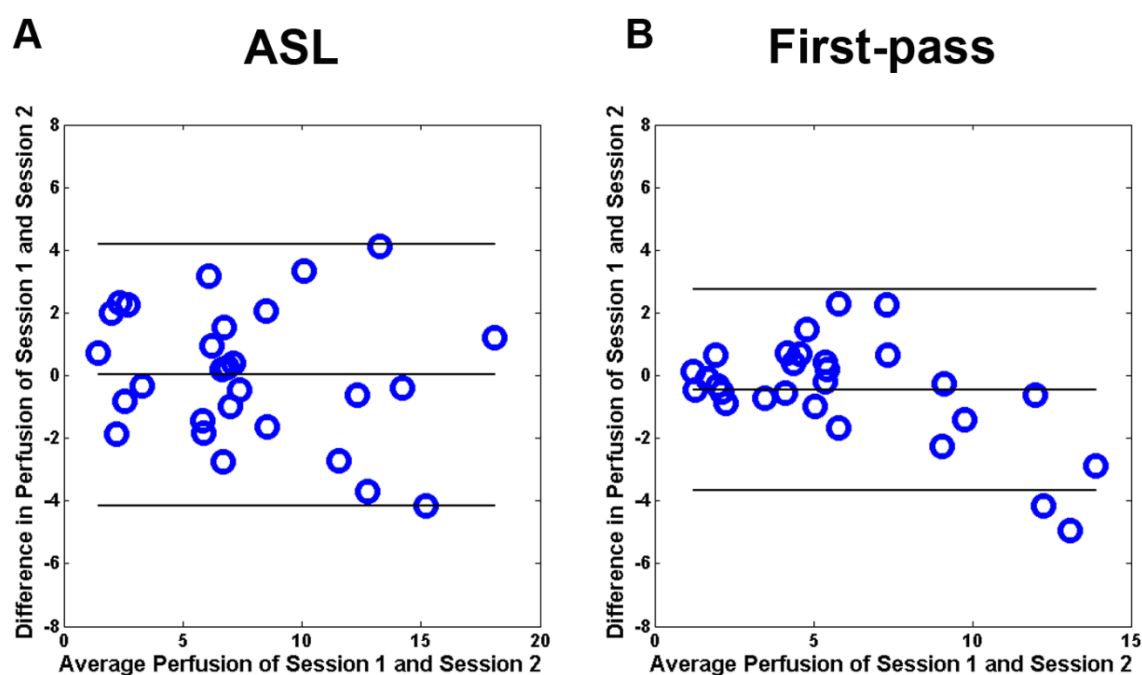
Figure 3.6: Repeatability results for ASL and first-pass MRI in mice. Bland-Altman plots showing the repeatability of perfusion measurements using the two perfusion imaging techniques, CSASL with kinetic ASL model (A) and CS-accelerated first-pass MRI method (B).

Table 3.2: Repeatability and between-session coefficient of variability for both the techniques

		Kinetic ASL Model	First-pass MRI
RC (%)	**Rest**	62	36
	Stress	41	31
	Infarct	138	56
	Remote	44	40
CV	**Rest**	18.55 ± 4.57	10.77 ± 2.18
	Stress	12.66 ± 3.34	14.15 ± 3.59
	Infarct	46.28 ± 9.33	17.03 ± 3.44[*]
	Remote	11.32 ± 2.90	14.50 ± 3.70

* $p < 0.05$ vs. First-pass MRI

The between-session coefficient of variability (CV_{bs}) results for ASL and first-pass MRI are summarized in

Table 3.2. The overall CV_{bs} (including the rest, stress, infarct and remote data) was 22 ± 4% for ASL and 14 ± 2% for first-pass. Similar to RC, the infarct zone CV_{bs} was significantly lower with first-pass as compared to ASL (17± 3 % with first pass vs. 46± 9% with ASL, $p<0.05$). CV_{bs} was comparable for the two techniques at rest (11± 2% with first pass vs. 19± 5% with ASL), stress (14± 4% with first pass vs. 13± 3% with ASL) and in the remote zone (15± 4% with first pass vs. 11± 3% with ASL).

3.3.5. Intra-user variability and Inter-user variability

Bland-Altman plots of intra-user variability and inter-user variability illustrate the mean difference in perfusion for a single individual analyzing the same data in two different sessions and two different individuals analyzing the same data, respectively. The intra-user variability Bland-Altman plots for ASL and first-pass MRI are shown in Figure 3.7A and Figure 3.7B, and the inter-user variability Bland-Altman plots are shown in Figure 3.7C and Figure 3.7D. From the Bland-Altman plots, it can be seen that both the intra-user and inter-user variability are consistent under a variety of conditions for ASL, but they increase at higher flows for first-pass MRI.
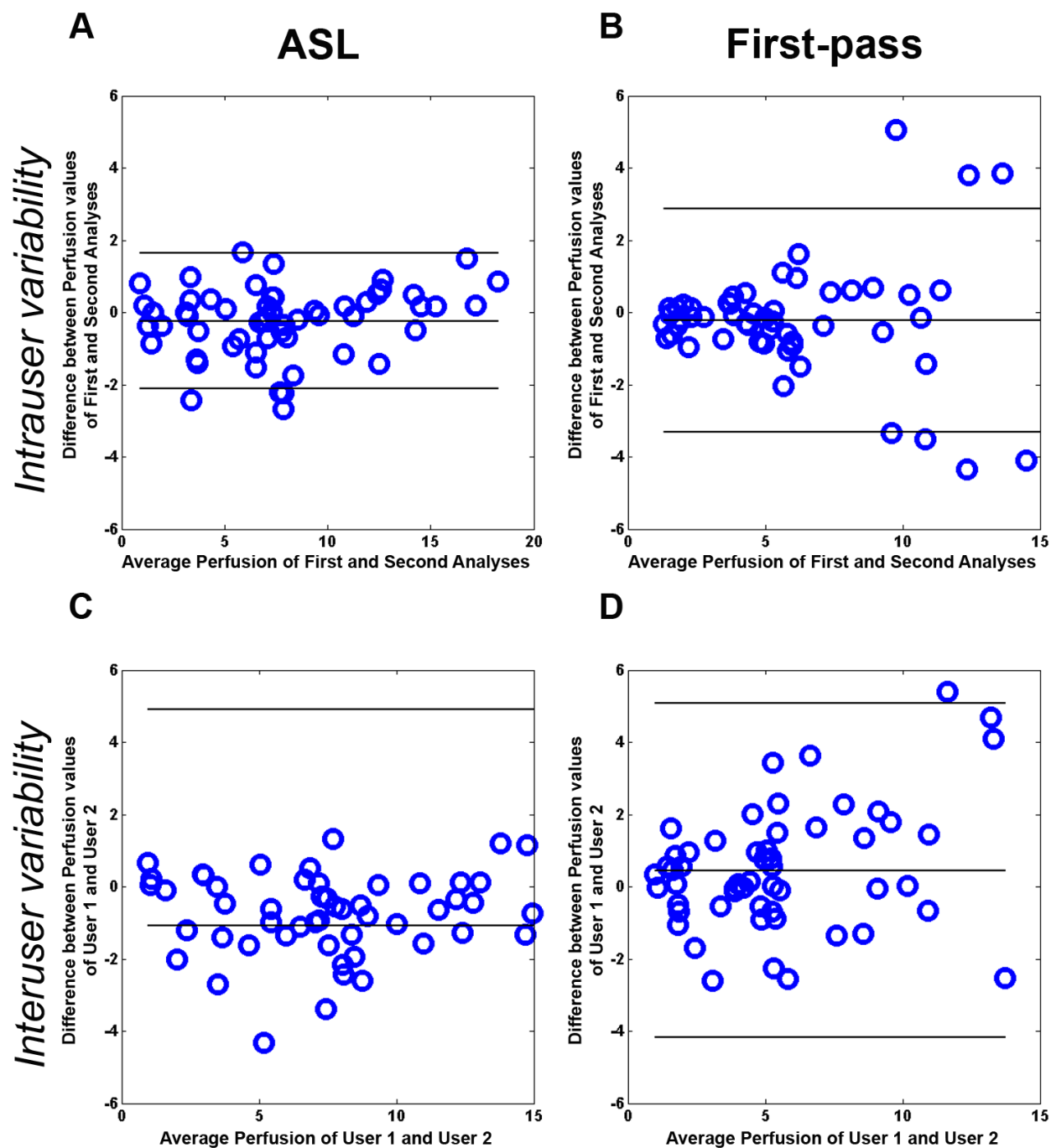
Figure 3.7: Intra-user and inter-user variability for ASL and first-pass MRI in mice. Intra-user variability (A-B) and inter-user variability (C-D) of the two perfusion imaging techniques, CSASL with kinetic ASL model (A,C) and first-pass MRI (B,D).

The $CV_{\text{intra-user}}$ and $CV_{\text{inter-user}}$ for both techniques for rest, stress and infarct studies are summarized in Table 3.3. The overall $CV_{\text{intra-user}}$ (including the rest, stress, infarct and remote studies) was 10 ± 2% for ASL and 11± 1% for first-pass MRI. The $CV_{\text{intra-user}}$ was comparable between the two techniques for the rest and remote zone perfusion studies. The stress perfusion $CV_{\text{intra-user}}$ was significantly lower for ASL compared to first pass (3 ± 1% vs. 14 ± 3%, p<0.05). The infarct zone $CV_{\text{intra-user}}$ trended lower with first-pass MRI as compared to ASL (12 ± 3% vs. 21± 5%).

The overall $CV_{\text{inter-user}}$ (including the rest, stress, infarct and remote data) was 13.99 ± 2.44% for ASL and 20.50 ± 2.40% for first-pass MRI. The $CV_{\text{inter-user}}$ was significantly higher for first-pass MRI compared to ASL at stress (17.16 ± 4.21 vs. 3.69 ± 0.75, p<0.05). The $CV_{\text{inter-user}}$ trended higher for first-pass MRI as compared to ASL for the remaining conditions (13.30 ± 3.22 vs. 8.95 ± 1.51 at rest, 30.88 ± 5.31 vs. 24.55 ± 6.32 in the infarct zone and 20.65 ± 5.31 vs.15.89 ± 5.97 in the remote zone).

3.3.6. Inter-animal variability

Inter-animal variability (CV_a) for rest, stress, infarct zone and remote zone perfusion data for ASL and first-pass MRI are summarized in Table 3.3. CV_a was comparable between ASL and first-pass MRI for the rest, stress and remote zone perfusion studies. There was a trend towards a lower CV_a with first-pass MRI for infarct perfusion studies compared to ASL (26 ± 3% vs. 44 ± 9%).

Table 3.3: Intra-user, inter-user and inter-animal variability for both the techniques

		Kinetic ASL Model	First-pass MRI
Intra-user CV	**Rest**	7.21 ± 1.51	7.56 ± 1.34
	Stress	2.82 ± 0.58[*]	14.33 ± 3.03
	Infarct	21.30 ± 5.25	12.12 ± 2.97
	Remote	8.96 ± 2.25	9.67 ± 1.78
Inter-user CV	**Rest**	8.95 ± 1.51	13.30 ± 3.22
	Stress	3.69 ± 0.75	17.16 ± 4.21
	Infarct	24.55 ± 6.32	28.68 ± 5.21
	Remote	15.89 ± 5.97	16.70 ± 3.83
Inter-animal variability (%)	**Rest**	18.34 ± 0.85	15.55 ± 3.60
	Stress	19.00 ± 2.59	18.31 ± 2.54
	Infarct	44.01 ± 8.58	26.10 ± 2.68
	Remote	20.47 ± 4.08	27.35 ± 3.59

[*]$p < 0.05$ vs. First-pass MRI

3.3.7. Perfusion sensitivity

We define perfusion sensitivity as the change in MRI signal for a given amount of blood flow. To help explain why first-pass MRI generally had better repeatability than ASL, even though image quality was better for ASL, we quantitatively estimated the perfusion sensitivities for these two techniques under the specific experimental conditions of this study. In general terms, because first-pass MRI uses gadolinium as a T1-shortening contrast agent to amplify the effects of perfusion on the signal and ASL does not use this amplification method, it is clear that first-pass MRI will have greater perfusion sensitivity than ASL. To quantify the perfusion sensitivities for each technique, we used the Fermi function model and Bloch equation simulations to estimate signals for first-pass imaging, and we used the gamma-variate based ASL kinetic model to estimate ASL signals. Using these models, we estimated ASL and first-pass MRI signals for blood flows in the range of 1 – 13 ml/g/min (as measured in the mouse heart in this study), using the specific pulse sequence parameters employed in this study, and assuming the gadolinium dose that was used experimentally in this study. Results from these simulations are shown in Figure 3.8, where it is seen that perfusion sensitivity for first-pass MRI is higher than ASL by approximately 75%, 23%, and 27% for blood flows in the low, intermediate, and high regimes, respectively. The greater perfusion sensitivity gained through the use of gadolinium is a major advantage of first-pass MRI compared to ASL, even under conditions specific to mouse heart imaging where the time available for saturation recovery is compressed compared to human imaging.
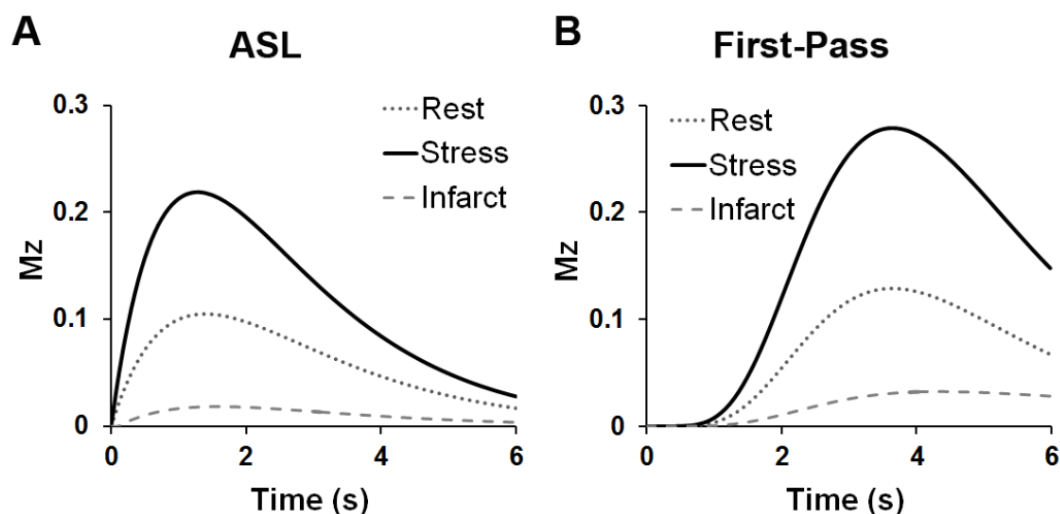
Figure 3.8: Perfusion sensitivity of ASL and First-pass MRI. Normalized signal-time curves simulated using the Fermi function deconvolution method for first-pass and kinetic ASL model for ASL under different conditions (rest, stress, infarct).

3.4. Discussion

The purpose of the present study was to compare ASL and first-pass MRI for the evaluation of myocardial perfusion in preclinical mouse imaging studies. Our comparison included metrics of image quality, repeatability, and variability, and was conducted under varying physiological conditions such as at rest, at stress, and after induction of myocardial infarction.

3.4.1. Image quality

The image quality was better for ASL than first-pass MRI for all conditions (rest, stress and post-MI). The reasons for the superior image quality in ASL images are two-

fold. First, since the acquisition for ASL was segmented, where only one spiral interleaf was acquired per heartbeat, there was very little cardiac motion during the image acquisition (which required less than 3 ms). In contrast, in order to capture the rapid kinetics of the gadolinium bolus, the first-pass acquisition was not segmented, and image quality was degraded by cardiac motion. The time to acquire one AIF image was approximately 25 ms, and the time to acquire one TF image was approximately 36 ms. These times are fairly short compared to a typical RR interval for a mouse, which is approximately 120 ms at rest and 100 ms at stress. However, reducing the scan time further would reduce motion artifact and improve image quality. Second, while ASL was respiratory gated, respiratory gating could not be employed for first-pass imaging in order to capture the rapid kinetics of the gadolinium bolus. While we did use a motion compensated CS reconstruction algorithm, respiratory motion likely caused more artifacts in first-pass imaging than in ASL.

3.4.2. Image acquisition time

Though the image quality of ASL is higher than first-pass, there is a substantial difference in the total acquisition times of the two techniques. While the acquisition time for first-pass imaging was less than a minute, it was approximately 40 minutes for ASL. However, the importance of acquisition time in animal imaging can be very different than human imaging. Whereas there is an emphasis on short scan times in humans due to healthcare economics and patient comfort, for animal imaging accuracy and precision in quantifying physiological parameters may take precedence. The total number of animals needed to test a hypothesis and complete a study may be reduced

by spending more time per animal to improve the accuracy and precision of a measurement. In this way, it may be more economical and ethical to use longer acquisitions. In the present study, acquisition parameters were determined independently for ASL and first-pass MRI in order to achieve good image quality and so that the images would be suited for quantitative analyses. While first-pass MRI will always be faster than ASL in the heart, in the future we will shorten our ASL scans by using a segmented acquisition where more spiral interleaves are acquired in each segment and, possibly, by using higher acceleration rates and lower spatial resolution. A recent study by Troalen *et al.* (101) used a new cine ASL technique in mice which has an 8-minute acquisition time. Another study by Campbell *et al.* (96) used a segmented Look-Locker ASL technique in mice with a reduced acquisition time of 15 min for both slice-selective and non-selective scans.

3.4.3. Perfusion values

The perfusion values measured using first-pass were lower than ASL and the discrepancy between the techniques was observed to increase as flow increased. One potential reason could be the reduction in the extraction fraction of gadolinium from the vascular to the extravascular space with increasing flow (134,135). Perfusion estimation using gadolinium-enhanced MRI depends on the transit of gadolinium to the extravascular space, which can be reduced when coronary flow values are high (134,135).

3.4.4. Repeatability

The between-session repeatability coefficient (RC) indicates the change in perfusion between different treatments or groups that is required to detect differences above systematic errors. With first-pass MRI, the RC is approximately 30-35%. This is consistent with our recent study which showed that stress perfusion was reduced by almost 30% in wild type C57Bl/6 mice fed a high-fat diet as compared to wild type mice on a standard chow diet (103).

The RC for infarcted tissues is much greater using ASL compared to first-pass MRI. This is likely because ASL has lower perfusion sensitivity than first-pass MRI, and the infarct zone has low perfusion. Perfusion sensitivity is the change in MRI signal due to blood flow. Because ASL has low perfusion sensitivity and perfusion is relatively low in the infarcted region, the ASL signal from this area is only slightly greater than the noise. This low signal-to-noise ratio leads to the poor RC.

Campbell *et al.* (96) studied repeatability of segmented ASL in mice at rest. However, their study used a higher isoflurane dose than our study (1.6% vs. 1.2%). Because isoflurane is a potent vasodilator (98), the mean perfusion values (approximately 12 ml/g/min) obtained in their study were comparable to the stress perfusion values obtained in the present study. Our overall RC is similar to their findings (55%). However, the RC specifically for the high flow regime is lower with both our techniques as compared to their reported value (Table 3.4).

Table 3.4: Comparison of repeatability coefficient between our techniques and Campbell *et al.*

RC with our ASL technique	RC with our First-pass technique	RC with Campbell *et al.* technique
41%	31%	55%

3.4.5. Variability

The between-session CV (CV_{bs}) takes into account differences associated with the technique such as repositioning the mouse, reshimming, replacing the ECG leads and i.v. line, and physiological differences in the mouse between the two sessions. The between-session CV indicates the variation to expect when imaging the same set of animals over time. Similar to the results obtained with RC, CV_{bs} was significantly lower with first-pass MRI as compared to ASL in low blood flow conditions (infarct). This is probably due to very low perfusion sensitivity with ASL at low blood flows. Compared to the Campbell study (96), the CV_{bs} values for stress perfusion studies obtained for both techniques in this study are slightly lower than their reported value (13% vs. 17% with ASL and 14% vs. 17% with first-pass MRI). Van Nierop *et. al.* (93) looked at between-session CV with a dual – bolus first-pass technique in mice at rest. Our first-pass CV_{bs} at rest is slightly higher than their reported value (11% vs. 6%).

The $CV_{intra-user}$ measures the variation in measurement when perfusion is estimated from the same dataset by the same user on two different occasions. This

takes into account variation associated with the analysis such as redrawing the ROIs and the various steps in reanalyzing the perfusion datasets. The $CV_{intra-user}$ was significantly lower for ASL as compared to first-pass MRI in the stress perfusion studies. This could be due to the higher image quality of stress perfusion images with ASL. The $CV_{intra-user}$ trended lower with first-pass MRI as compared to ASL for the infarct studies, probably due to higher perfusion sensitivity of first-pass MRI at low blood-flow conditions.

The $CV_{inter-user}$ was lower for ASL than for first-pass MRI under all conditions. This is likely due to the low degree of user interaction in ASL analysis as opposed to first-pass perfusion analysis. There are multiple steps in the first-pass analysis that involve user interaction such as drawing the ROIs for the LV blood pool and myocardium, fitting a gamma-variate function to the AIF data, adjusting the contrast arrival delay time for Fermi function fitting, and determining the end time of first-pass kinetics. In comparison, ASL analysis requires user interaction only when contouring the LV blood pool and LV myocardium.

The inter-animal variability (CV_a) indicates the variation to expect between the animals and this can be useful in deciding the sample sizes while planning an experiment. There was a trend towards lower CV_a with first-pass MRI for infarct perfusion studies as compared to ASL ($26 \pm 3\%$ vs. $44 \pm 9\%$), probably due to the higher perfusion sensitivity of first-pass MRI at low blood flows. CV_a was higher for the infarct and remote zone perfusion studies for both techniques, and this could be due to differences in regional perfusion analysis vs. global perfusion analysis. In the post-MI studies, the signal is averaged from smaller regions and there is increased variation in

the regional signal measurements as compared to the global signal measurements. CV_a obtained in this study was comparable to previously reported values as calculated using the mean and standard deviations (77,93-96,98,100,101,103). Prior studies reported CV_a of 8-27% (77,93-96,98,100,101,103) at rest and stress and our reported values (16-18% with first-pass MRI and 19% with ASL) are within this range. A prior study (94) reported CV_a of 67% in the infarct zone with permanent ligation and our CV_a values are lower than their reported value for both techniques (27% with first-pass MRI and 21% with ASL).

Although the overall repeatability and data variability are comparable between ASL and first-pass MRI, each technique has its own advantages and disadvantages, and depending on the application, one technique may be more suitable than the other. For low blood flow conditions such as infarct imaging, first-pass MRI is more suitable for myocardial perfusion imaging in mice due to better repeatability (lower RC and CV_{bs}) and variability (lower $CV_{intra-user}$ and $CV_{inter-user}$). Additionally, accounting for the issue of overall scan time, first-pass MRI in mice integrates well into a comprehensive MRI protocol due to its short acquisition time. On the other hand, at higher blood flows such as stress perfusion imaging, ASL may be more suitable than first-pass MRI due to its superior image quality and reduced user variability. Furthermore, due to the ability to employ segmented acquisitions with ASL, it is straightforward to achieve higher spatial resolution with ASL compared to first-pass MRI, and this factor is amplified at stress perfusion imaging where heart rates can be as high as 650-700 bpm Additionally, for cases where the stress agent can be injected i.p., the imaging protocol for ASL would be much simpler as it would not require any i.v. lines. In that case, for imaging studies

which require serial perfusion imaging in the same animals over time, ASL could be advantageous since repetitive placement of i.v. lines for first-pass imaging could be difficult. Understanding and balancing these competing factors should prove useful for planning future studies which investigate mechanisms underlying and therapies for perfusion abnormalities in various mouse models of cardiovascular diseases.

Chapter 4: Cardiac MR Detects the Progression of Impaired Myocardial Perfusion Reserve and LV hypertrophy in a Mouse Model of Obesity-Related Cardiomyopathy

4.1. Introduction

Obesity has become increasing prevalent in western society and is associated with increased risk of heart failure (17). The Framingham study showed that the risk of heart failure increased by 5% in men and 7% in women per unit increase in body mass index after adjustment for other risk factors (17). Recently it has been shown that impaired myocardial perfusion reserve is prognostic of adverse cardiovascular outcomes (24). Furthermore, a recent study by Schindler *et al.* (8) showed that increased body weight is independently associated with impaired myocardial perfusion reserve (MPR), even in the absence of obstructive coronary artery disease (CAD). MPR is the amount by which myocardial blood flow increases during stress or maximal coronary vasodilation. Since the coronary arterioles primarily determine coronary vascular resistance, in the absence of obstructive CAD, MPR assesses the function of the small blood vessels (coronary vascular function) and it is a sensitive indicator of the capacity of the coronary circulation to supply oxygen to the myocardium.

Mouse models have been increasingly utilized in cardiovascular research to study underlying mechanisms and to investigate the effects of novel therapies. A recent study characterized the long term effects of high fat diet on the cardiovascular system (107). They showed that mice fed a high-fat diet (HFD) for 8-16 months develop obesity, hyperglycemia, hyperinsulinemia, insulin resistance, cardiomyocyte hypertrophy and other cardiac metabolic compensations (107). Furthermore, using isolated thoracic aorta, they also showed that the HFD mice have impaired vascular reactivity. A more recent study used MRI to show that HFD mice develop cardiac dysfunction after 20 weeks of diet (136). In addition, we recently used first-pass contrast enhanced MRI in

mice and demonstrated that HFD mice have impaired MPR after 24 weeks of diet (103). However, no study so far has characterized the time course of myocardial perfusion in diet-induced obesity in mice.

Myocardial perfusion imaging is a well-established tool to non-invasively assess blood flow to the heart. Quantitative myocardial perfusion imaging in knockout or transgenic mouse models can be used to probe molecular mechanisms underlying impaired MPR in obesity related cardiomyopathy. Since perfusion MRI is non-invasive and non-terminal, quantitative myocardial perfusion MRI can be used to serially study perfusion and this is especially useful in investigating molecular mechanisms in a rodent model. In this study, we used *in vivo* cardiac MRI in a mouse model of diet-induced obesity to establish the time course of impaired MPR and LV hypertrophy and we further used *ex vivo* histological and vascular reactivity studies to elucidate factors underlying the MRI results.

4.2. Methods

4.2.1. Experimental Design

Two groups of mice were studied: wild-type C57Bl/6 mice fed a high fat diet (n = 9) (60% calories from fat, Diet # 12492, Research Diets Inc., New Brunswick, NJ) and age-matched wild-type C57Bl/6 mice fed a low fat diet (n = 9) (10% calories from fat, Diet # D12450J, Research Diets Inc., New Brunswick, NJ). Male mice were selected for

this study as prior studies have shown that female C57Bl/6 mice are protected against high-fat diet induced glucose intolerance (137) and development of obesity related cardiac dysfunction (138). The experimental timeline for this study is shown in Figure 4.1. The mice were started on their respective diets at 6 weeks of age. The mice were studied at 6, 12, 18 and 24 weeks after the start of diet. The MRI protocol at all these time-points included: perfusion imaging at rest and with vasodilator Regadenoson using a dual-contrast first-pass sequence, cine DENSE imaging to measure myocardial strain, cine black-blood MRI to measure end-diastolic volume (EDV), end-systolic volume (ESV), ejection fraction (EF), LV mass, LV wall thickness at end-diastole (LVEDWT) and LV wall thickness at end-systole (LVESWT). Glucose tolerance tests were performed at 6, 12, 18 and 24 weeks after the start of diet. Systolic blood pressure was measured in conscious mice towards the end of the study using a non-invasive tail cuff plethysmography system (Model BP 2000, Visitech Systems, Apex, NC). Mice were euthanized at the end of the study to measure coronary arteriole vascular reactivity *ex vivo*, aorta plaque and for histology.
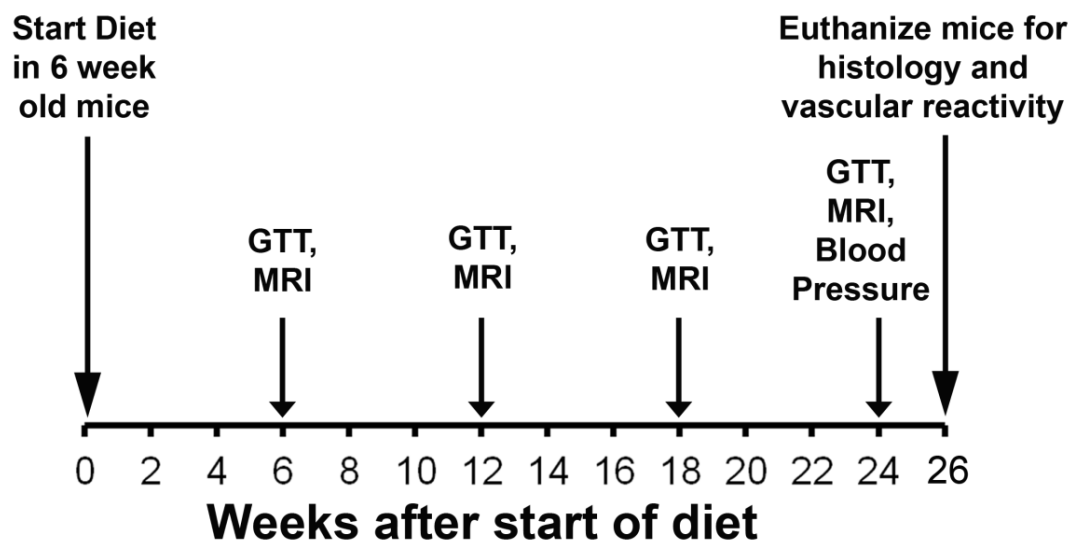
Figure 4.1: Timeline of the experimental design. 6 week old C57Bl/6 mice were fed a high-fat diet (60% calories from fat) or a low-fat diet (10% calories from fat). Glucose tolerance tests and MR imaging was performed at 6, 12, 18 and 24 weeks after start of diet. Blood pressure was measured non-invasively at 25 weeks after diet. At the end of the study mice were euthanized for histology and vascular reactivity studies.

4.2.2. Animal Handling

All animal studies were performed under protocols that comply with the Guide for the Care and Use of Laboratory Animals (NIH publication no. 85-23, Revised 1996) and were approved by the Animal Care and Use Committee at our institution. An indwelling tail vein catheter was established to deliver Gd-DTPA (Magnevist, 0.1 mM/kg body weight) and Regadenoson. Mice were positioned supine in the magnet and body temperature was maintained at 36 ± 0.5 0C using thermostated water. Anesthesia was maintained using 1.1-1.25 % isoflurane in O2 inhaled through a nose cone during

imaging. The ECG, body temperature and respiration were monitored during imaging using an MR-compatible system (SA Instruments, Stony Brook, New York). The body weights were recorded for all the animals before starting the diets and during each imaging study.

4.2.3. Glucose Tolerance Test

For the glucose-tolerance test (GTT) (112), mice were injected intraperitoneally with 1 g/kg glucose in milli-Q water after overnight fasting (15-16 hours). A tail vein blood sample was taken before injection of glucose (to measure the fasting blood glucose) and at 10, 30, 60 and 90 min post-injection of the glucose solution for determination of blood glucose. Blood glucose concentrations were measured using OneTouch Ultra glucometer (LifeScan, Milpitas, CA). The blood glucose values were then plotted versus time and the area under the curve (AUC) was calculated to evaluate glucose tolerance.

4.2.4. MRI Hardware

MRI was performed on a 7T Clinscan system (Bruker, Ettlingen, Germany) equipped with actively shielded gradients with a full strength of 650 mT/m and a slew rate of 6666 mT/m/ms. Additional equipment included a 30 mm diameter birdcage RF coil and an MR-compatible physiological monitoring and gating system for mice (SA Instruments, Inc., Stony Brook, NY).

4.2.5. MRI

In all mice, localizer imaging was performed to select a mid-ventricular short-axis slice. Rest perfusion was then measured using a CS-accelerated dual-contrast first-pass sequence (103). Using this sequence, two slices were acquired: one for the arterial input function (AIF) and the other for the tissue function (TF). The imaging parameters included: echo time/repetition time (TE/TR) = 1.2/2.1 ms, field of view (FOV) = 25.6 x 18 mm^2, phase FOV= 72%, percent sampling = 80%, image resolution = 200 μm^2, matrix = 128 x 74, excitation flip angle = 15^0, slice thickness = 1 mm, AIF saturation delay = 15 ms, TF saturation delay = 57 ms, acceleration rate = 6 for AIF and 4 for TF, AIF acquisition time = 25ms/image and TF acquisition time = 36 ms/image, AIF phase encode lines = 12 and TF phase encode lines = 17. Ten seconds after the start of the acquisition, Gd-DTPA (0.1 mmol/kg body weight) was injected i.v., while imaging continued to capture the first-pass kinetics. Thereafter, baseline LV structure and function was assessed using a black-blood cine MRI sequence as described previously (70). Six to eight short-axis slices were acquired covering the entire LV from base to apex. Some of the imaging parameters included: TE/TR = 1.9/4.4 ms, slice thickness = 1 mm, image resolution = 200 μm^2 and number of averages = 2-4. Myocardial strain was then measured in a mid-ventricular slice using the cine DENSE sequence (84). The imaging parameters included: field of view = 25.6 - 30 mm, matrix = 128x128, slice thickness = 1 mm, repetition time = 7.1 ms, echo time = 0.67 ms, number of averages = 4-6, number of spiral interleaves = 27, flip angle = 17^0 and displacement encoding frequency = 1.1 cycles/mm. The total scan time for a single 2D slice was 10-15 minutes. For the cine DENSE acquisition, fat-saturation was applied when necessary to null the

signal from fat in order to improve the image quality. Thereafter, Regadenoson (0.1 μg/g body weight) was injected i.v. and 10 minutes later, stress first-pass perfusion imaging was performed in a mid-ventricular slice while injecting Gd-DTPA. The imaging protocol was the same as the rest perfusion imaging.

4.2.6. Vascular Reactivity studies

At the end of the study, a subgroup of HFD (n = 3) and control mice (n =2) were euthanized and coronary arteries from the second arborized branches off the left coronary artery were isolated (lumen diameter 90.9 μm +/ -9.5 μm). The arteries were freed of the surrounding cardiac myocytes and were placed in an arteriograph (Danish MyoTechnology, DMT, Ann Harbor, MI), where they were cannulated at both ends and pressurized to 40 mm Hg as previously described (139-141). Cumulative dose-responses to adenosine and acetylcholine and a step-wise pressure increase for assessment of passive tone were measured as previously described (139-141).

4.2.7. Histology

At the end of the study, a subgroup of mice was euthanized for histology (n = 5, each group). The hearts were harvested and the mid-ventricular short-axis sections (3 mm thick) were fixed in 4% paraformaldehyde for 4 hours and then embedded in paraffin. Paraffin embedded sections (5 μm thick) were then stained with H&E to look at morphology of the cardiomyocytes, anti-CD31 antibody (Santa Cruz Biotechnology) to stain for capillaries, Masson's Trichrome to stain for collagen and Mac-2 antibody to stain for macrophages. The stained sections were visualized under brightfield using

Olympus BX51. For measurement of aortic plaque, ascending aortas were excised and stained with Sudan IV.

For histology, image analysis was performed in ImageJv1.49g (NIH). In order to quantify capillary density, 6 random non-overlapping sections were imaged at 40x magnification and capillaries and cardiomyocytes were counted using the 'analyze particles' function in ImageJ. To quantify interstitial fibrosis, 15 random non-overlapping sections (excluding the blood vessels) were imaged at 40x. Thereafter, a thresholding method was used to quantify the area occupied by collagen (which was stained blue in the images). Using the 15 sections, the total collagen area was normalized by the total area occupied by cardiomyocytes and connective tissue and expressed as a percentage. To quantify perivascular fibrosis, two blood vessels were imaged per specimen at 40x and the average perivascular collagen area normalized to the vessel luminal area was expressed. The aortic plaque area, quantified using ImageJ was expressed as a percentage of the aortic vessel area.

4.2.8. Data Analysis

For perfusion images, image analysis was performed in MATLAB (Mathworks, Natick, MA). Undersampled first-pass perfusion images were reconstructed using a motion-compensated compressed-sensing (CS) technique called BLOSM (109). All perfusion analysis was based on Fermi function deconvolution (41), implemented in MATLAB, as described before (103). Briefly, the signal intensity vs. time curves was obtained by placing a region of interest (ROI) in the LV blood pool for the AIF and in the myocardium for the TF. These signal intensities were normalized by the signal

intensities of the proton density images and thereafter converted into T1 values using the methods described by Cernicanu and Axel (38). The pre-contrast T1 was fixed at 1.55 s for blood and 1.45 s for myocardium (103). The black-blood cine images were imported to a workstation and analyzed using Segment (Medviso, AB). Using this software, the end-diastolic (ED) and end-systolic (ES) frames were identified and thereafter, the endocardial and epicardial contours were drawn on these frames for all the slices. Using the software, the EDV, ESV, EF, LV mass, LVEDWT and LVESWT were calculated. The cine-DENSE images were analyzed using the DENSE analysis tool, which is a semi-automatic technique (88) built in MATLAB. Using these images, global peak circumferential strain (E_{cc}) was calculated.

4.2.9. Statistical Analysis

All statistical analyses were performed using SigmaPlot (Systat Software Inc., Point Richmond, CA). Differences in body weight, EDV, ESV, EF, LV mass, LVEDWT, LVESWT, rest perfusion, stress perfusion and E_{cc} were analyzed using two-way repeated measures analysis of variance (ANOVA). All values in text, tables and graphs are presented as mean ± standard deviation.

4.3. Results

4.3.1. Body Mass and Glucose Tolerance Test

Body weight was significantly higher in mice fed high-fat diet after 6 weeks of diet (Figure 4.2, p<0.05 vs. age-matched Control). The HFD mice were mildly hyperglycemic at 12 and 18 weeks of diet as measured using fasting blood glucose (Figure 4.3A, p <0.05 vs. age-matched Control). Figure 4.3B shows glucose tolerance curves of the HFD and control mice after 12 weeks of diet and Figure 4.3C shows the area under the curve for the glucose tolerance test at different time-points after diet. The HFD mice were glucose intolerant as compared to the control mice at 12 weeks after diet (Figure 4.3B-C).
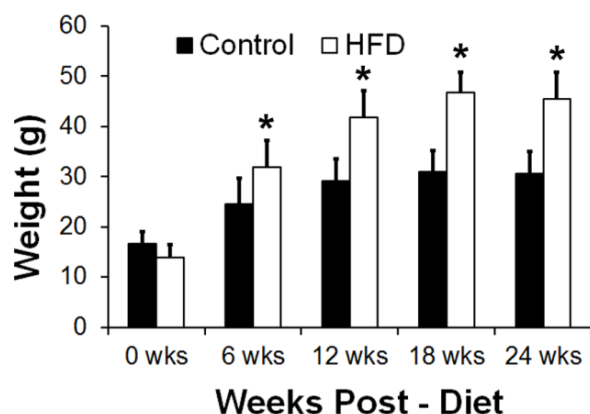
Figure 4.2: Body weight measurements in Control and HFD mice. The figure shows body weight measurements in mice fed high-fat diet (HFD) and low-fat diet (Control) at the start of diet and 6, 12, 18 and 24 weeks after diet. Body weight was increased in the HFD mice after 6 weeks of diet and it progressively increased till the end of the study (*p < 0.05 vs. age-matched Control).
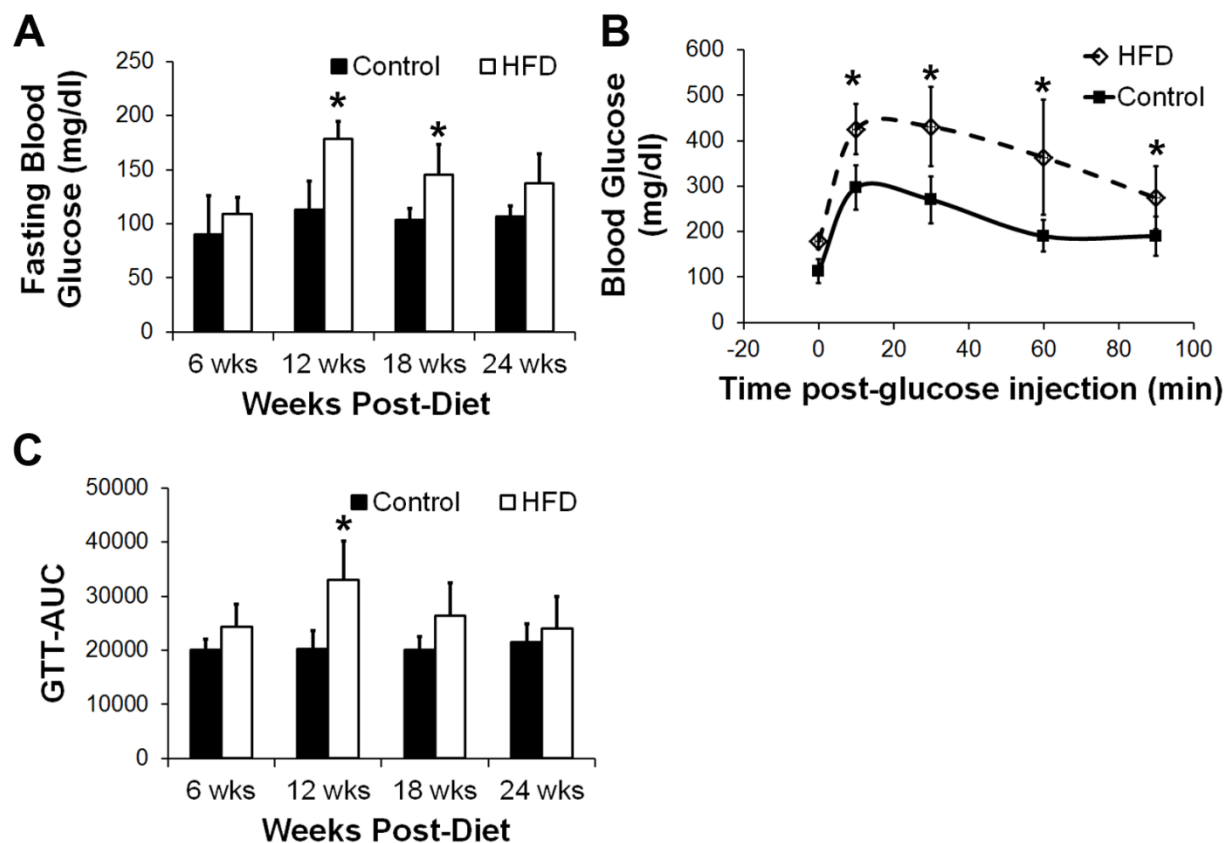
Figure 4.3: Glucose measurements in Control and HFD mice. **(A):** Fasting blood glucose measurements in Control and HFD mice at 6, 12, 18 and 24 weeks post-diet. Fasting blood glucose was higher in the HFD mice (*$p < 0.05$ vs. age-matched control). **(B):** Glucose tolerance curves in the Control and HFD mice at 12 weeks post-diet showing that the HFD mice were glucose-intolerant (*$p < 0.05$ vs. Control at the same time-point). **(C):** The area under the curve (AUC) of the glucose tolerance test for Control and HFD mice at 6, 12, 18 and 24 weeks post-diet (*$p < 0.05$ vs. age-matched control).

4.3.2. MRI

4.3.2.1. Perfusion

Figure 4.4 (A-D) shows example first-pass perfusion images obtained from a mouse heart. Figure 4.5 A-B shows rest and stress perfusion measurements in both the groups of mice at 6, 12, 18 and 24 weeks after the start of diet. There were no differences in the rest perfusion measurements between the two groups of mice (Figure 4.5A). However stress perfusion in the HFD mice was reduced as compared to control mice after 18 weeks of diet (Figure 4.5B, $p<0.05$ vs. age-matched Control). Hence MPR which is defined as stress perfusion normalized by rest perfusion was reduced in the HFD mice as compared to control mice after 18 weeks of diet (Figure 4.5C, $p<0.05$ vs. age-matched Control).
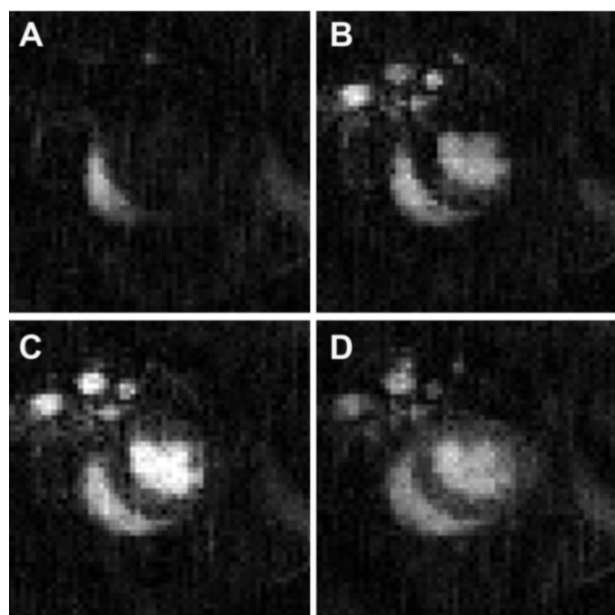
Figure 4.4: First-pass perfusion MRI of the mouse heart. Example first-pass perfusion images obtained from a mouse at rest.
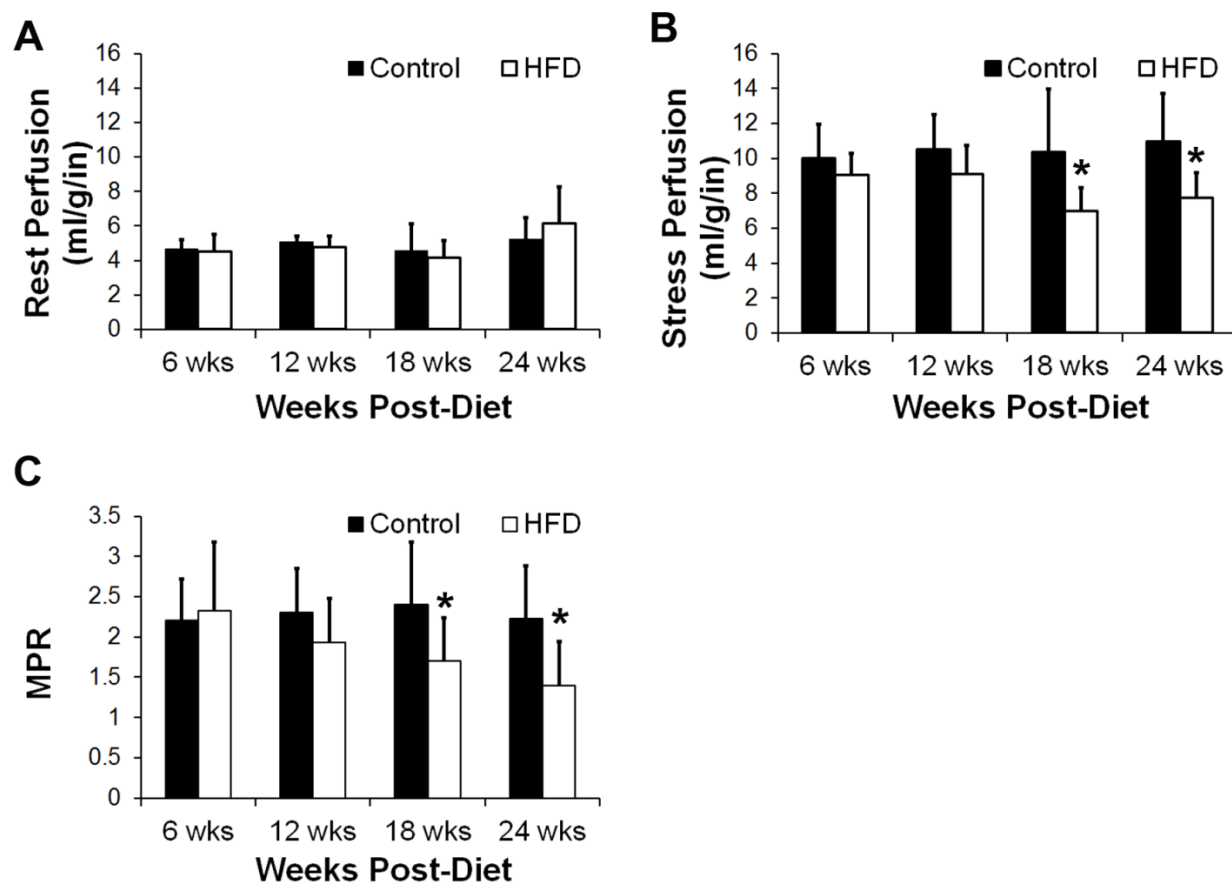
Figure 4.5: MBF and MPR measurements in Control and HFD mice. **(A):** Rest perfusion measurements in the Control and HFD mice at 6, 12, 18 and 24 weeks after diet. **(B):** Stress perfusion measurements in the Control and HFD mice at 6, 12, 18 and 24 weeks after diet. Stress perfusion was reduced in the HFD mice at 18 and 24 weeks after diet (*$p<0.05$ vs. age-matched control). **(C):** MPR measurements in the Control and HFD mice. MPR was reduced in the HFD mice at 18 and 24 weeks after diet (*$p<0.05$ vs. age-matched control).

4.3.2.2.   LV structure and Function

Figure 4.6 shows example black-blood cine images obtained from a control and a

HFD mouse at end-diastole (ED) and end-systole (ES) after 18 weeks on diet. The

hearts of the HFD mice became hypertrophic after 18 weeks of diet and this can be

appreciated from the images and can also be seen from the LV mass and LVEDWT

measurements in the two groups of mice (Figure 4.7A-B). LV mass was significantly

higher in the HFD mice as compared to the Control mice after 18 weeks of diet (Figure

4.7A, $p < 0.05$ vs. age-matched Control). We detected a step-wise increase in LV mass

in the HFD mice. LV mass increased from 78.6 ± 9.0 g at 6 weeks of diet to 85.5 ± 9.4 g

at 12 weeks of diet ($p < 0.05$ vs. HFD at 6weeks post-diet), which then further increased

to 96.9 ± 12.4 g at 18weeks of diet ($p < 0.05$ vs. HFD at 6 and 12weeks post-diet) and

thereafter to 108.3 ± 5.8 g at 24 weeks of diet ($p < 0.05$ vs. HFD at 6, 12 and 18 weeks

post-diet). We also saw a slight increase in LV mass in the Control group at 24 weeks

after diet ($p < 0.05$ vs. Control at 6 and 12 weeks of diet), probably due to ageing.

LVEDWT and LVESWT were also significantly increased in the HFD mice after 18

weeks of diet (Figure 4.7B-C, $p < 0.05$ vs. age-matched Control, $p < 0.05$ vs. HFD at 6

and 12 weeks post-diet). Table 4.1 summarizes the LV volumes, ejection fraction (EF)

and peak circumferential strain (E_{cc}) results obtained in the two groups of mice at the

various time-points. There were no statistically significant differences in LV EDV, LV

ESV, LV EF and LV E_{cc} measurements between the two groups of mice (Table 4.1).
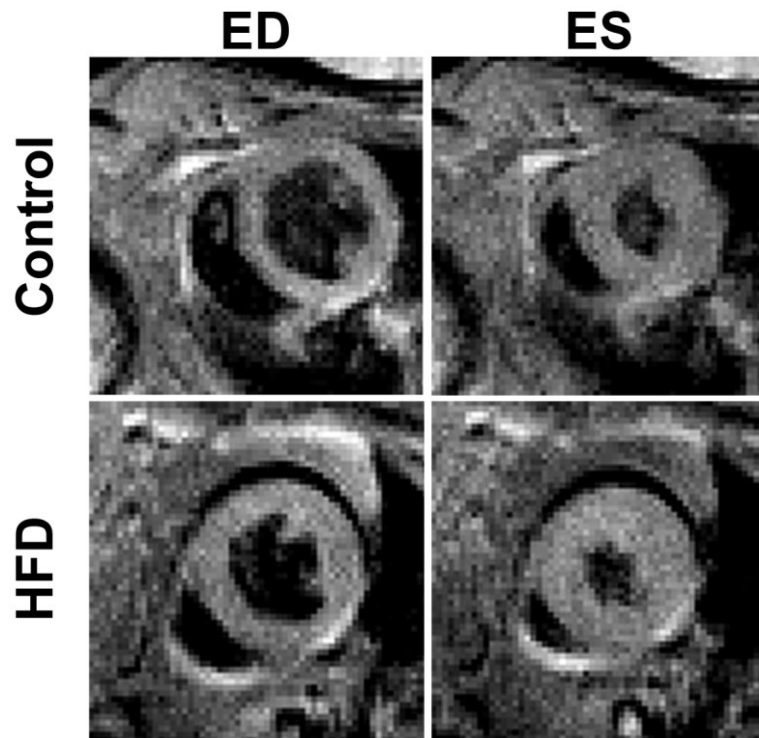
Figure 4.6: Cine images from Control and HFD mice. This figure shows example black-blood cine images in the Control and HFD mice at end-diastole and end-systole after 18 weeks of diet.
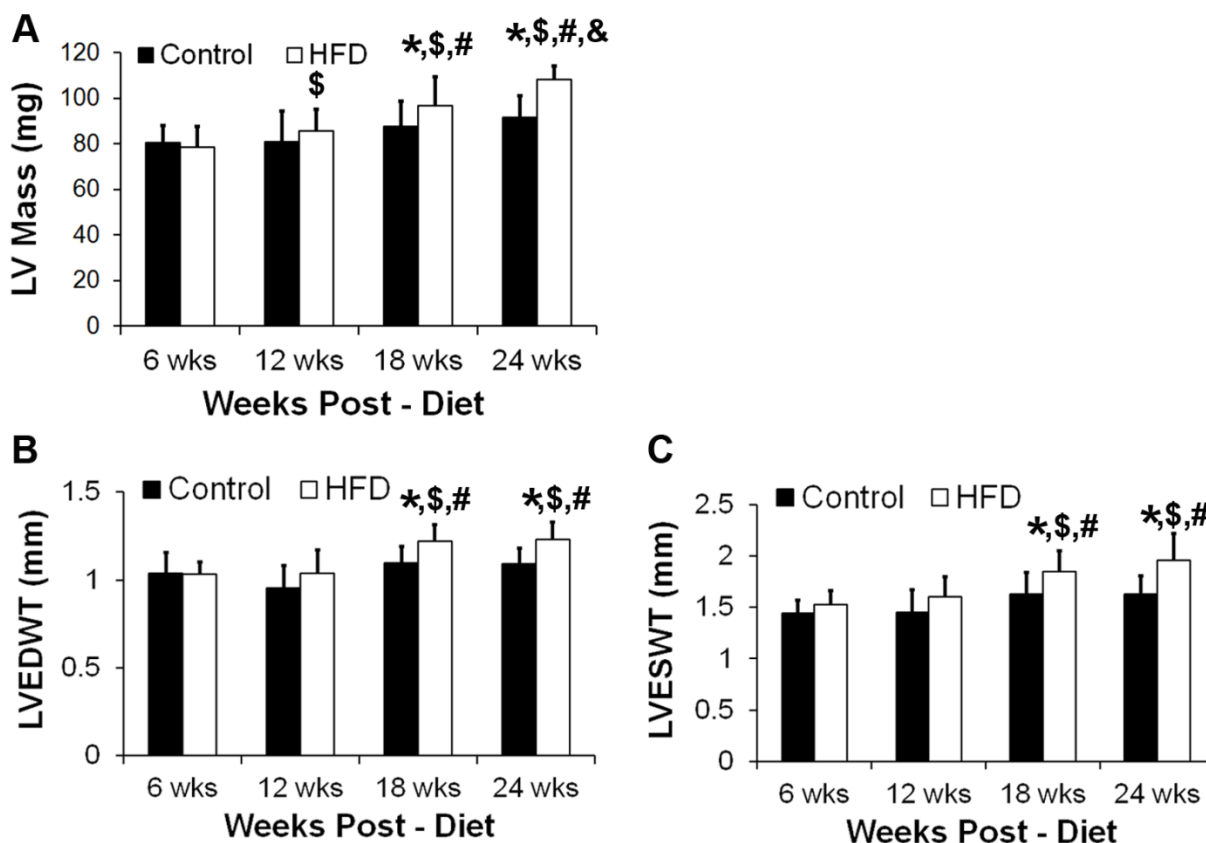
**Figure 4.7:** LV mass and LV wall thickness measurements in Control and HFD mice. **(A):** LV mass measurements in the Control and HFD mice at 6-24 weeks after diet. LV mass was increased in the HFD mice vs. Control mice at 18-24 weeks after diet. **(B):** LV end-diastolic wall thickness (LVEDWT) measurements in the Control and HFD mice at 6-24 weeks after diet. LVEDWT was increased in the HFD mice vs. Control mice at 18-24 weeks after diet. **(C):** LV end-systolic wall thickness (LVESWT) measurements in the Control and HFD mice at 6-24 weeks after diet. LVESWT was increased in the HFD mice vs. Control mice at 18-24 weeks after diet (*$p<0.05$ vs. age-matched control, $p<0.05$ vs. HFD at 6 weeks, #$p<0.05$ vs. HFD at 12 weeks, &$p<0.05$ vs. HFD at 18 weeks).

Table 4.1: MRI parameters of cardiac function

	Time (Weeks after start of diet)							
	6 weeks		**12 weeks**		**18 weeks**		**24 weeks**	
	Control	**HFD**	**Control**	**HFD**	**Control**	**HFD**	**Control**	**HFD**
LVEDV (µL)	43 ± 7	42 ± 7	48 ± 9	47 ± 10	44 ± 7	40 ± 7	40 ± 6	43 ± 5
LVESV (µL)	17 ± 4	14 ± 4	17 ± 6	17 ± 6	16 ± 6	12 ± 5	13 ± 4	11 ± 5
LVEF (%)	61 ± 8	66 ± 8	64 ± 12	65 ± 8	64 ± 9	69 ± 12	67 ± 8	74 ± 11
E_{cc} (%)	-0.14 ± 0.02	-0.13 ± 0.02	-0.13 ± 0.02	-0.12 ± 0.01	-0.12 ± 0.03	-0.11 ± 0.02	-0.12 ± 0.01	-0.14 ± 0.02
Heart Rate (bpm)	530 ± 63	538 ± 88	478 ± 39	485 ± 69	450 ± 84	512 ± 62	507 ± 47	549 ± 59

LVEDV: Left-ventricular end-diastolic volume, LVESV: Left-ventricular end-systolic volume, LVEF: Left-ventricular ejection fraction, E_{cc}: Circumferential strain

4.3.3. Blood Pressure and Heart Rate

There were no statistically significant differences in the systolic and diastolic blood pressure measurements between the two groups of mice after 25 weeks of diet (Figure 4.8). There were also no heart rate differences between the two groups of mice for the entire time course of study (Table 4.1).
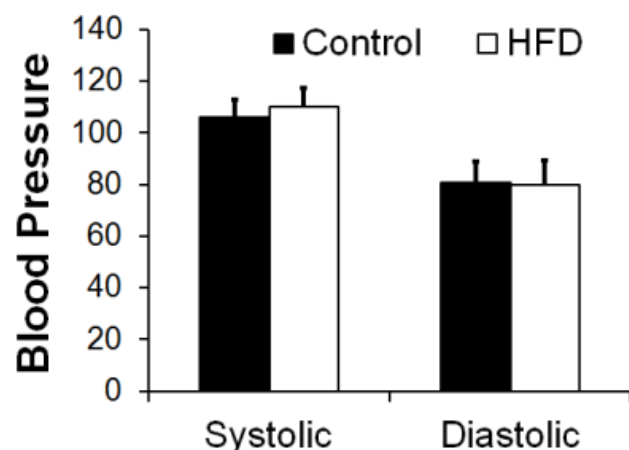
Figure 4.8: Blood pressure measurements in Control and HFD mice. There are no significant differences in systolic and diastolic blood pressure measurements between Control and HFD mice after 25 weeks after diet.

4.3.4. Vascular Reactivity

In order to further elucidate our perfusion imaging results, we performed vascular reactivity studies using isolated coronary arterioles. Cumulative dose-response curves to adenosine demonstrated a significantly decreased ability of the arteries to dilate when the mice were fed a high-fat diet for 26 weeks (Figure 4.9A, $p<0.05$ vs. Control). Since loss of endothelial dilators is a hallmark of high-fat diets, we also tested vascular reactivity to acetylcholine, an endothelial specific dilator. Similar to adenosine, the ability of HFD mice to dilate coronary arterioles was significantly inhibited in response to acetylcholine (Figure 4.9B, $p<0.05$ vs. Control). Lastly, we tested whether a change in matrix composition may also be altered in the coronary arterioles by measuring the passive tone in increasing pressure steps. In the HFD mice, the passive tone was significantly inhibited as compared to the control mice (Figure 4.9C, $p<0.05$ vs. Control).

These results together with the MR perfusion results demonstrated that the coronary arterioles in the mice fed a high fat diet have a significantly decreased capacity to dilate.
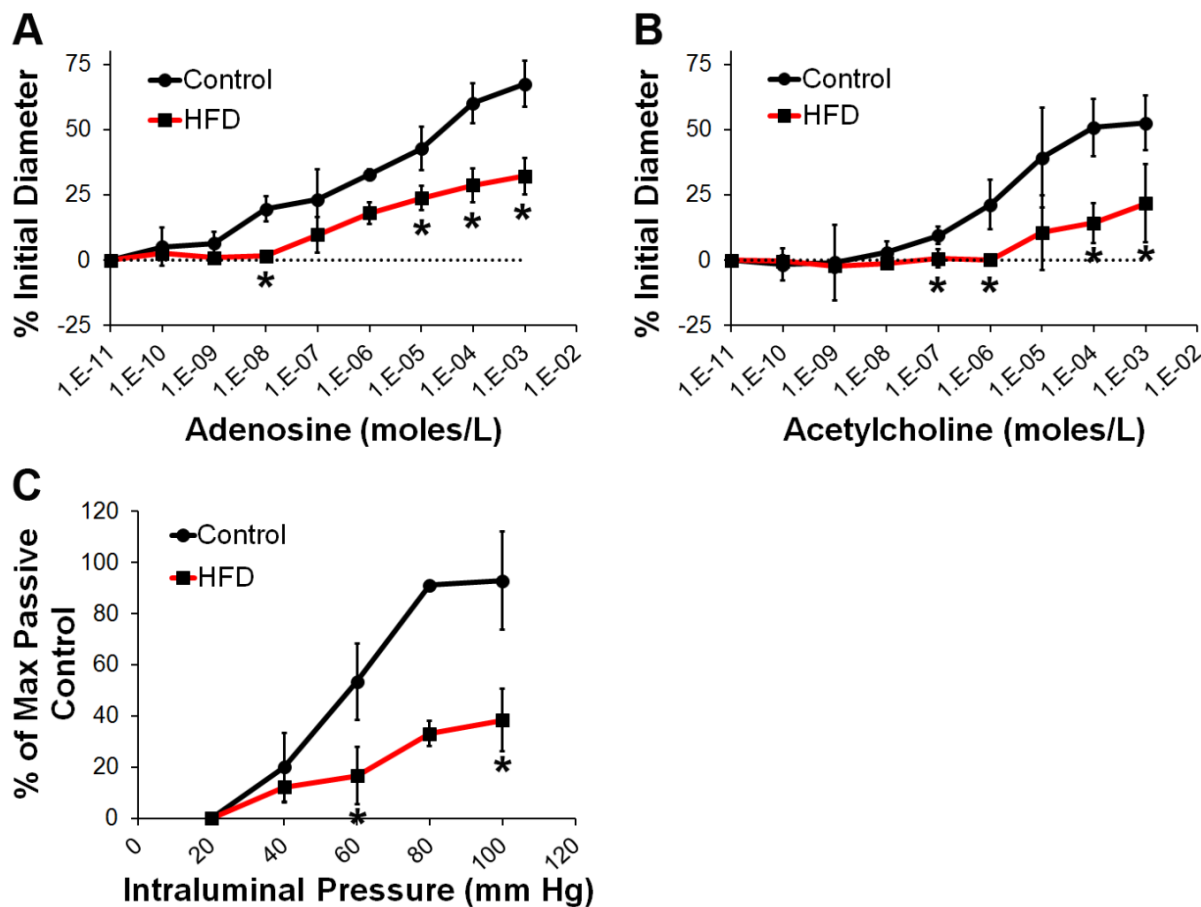
Figure 4.9: Coronary arteriole vascular reactivity in Control and HFD mice. (A): Cumulative dose-response curves to adenosine in Control and HFD mice at 26 weeks after diet. Coronary vascular reactivity to adenosine is reduced in the HFD mice (*p<0.05 vs. Control at same concentration). (B): Cumulative dose-response curves to acetylcholine in Control and HFD mice at 26 weeks after diet. Coronary vascular reactivity to acetylcholine is reduced in the HFD mice (*p<0.05 vs. Control at same concentration). (C): Passive tone in the Control and HFD mice after 26 weeks after diet. Passive tone was inhibited in the HFD mice (*p<0.05 vs. Control at same pressure).

4.3.5. Histology

Figure 4.10 shows example CD31-stained images obtained from a control and HFD mouse heart. There were no significant differences in the number of capillaries per cardiomyocyte between the two groups of mice (Figure 4.10C). Furthermore, there was no aortic atherosclerosis in both control and HFD mice. Aortic plaque was found to be 3.7 ± 1.8 % in the control mice and 3.2 ± 1.4 % in the HFD mice. Figure 4.11 shows Masson's Trichrome stained sections of myocardium obtained from a control mouse (Figure 4.11A) and a HFD mouse (Figure 4.11B). We found increased interstitial fibrosis in HFD mice (Figure 4.11C, $p<0.05$) after 26 weeks of diet as compared to control mice. Figure 4.12 shows Masson's Trichrome stained coronary arteries obtained from a control mouse (Figure 4.12A) and a HFD mouse (Figure 4.12B). We found a trend towards increased perivascular fibrosis in the HFD mice (Figure 4.12C). We also noted increased macrophages in the HFD mice (Figure 4.13).
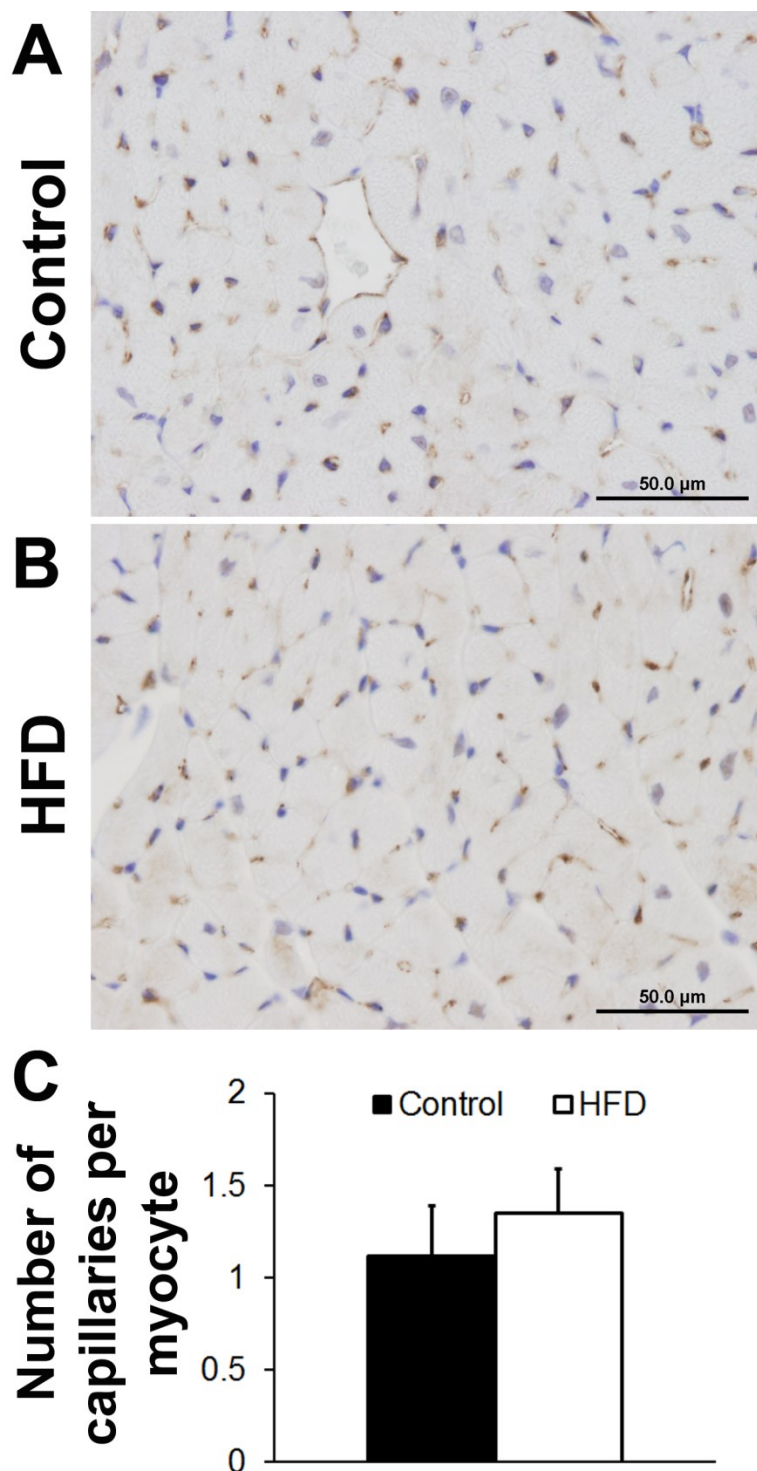
Figure 4.10: Myocardial capillary density in Control and HFD mice. (A): Representative

CD31-stained sections of heart from a Control and (B): a HFD mouse. (C): Number of

capillaries per cardiomyocyte was unchanged by the high-fat diet. Scale bars = 50 μm.
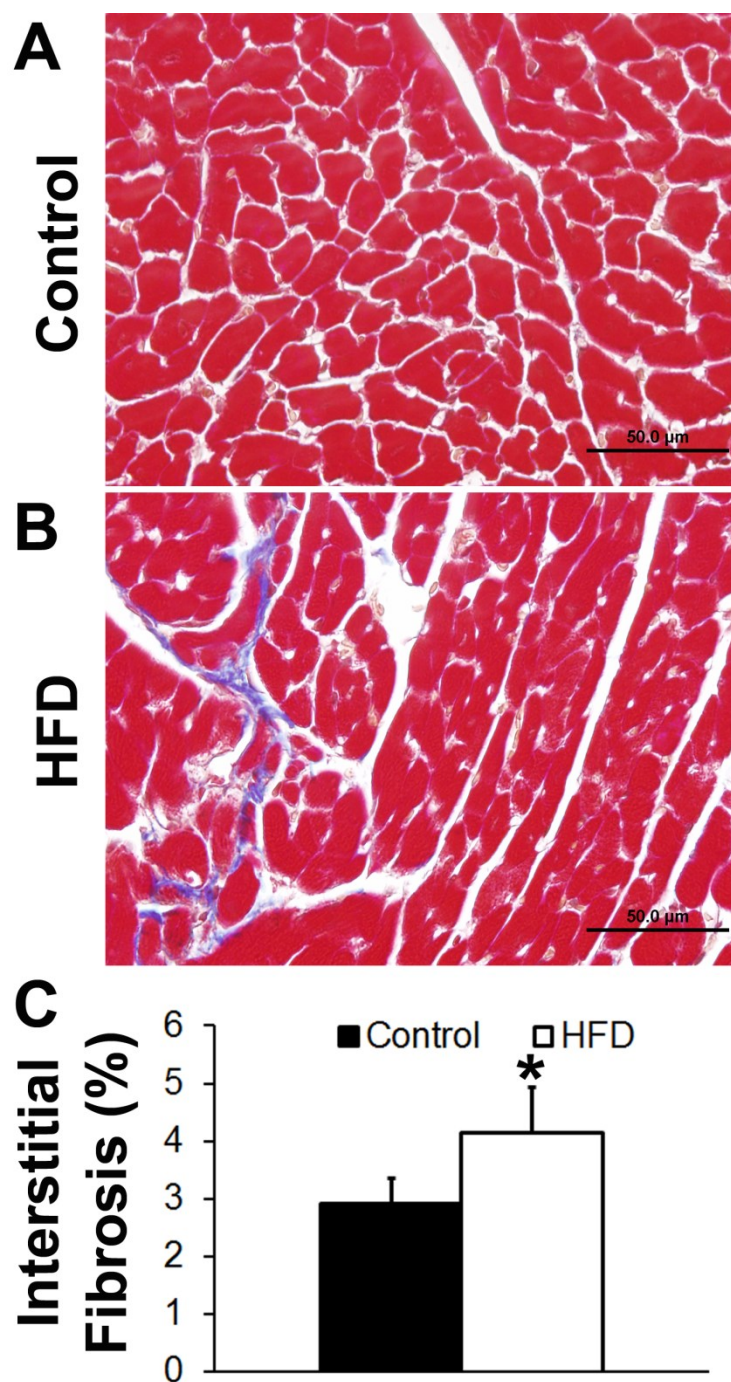
Figure 4.11: Myocardial interstitial fibrosis results in Control and HFD mice. (A): Representative Masson's Trichrome stained sections of heart from a Control and (B): a HFD mouse. (C): Myocardial interstitial fibrosis was significantly higher in HFD mice. Scale bars = 50 μm.
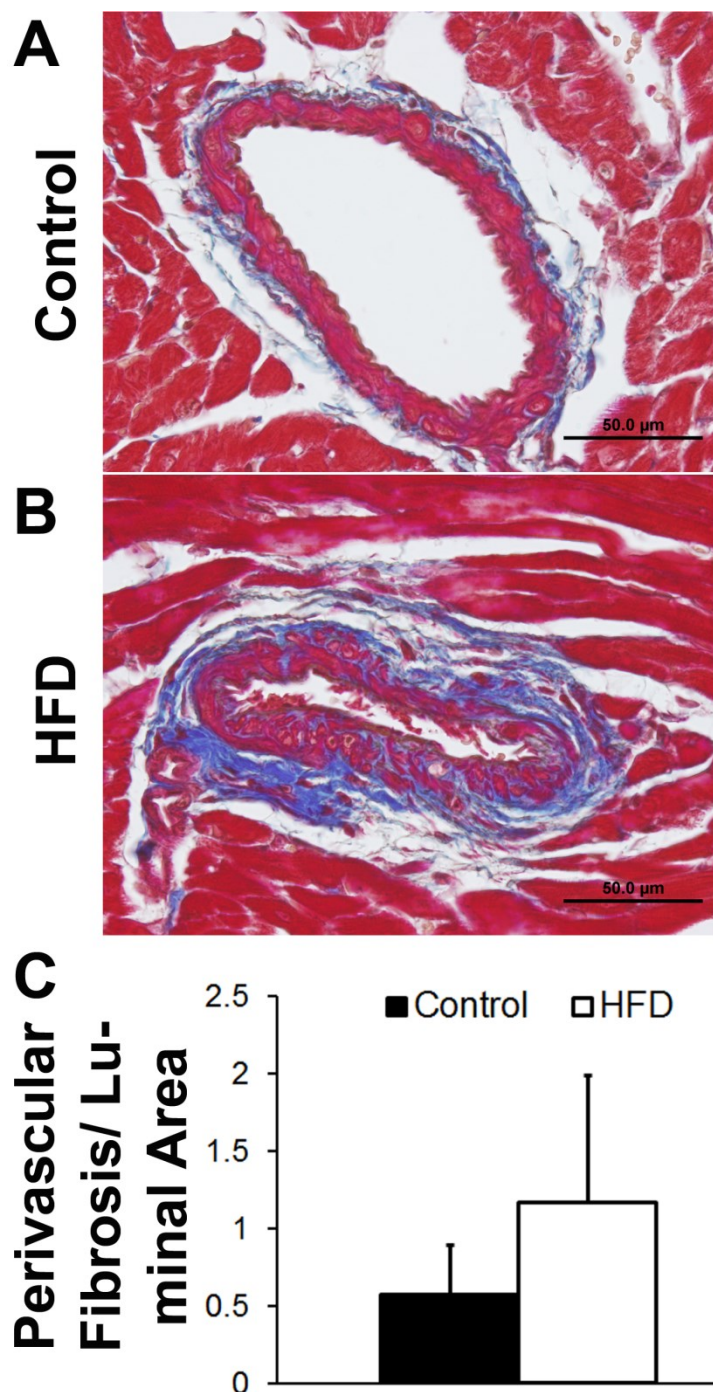
Figure 4.12: Perivascular fibrosis in Control and HFD mice. (A): Representative Masson's Trichrome-stained coronary vessels from sections of heart from a Control mouse and (B): a HFD mouse. (C): There was trend towards increased perivascular fibrosis in HFD mice. Scale bars = 50 µm.
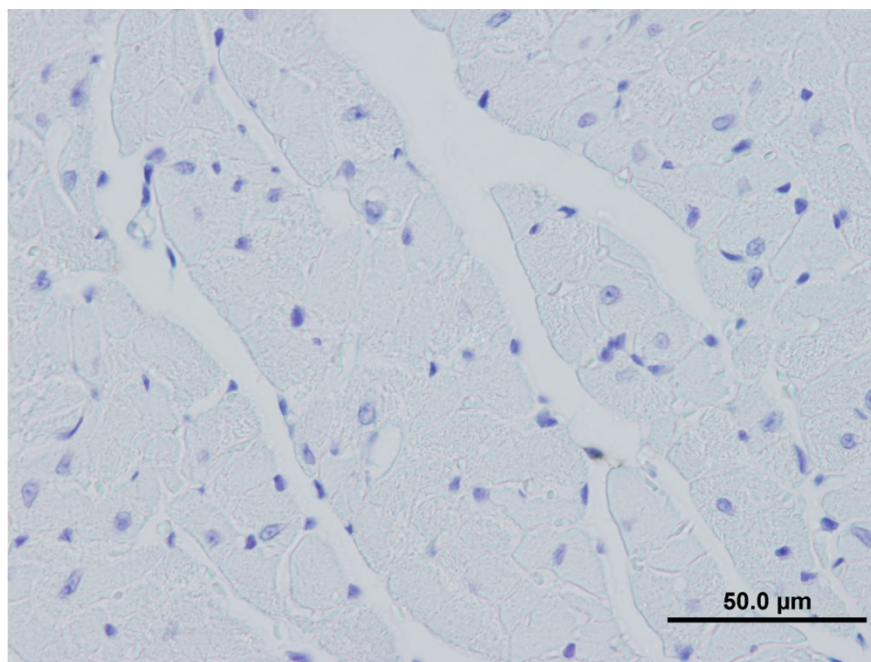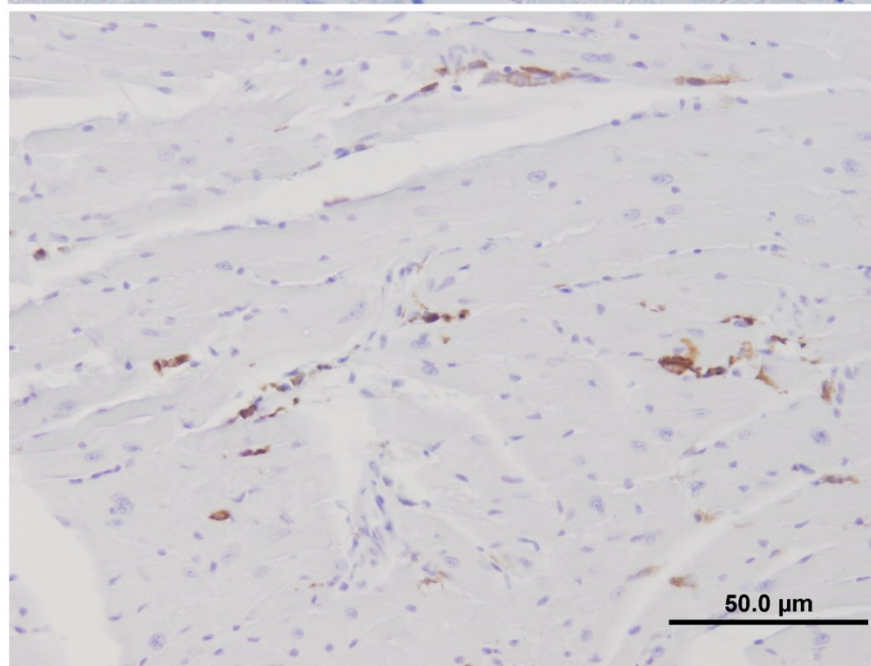
Figure 4.13: Mac2-staining in Control and HFD mice. Representative Mac2-stained sections of the heart obtained from a Control and a HFD mouse. More macrophages were observed in the hearts of HFD mice.

4.4. Discussion

Obesity and increased body weight is associated with increased risk of heart failure (17) and is independently associated with impaired myocardial perfusion reserve (8). In this study, for the first time we have established the time course of reduction in MPR in a mouse model of diet-induced obesity. Using *in vivo* cardiac MRI we showed that 18 weeks of high-fat diet in C57Bl/6 mice resulted in significantly reduced myocardial perfusion reserve without changes in capillary density and without aortic atherosclerosis. The perfusion imaging results were thereafter corroborated using *ex vivo* vascular reactivity studies. We showed that the vasodilatory capacity of the isolated coronary arterioles was impaired in response to adenosine in the HFD mice which directly supports the imaging finding of reduced stress MBF in the HFD mice. Thereafter, we also showed that the HFD mice had reduced response to acetylcholine, an endothelial specific dilator which could signify endothelial dysfunction. Furthermore, we also showed that 18 weeks of HFD in mice resulted in increased LV mass and increased LV wall thickness without changes in LV volumes and peak LV circumferential strain.

Our vascular reactivity results are in agreement with prior studies by Yamamoto *et al.* (142) and Calligaris *et al.* (107), who have also shown significantly impaired vascular endothelium dependent relaxation in response to acetylcholine in mice fed a high-fat diet after 17 weeks and 8-16 months of diet respectively. Furthermore, these results are also in line with prior studies which reported impaired coronary endothelial function in patients with obesity (8,143).

In this study, we have shown that HFD mice develop cardiac hypertrophy (increased LV mass and LV wall thickness) after 18 weeks of feeding. There were no significant differences in systolic and diastolic function (LV volumes, LV peak E_{cc}, systolic strain rate and diastolic strain rate) between the two groups of mice for the time course of the study. Previous studies have used C57Bl/6 mice with different types of high-fat diets to study the effects of obesity, diabetes and metabolic syndrome on cardiac function (107,136,138,142,144-152). Similar to our findings, a recent study by Calligaris *et al.*(107) showed increased LV mass, cardiomyocyte hypertrophy and normal baseline systolic function in HFD mice after 8-16 months of HFD feeding using histology, echocardiography and cardiac catheterization. Using cardiac catheterization, they also showed impaired cardiac function under stress after 8-16 months of HFD. In contrast to our results, another study (144) showed reduced systolic function as measured by echocardiography in HFD mice after 25 weeks. Similar to our results, another recent study (136) showed normal systolic function and increased LV mass in mice fed a high-fat diet where 45% of the calories came from fat after 20 weeks of diet. They also showed 15% impairment in the early diastolic phase of the HFD mice after 20 weeks of diet using high frame-rate cine MRI (50-60 frames per cardiac cycle). Another recent study reported 40% reduction in subepicardial circumferential strain using cine DENSE imaging in the HFD mice after 5 months of diet (117). In our study, we saw a trend towards lower subepicardial strain at 12-18 weeks of diet (data not shown), however this trend disappeared at 24 weeks after diet. One potential reason for this could be the mortality of some of the obese mice between 18-24 weeks of diet.

We noted some variability in the glucose tolerance measurements in mice over time. A prior study showed that C57Bl/6 mice fed a high-fat diet display a heterogeneous metabolic adaptation (153). One potential reason for variability in glucose tolerance measurements in this study could be the combination of heterogeneous adaptation to high-fat diet and mortality of some obese mice over time. Another potential reason could be the repetitive handling of the mice.

The exact mechanism for the dramatic change in vascular reactivity in the coronary arteries is not known. One possibility is a rapid deterioration of the overall endothelium, and endothelial dilatory components in particular, especially changes in eNOS, which has been observed in a plethora of other high-fat models. The lack of dilation in response to both adenosine and acetylcholine, agonists that have well-defined endothelial derived nitric oxide release for smooth muscle dilation, would indicate this is likely the case. Furthermore, we also showed that the passive tone (zero calcium in the buffer) in the isolated coronary arteries was also significantly reduced, indicating likely a dramatic change in extracellular matrix composition, making the arteries more rigid. Correspondingly, using Masson's Trichrome stained sections of the heart and coronary vessels, we also showed significantly higher interstitial fibrosis and a trend towards increased perivascular fibrosis in the HFD mice. Similar to our results, a prior study has also shown that mice fed a high fat diet develop increased perivascular fibrosis (142). This change in extracellular matrix, especially perivascular fibrosis, may result in stiffer vessels, thereby affecting the dilation of these vessels. Regardless of the exact mechanism for the change in vascular reactivity, because the ability of resistance arteries to dilate or constrict governs the degree of blood flow to the capillaries, it is

highly likely that the inability of these coronary arteries to dilate in response to adenosine (or acetylcholine and changes in pressure) is responsible for the significantly inhibited MPR.

Several mechanisms have been implicated in the pathogenesis of obesity related cardiac dysfunction such as insulin resistance, lipotoxicity, inflammation, oxidative stress and renin-angiotensin-aldosterone system (RAAS) activity (154). Accumulation of fat or lipid in cardiomyocytes is known as cardiac steatosis and it is a common finding in obesity (155). Prolonged lipid overload in the heart is known to be toxic to cardiomyoctes through increased oxidative stress (156), fibrosis (157), apoptosis (156,158), increased endoplasmic reticulum (ER) stress (156), ceramide accumulation (156) and mitochondrial dysfunction (156). Furthermore, lipotoxicity is known to stimulate cardiomyocyte hypertrophy (157,159) and increased fibrosis, which in turn leads to cardiac dysfunction (157). Prior studies have also shown increased cardiac inflammation in obesity which then leads to cardiac hypertrophy and dysfunction (160). Recently, there has been a growing interest in the role of adiponectins in obesity related disorders (161). Adiponectin is a hormone secreted by adipose tissue and the plasma concentration of adiponectin is reduced in patients with obesity-related disorders (162). A recent study showed that pressure overload in adiponectin deficient mice resulted in concentric LV hypertrophy and that supplementation of adiponectin attenuated cardiac hypertrophy in response to pressure overload (163). These findings suggest that low levels of adiponectin may contribute to cardiac hypertrophy in obesity related disorders (161). Some or all of the above mentioned mechanisms may be responsible for LV hypertrophy observed in the HFD mice in this study.

4.5. Conclusion

Using cardiac MR, vascular reactivity, and histological studies, we showed that C57Bl/6 mice fed a HFD for 18–24 weeks have LV hypertrophy and reduced vasodilatory capacity at stress with normal capillary density and no aortic plaque. Future studies using cardiac MR and gene-modified mice fed a HFD may shed light on key molecular mechanisms that underlie myocardial ischemia in obesity related cardiomyopathy.

Chapter 5: Conclusions and Future Directions

5.1. Conclusions

5.1.1. Quantitative First-Pass Perfusion MRI in Mice

In the study discussed in chapter 2, we presented a dual-contrast first-pass MRI technique for mice. We used k_y-t undersampling with a dual-contrast saturated recovery gradient echo technique and BLOSM compressed sensing reconstruction to measure perfusion in mice. In this study, we demonstrated that this technique provides the spatial and temporal resolution to perform absolute quantification of MBF in mice at rest and after vasodilation. Furthermore, using this technique we also detected reduced MPR in mice fed a high-fat diet for 24 weeks. Since the image acquisition time is less than a minute, this technique allowed us to quantify MPR in mice in a sufficiently short scan time. Future studies may apply this technique in gene modified mice to study mechanisms underlying obesity and diabetes.

5.1.2. Comparison of ASL and First-pass MRI in Mice

In the study discussed in Chapter 3, we compared the two perfusion imaging techniques, first-pass perfusion MRI and ASL for assessment of MBF in mouse imaging studies. We compared metrics of image quality, repeatability, and variability, for the two techniques under varying physiological conditions such as at rest, at stress, and after induction of myocardial infarction. We demonstrated that image quality was superior with ASL as compared to first-pass MRI. Furthermore, we also demonstrated that although the overall repeatability and variability was similar for both the techniques, each technique has its own advantages and disadvantages and depending on the

specific application, one technique might be better than the other. At low MBF conditions such as infarct imaging, it might be more suitable to use first-pass MRI due to its better repeatability and variability. Furthermore, first-pass MRI would integrate better into a more comprehensive imaging protocol due to its short scan time. However, at high MBF conditions such as at stress, ASL might be more suitable due to its superior image quality and reduced user variability. This study may be useful in planning future studies investigating perfusion abnormalities in cardiovascular diseases.

5.1.3. Time course of Impaired MPR in HFD Mice

In the study described in chapter 4, we described the time course of MPR in a mouse model of diet-induced obesity and we used histological and vascular reactivity studies to further elucidate the underlying factors. We showed that after 18 weeks of high-fat diet, MPR was impaired and LV mass and LV wall thickness was increased as compared to wild type mice fed a low-fat diet. In parallel with the MPR results we also showed that coronary vascular reactivity was reduced in the HFD mice. These findings were observed in the absence of any differences in myocardial capillary density and in the absence of aortic atherosclerosis. Future studies using these techniques in gene-modified mice fed a high-fat diet may shed light on mechanisms underlying obesity related cardiomyopathy and may also be used to test novel therapies for obesity related cardiomyopathy.

5.2. Future Directions

5.2.1. Improvements for First-Pass MRI in Mice

Currently, the image acquisition time for each AIF image is 25 ms and the image acquisition time for each TF image is 36 ms. The R-R interval for mice is about 120 ms at rest and about 100 ms after vasodilation. Image quality of first-pass MRI in mice may be further improved by decreasing the acquisition time for each image. This may be achieved by using other k-space trajectories such as radial and spiral and by exploring higher acceleration rates, possibly by using phased-array coils and by combining parallel imaging with compressed sensing. Decreasing the image acquisition time would reduce the artifacts due to cardiac motion especially after vasodilation. However, with non-cartesian trajectories, off-resonance artifacts may be a problem, especially with obese mice. This may be further optimized by reducing the duration of each spiral or radial spoke.

5.2.2. Improvements for ASL in Mice

The scan time for ASL in mice may be reduced by using a segmented acquisition where 3-4 spiral interleaves are acquired each heartbeat and by exploring higher acceleration rates. Currently, in our study, we have used rate 2 acceleration for ASL imaging. Using an imaging protocol with 3 spiral interleaves per heartbeat with rate 4 acceleration, would bring the total scan time (including both slice-selective and non-selective scans) down to 6-8 min. This would make it feasible to integrate ASL in a more comprehensive MRI protocol.

5.2.3. Assessing Therapies for Obesity-Related Cardiomyopathy

In our study, we demonstrated that HFD mice have increased LV mass and increased LV wall thickness. It has been shown using prior studies that numerous factors may contribute to LV hypertrophy such as lipotoxicity (157), low levels of adiponectin (161) and increased inflammation (160). Thus, future experiments may investigate therapeutic approaches such as the use of lipid lowering drugs, supplementation of adiponectin or the use of anti-inflammatory drugs to prevent and reverse cardiac hypertrophy in HFD mice.

In our study we showed that MPR is impaired in HFD mice after 18 weeks of diet. Additionally, we also demonstrated using vascular reactivity studies that HFD mice have reduced response to acetylcholine, which is an endothelium mediated vasodilator. This could signify endothelial dysfunction. Prior studies have shown that obesity is linked to increased oxidative stress which results in reduced nitric oxide bioavailability and this could eventually lead to endothelial dysfunction (18,164). Thus, therapies to reduce oxidative stress may restore endothelial dysfunction associated with obesity and may also normalize the MPR values in HFD mice. Prior studies have used leptin treatment and inhibitors of NADPH to reduce oxidative stress in obese mice. A recent study also showed that obesity related endothelial dysfunction of the mesenteric arteries can be prevented by deficiency of P-selectin Glycoprotein Ligand-1 (165). Other mechanisms may also be responsible for endothelial dysfunction. A prior study showed that Interleukin-6 (IL-6), a cytokine associated with obesity, can induce oxidative stress and endothelial dysfunction by upregulating angiotensin II type 1 receptor (166). In addition, a recent study showed that Olmesartan, an angiotensin II type 1 receptor blocker (ARB)

significantly suppressed high-fat diet induced vascular endothelial dysfunction and disruption of eNOS in mice (142). Thus, future studies may test the therapeutic benefits of ARBs and other novel therapies on high-fat diet induced cardiac dysfunction in mice.

A prior study showed a shift in myocardial substrate utilization in a genetic mouse model of obesity (20). They showed decreased glucose oxidation and increased fatty acid oxidation in the hearts of obese mice and they also showed that this cardiac metabolic shift preceded the other cardiac abnormalities. Thus, the shift in cardiac metabolism may play a critical role in the pathogenesis of obesity related cardiomyopathy. Hence, future studies may use micro-PET with MRI in mice fed a high-fat diet to assess cardiac metabolism and to investigate the underlying mechanisms.

Appendix: List of Publications

PUBLICATIONS:

1. **Naresh N.K.**, Chen X., Moran E.M., Tian Y., French B.A., Epstein F.H.: Repeatability and Variability of Cardiac Perfusion Imaging Techniques for Mice: Comparison of Arterial Spin Labeling and First-pass Contrast-enhanced MRI. *In Preparation*.

2. **Naresh N.K.**, Butcher J.T., Lye J., Chen X., Isakson B.E., Annex B.H., Epstein F.H.: Cardiac MR Detects the Progression of Impaired Myocardial Perfusion Reserve and LV hypertrophy in a Mouse Model of Obesity-Related Cardiomyopathy. *In Preparation*.

3. **Naresh N.K.**, Chen X., Roy R.J., Antkowiak P.F., Annex B.H., Epstein F.H.: Accelerated dual-contrast first-pass perfusion MRI of the mouse heart: Development and application to diet-induced obese mice. Magnetic Resonance in Medicine 2014, DOI: 10.1002/mrm.25238.

4. **Naresh N.K.**, Xu Y, Klibanov A.L., Vandsburger M.H., Meyer C.H., Leor J, Kramer C.M., French B.A. and Epstein F.H.: Monocyte and/or macrophage infiltration of heart after myocardial infarction: MR imaging by using T1-shortening liposomes. Radiology 2012 Aug, 264(2):428-35.
   Finalist for Alexander Margulis Award for Scientific Excellence 2013

5. **Naresh N.K**., Ben-Mordechai T., Leor J, Epstein F.H.: Molecular Imaging of Healing After Myocardial Infarction. Current Cardiovascular Imaging Reports 2010, 4(1): 63-76.

ORAL ABSTRACTS:

1. **Naresh N.K.**, Chen X., Roy R.J., Annex B.H., Epstein F.H.: Cardiac MR Detects Impaired Myocardial Perfusion Reserve and Left-ventricular Hypertrophy in C57Bl/6 Mice Fed a High-Fat Diet. Society for Cardiovascular Magnetic Resonance 2013.

2. **Naresh N.K.**, Chen X., Antkowiak P.F., Xu Y., French B.A., Epstein F.H.: Accelerated Dual-contrast Quantitative First-pass Perfusion MRI of the Mouse Heart with Compressed Sensing. Journal of Cardiovascular Magnetic Resonance 2013; 15(Suppl 1): W17

3. **Naresh N.K.**, Chen X., Antkowiak P.F., Roy R.J. and Epstein F.H.: First-pass MRI detects reduced myocardial perfusion reserve in ApoE$^{-/-}$ mice on a high-cholesterol diet. Proceedings of International Society of Magnetic Resonance in Medicine 2013.

POSTERS:

1. **Naresh N.K.**, Chen X., Antkowiak P.F., French B.A., Epstein F.H.: Compressed-Sensing Accelerated, Dual-contrast, Quantitative First-pass Perfusion MRI of the Mouse Heart. Circulation 2013; 128: A14838.

2. **Naresh N.K.**, Chen X., Carrick J.V., Antkowiak P.F., Roy R.J., Annex B.H., Epstein F.H.: First-pass MRI Reveals Distinct Mechanisms for Reduced

Myocardial Perfusion Reserve Between ApoE-/- Mice on a High-cholesterol Diet and C57Bl/6 Mice on a High-fat Diet. Circulation 2013; 128: A13298.

3. **Naresh N.K.**, Chen X., Antkowiak P.F., Epstein F.H.: Quantitative first-pass perfusion MRI of the mouse heart: data acquisition, reconstruction, and analysis strategies. Journal of Nuclear Medicine 2012; 53 (4): p669. (Won first place in Young Investigator Travel Awards)

4. **Naresh N.K.**, Klibanov A.L., Vandsburger M.H., Leor J., Xu Y., French B.A. and Epstein F.H. : Post-infarct Macrophage Tracking Using MRI and a T1-shortening Contrast Agent: Correction For T1-lengthening Due To Infarct-related Edema. Circulation 2011; 124: A15648.

5. **Naresh N.K.**, Klibanov A.L., Vandsburger M.H., Leor J., Xu Y., French B.A. and Epstein F.H.: Serial Quantitative MRI of Post-Infarct Macrophage Infiltration of the Mouse Heart Using Gd-Liposomes and R1-Mapping. Proceedings of International Society of Magnetic Resonance in Medicine 2011.

6. **Naresh N.K**., Vandsburger M.H., Klibanov A.L., Beyers R.J., Antkowiak P., Xu Y., Smith R.S., French B.A. and Epstein F.H.: Serial Quantitative Cellular MRI of Macrophage Infiltration in the Post-Infarct Heart Using T_1-Mapping and Gd-Liposomes. Circulation 2010, 122:A17344.

7. Naresh N.K., Vandsburger M.H., Klibanov A.L., Antkowiak P., Xu Y., French B.A. and Epstein F.H.: T_1 mapping of the heart with cardio-respiratory-gated Look-Locker MRI quantifies T_1 shortening due to Gd-labeled macrophage infiltration after acute myocardial infarction. Proceedings of International Society of Magnetic Resonance in Medicine 2010.

References

1. Di Carli M, Czernin J, Hoh CK, Gerbaudo VH, Brunken RC, Huang SC, Phelps ME, Schelbert HR. Relation among stenosis severity, myocardial blood flow, and flow reserve in patients with coronary artery disease. Circulation 1995;91(7):1944-1951.

2. Patel AR, Antkowiak PF, Nandalur KR, West AM, Salerno M, Arora V, Christopher J, Epstein FH, Kramer CM. Assessment of Advanced Coronary Artery DiseaseAdvantages of Quantitative Cardiac Magnetic Resonance Perfusion Analysis. Journal of the American College of Cardiology 2010;56(7):561-569.

3. Marzilli M, Merz CN, Boden WE, Bonow RO, Capozza PG, Chilian WM, DeMaria AN, Guarini G, Huqi A, Morrone D, Patel MR, Weintraub WS. Obstructive coronary atherosclerosis and ischemic heart disease: an elusive link! J Am Coll Cardiol 2012;60(11):951-956.

4. Lin F, Shaw LJ, Berman DS, Callister TQ, Weinsaft JW, Wong FJ, Szulc M, Tandon V, Okin PM, Devereux RB, Min JK. Multidetector computed tomography coronary artery plaque predictors of stress-induced myocardial ischemia by SPECT. Atherosclerosis 2008;197(2):700-709.

5. Reis SE, Holubkov R, Smith AJC, Kelsey SF, Sharaf BL, Reichek N, Rogers WJ, Merz CNB, Sopko G, Pepine CJ. Coronary microvascular dysfunction is highly prevalent in women with chest pain in the absence of coronary artery disease: Results from the NHLBI WISE study. American Heart Journal 2001;141(5):735-741.

6.   Murthy VL, Naya M, Foster CR, Gaber M, Hainer J, Klein J, Dorbala S, Blankstein R, Di Carli MF. Association between coronary vascular dysfunction and cardiac mortality in patients with and without diabetes mellitus. Circulation 2012;126(15):1858-1868.

7.   Di Carli MF, Charytan D, McMahon GT, Ganz P, Dorbala S, Schelbert HR. Coronary circulatory function in patients with the metabolic syndrome. J Nucl Med 2011;52(9):1369-1377.

8.   Schindler TH, Cardenas J, Prior JO, Facta AD, Kreissl MC, Zhang XL, Sayre J, Dahlbom M, Licinio J, Schelbert HR. Relationship between increasing body weight, insulin resistance, inflammation, adipocytokine leptin, and coronary circulatory function. J Am Coll Cardiol 2006;47(6):1188-1195.

9.   Barlow SE. Expert committee recommendations regarding the prevention, assessment, and treatment of child and adolescent overweight and obesity: summary report. Pediatrics 2007;120 Suppl 4:S164-192.

10.   Ng M, Fleming T, Robinson M, Thomson B, Graetz N, Margono C, Mullany EC, Biryukov S, Abbafati C, Abera SF, Abraham JP, Abu-Rmeileh NME, Achoki T, AlBuhairan FS, Alemu ZA, Alfonso R, Ali MK, Ali R, Guzman NA, Ammar W, Anwari P, Banerjee A, Barquera S, Basu S, Bennett DA, Bhutta Z, Blore J, Cabral N, Nonato IC, Chang J-C, Chowdhury R, Courville KJ, Criqui MH, Cundiff DK, Dabhadkar KC, Dandona L, Davis A, Dayama A, Dharmaratne SD, Ding EL, Durrani AM, Esteghamati A, Farzadfar F, Fay DFJ, Feigin VL, Flaxman A, Forouzanfar MH, Goto A, Green MA, Gupta R, Hafezi-Nejad N, Hankey GJ, Harewood HC, Havmoeller R, Hay S, Hernandez L, Husseini A, Idrisov BT, Ikeda

N, Islami F, Jahangir E, Jassal SK, Jee SH, Jeffreys M, Jonas JB, Kabagambe EK, Khalifa SEAH, Kengne AP, Khader YS, Khang Y-H, Kim D, Kimokoti RW, Kinge JM, Kokubo Y, Kosen S, Kwan G, Lai T, Leinsalu M, Li Y, Liang X, Liu S, Logroscino G, Lotufo PA, Lu Y, Ma J, Mainoo NK, Mensah GA, Merriman TR, Mokdad AH, Moschandreas J, Naghavi M, Naheed A, Nand D, Narayan KMV, Nelson EL, Neuhouser ML, Nisar MI, Ohkubo T, Oti SO, Pedroza A, Prabhakaran D, Roy N, Sampson U, Seo H, Sepanlou SG, Shibuya K, Shiri R, Shiue I, Singh GM, Singh JA, Skirbekk V, Stapelberg NJC, Sturua L, Sykes BL, Tobias M, Tran BX, Trasande L, Toyoshima H, van de Vijver S, Vasankari TJ, Veerman JL, Velasquez-Melendez G, Vlassov VV, Vollset SE, Vos T, Wang C, Wang X, Weiderpass E, Werdecker A, Wright JL, Yang YC, Yatsuya H, Yoon J, Yoon S-J, Zhao Y, Zhou M, Zhu S, Lopez AD, Murray CJL, Gakidou E. Global, regional, and national prevalence of overweight and obesity in children and adults during 1980–2013: a systematic analysis for the Global Burden of Disease Study 2013. The Lancet;384(9945):766-781.

11. Flegal KM, Kit BK, Orpana H, Graubard BI. Association of all-cause mortality with overweight and obesity using standard body mass index categories: a systematic review and meta-analysis. Jama 2013;309(1):71-82.

12. Jiang J, Ahn J, Huang WY, Hayes RB. Association of obesity with cardiovascular disease mortality in the PLCO trial. Prev Med 2013;57(1):60-64.

13. Wong C, Marwick TH. Obesity cardiomyopathy: pathogenesis and pathophysiology. Nat Clin Pract Cardiovasc Med 2007;4(8):436-443.

14. Smith HL, Willius FA. Adiposity of the heart: A clinical and pathologic study of one hundred and thirty-six obese patients. Archives of Internal Medicine 1933;52(6):911-931.

15. Amad KH, Brennan JC, Alexander JK. The cardiac pathology of chronic exogenous obesity. Circulation 1965;32(5):740-745.

16. Hubert HB, Feinleib M, McNamara PM, Castelli WP. Obesity as an independent risk factor for cardiovascular disease: a 26-year follow-up of participants in the Framingham Heart Study. Circulation 1983;67(5):968-977.

17. Kenchaiah S, Evans JC, Levy D, Wilson PW, Benjamin EJ, Larson MG, Kannel WB, Vasan RS. Obesity and the risk of heart failure. N Engl J Med 2002;347(5):305-313.

18. Abel ED, Litwin SE, Sweeney G. Cardiac remodeling in obesity. Physiol Rev 2008;88(2):389-419.

19. Wong C, Marwick TH. Obesity cardiomyopathy: pathogenesis and pathophysiology. Nat Clin Pract Cardiovasc Med 2007;4(8):436-443.

20. Buchanan J, Mazumder PK, Hu P, Chakrabarti G, Roberts MW, Yun UJ, Cooksey RC, Litwin SE, Abel ED. Reduced cardiac efficiency and altered substrate metabolism precedes the onset of hyperglycemia and contractile dysfunction in two mouse models of insulin resistance and obesity. Endocrinology 2005;146(12):5341-5349.

21. Christoffersen C, Bollano E, Lindegaard ML, Bartels ED, Goetze JP, Andersen CB, Nielsen LB. Cardiac lipid accumulation associated with diastolic dysfunction in obese mice. Endocrinology 2003;144(8):3483-3490.

22. Kalupahana NS, Moustaid-Moussa N. The renin-angiotensin system: a link between obesity, inflammation and insulin resistance. Obes Rev 2012;13(2):136-149.

23. Coelho-Filho OR, Rickers C, Kwong RY, Jerosch-Herold M. MR myocardial perfusion imaging. Radiology 2013;266(3):701-715.

24. Murthy VL, Naya M, Foster CR, Hainer J, Gaber M, Di Carli G, Blankstein R, Dorbala S, Sitek A, Pencina MJ, Di Carli MF. Improved cardiac risk assessment with noninvasive measures of coronary flow reserve. Circulation 2011;124(20):2215-2224.

25. Anagnostopoulos C, Almonacid A, El Fakhri G, Curillova Z, Sitek A, Roughton M, Dorbala S, Popma JJ, Di Carli MF. Quantitative relationship between coronary vasodilator reserve assessed by 82Rb PET imaging and coronary artery stenosis severity. Eur J Nucl Med Mol Imaging 2008;35(9):1593-1601.

26. Beanlands RS, Muzik O, Melon P, Sutor R, Sawada S, Muller D, Bondie D, Hutchins GD, Schwaiger M. Noninvasive quantification of regional myocardial flow reserve in patients with coronary atherosclerosis using nitrogen-13 ammonia positron emission tomography. Determination of extent of altered vascular reactivity. J Am Coll Cardiol 1995;26(6):1465-1475.

27. Uren NG, Melin JA, De Bruyne B, Wijns W, Baudhuin T, Camici PG. Relation between myocardial blood flow and the severity of coronary-artery stenosis. N Engl J Med 1994;330(25):1782-1788.

28. De Bruyne B, Hersbach F, Pijls NH, Bartunek J, Bech JW, Heyndrickx GR, Gould KL, Wijns W. Abnormal epicardial coronary resistance in patients with diffuse

atherosclerosis but "Normal" coronary angiography. Circulation 2001;104(20):2401-2406.

29.   Fujiwara M, Tamura T, Yoshida K, Nakagawa K, Nakao M, Yamanouchi M, Shikama N, Himi T, Masuda Y. Coronary flow reserve in angiographically normal coronary arteries with one-vessel coronary artery disease without traditional risk factors. Eur Heart J 2001;22(6):479-487.

30.   Johnson BD, Shaw LJ, Buchthal SD, Bairey Merz CN, Kim HW, Scott KN, Doyle M, Olson MB, Pepine CJ, den Hollander J, Sharaf B, Rogers WJ, Mankad S, Forder JR, Kelsey SF, Pohost GM. Prognosis in women with myocardial ischemia in the absence of obstructive coronary disease: results from the National Institutes of Health-National Heart, Lung, and Blood Institute-Sponsored Women's Ischemia Syndrome Evaluation (WISE). Circulation 2004;109(24):2993-2999.

31.   Suzuki H, Takeyama Y, Koba S, Suwa Y, Katagiri T. Small vessel pathology and coronary hemodynamics in patients with microvascular angina. Int J Cardiol 1994;43(2):139-150.

32.   Vaccarino V, Badimon L, Corti R, de Wit C, Dorobantu M, Hall A, Koller A, Marzilli M, Pries A, Bugiardini R. Ischaemic heart disease in women: are there sex differences in pathophysiology and risk factors? Position paper from the working group on coronary pathophysiology and microcirculation of the European Society of Cardiology. Cardiovasc Res 2011;90(1):9-17.

33.   Salerno M, Kramer CM. Advances in parametric mapping with CMR imaging. JACC Cardiovasc Imaging 2013;6(7):806-822.

34.   Gerber BL, Raman SV, Nayak K, Epstein FH, Ferreira P, Axel L, Kraitchman DL. Myocardial first-pass perfusion cardiovascular magnetic resonance: history, theory, and current state of the art. J Cardiovasc Magn Reson 2008;10:18.

35.   Kostler H, Ritter C, Lipp M, Beer M, Hahn D, Sandstede J. Prebolus quantitative MR heart perfusion imaging. Magn Reson Med 2004;52(2):296-299.

36.   Christian TF, Rettmann DW, Aletras AH, Liao SL, Taylor JL, Balaban RS, Arai AE. Absolute myocardial perfusion in canines measured by using dual-bolus first-pass MR imaging. Radiology 2004;232(3):677-684.

37.   Kim D, Axel L. Multislice, dual-imaging sequence for increasing the dynamic range of the contrast-enhanced blood signal and CNR of myocardial enhancement at 3T. J Magn Reson Imaging 2006;23(1):81-86.

38.   Cernicanu A, Axel L. Theory-based signal calibration with single-point T1 measurements for first-pass quantitative perfusion MRI studies. Acad Radiol 2006;13(6):686-693.

39.   Nagel E, Klein C, Paetsch I, Hettwer S, Schnackenburg B, Wegscheider K, Fleck E. Magnetic resonance perfusion measurements for the noninvasive detection of coronary artery disease. Circulation 2003;108(4):432-437.

40.   Jerosch-Herold M. Quantification of myocardial perfusion by cardiovascular magnetic resonance. J Cardiovasc Magn Reson 2010;12:57.

41.   Jerosch-Herold M, Wilke N, Stillman AE. Magnetic resonance quantification of the myocardial perfusion reserve with a Fermi function model for constrained deconvolution. Med Phys 1998;25(1):73-84.

42. Jerosch-Herold M, Swingen C, Seethamraju RT. Myocardial blood flow quantification with MRI by model-independent deconvolution. Med Phys 2002;29(5):886-897.

43. Keeling SL, Kogler T, Stollberger R. Deconvolution for DCE-MRI using an exponential approximation basis. Med Image Anal 2009;13(1):80-90.

44. Neyran B, Janier MF, Casali C, Revel D, Canet Soulas EP. Mapping myocardial perfusion with an intravascular MR contrast agent: robustness of deconvolution methods at various blood flows. Magn Reson Med 2002;48(1):166-179.

45. Edelman RR, Siewert B, Darby DG, Thangaraj V, Nobre AC, Mesulam MM, Warach S. Qualitative mapping of cerebral blood flow and functional localization with echo-planar MR imaging and signal targeting with alternating radio frequency. Radiology 1994;192(2):513-520.

46. Wong EC, Buxton RB, Frank LR. Implementation of quantitative perfusion imaging techniques for functional brain mapping using pulsed arterial spin labeling. NMR Biomed 1997;10(4-5):237-249.

47. Kim SG. Quantification of relative cerebral blood flow change by flow-sensitive alternating inversion recovery (FAIR) technique: application to functional mapping. Magn Reson Med 1995;34(3):293-301.

48. Kwong KK, Chesler DA, Weisskoff RM, Donahue KM, Davis TL, Ostergaard L, Campbell TA, Rosen BR. MR perfusion studies with T1-weighted echo planar imaging. Magn Reson Med 1995;34(6):878-887.

49.   Golay X, Stuber M, Pruessmann KP, Meier D, Boesiger P. Transfer insensitive

        labeling technique (TILT): application to multislice functional perfusion imaging. J

        Magn Reson Imaging 1999;9(3):454-461.

50.   Williams DS, Detre JA, Leigh JS, Koretsky AP. Magnetic resonance imaging of

        perfusion using spin inversion of arterial water. Proc Natl Acad Sci U S A

        1992;89(1):212-216.

51.   Bauer WR, Hiller KH, Roder F, Rommel E, Ertl G, Haase A. Magnetization

        exchange in capillaries by microcirculation affects diffusion-controlled spin-

        relaxation: a model which describes the effect of perfusion on relaxation

        enhancement by intravascular contrast agents. Magn Reson Med 1996;35(1):43-

        55.

52.   Belle V, Kahler E, Waller C, Rommel E, Voll S, Hiller KH, Bauer WR, Haase A. In

        vivo quantitative mapping of cardiac perfusion in rats using a noninvasive MR

        spin-labeling method. J Magn Reson Imaging 1998;8(6):1240-1245.

53.   Buxton RB, Frank LR, Wong EC, Siewert B, Warach S, Edelman RR. A general

        kinetic model for quantitative perfusion imaging with arterial spin labeling. Magn

        Reson Med 1998;40(3):383-396.

54.   Hrabe J, Lewis DP. Two analytical solutions for a model of pulsed arterial spin

        labeling with randomized blood arrival times. J Magn Reson 2004;167(1):49-55.

55.   Epstein FH. MR in mouse models of cardiac disease. NMR Biomed

        2007;20(3):238-255.

56.   Patten RD, Hall-Porter MR. Small animal models of heart failure: development of

        novel therapies, past and present. Circ Heart Fail 2009;2(2):138-144.

57.   Yutzey KE, Robbins J. Principles of genetic murine models for cardiac disease. Circulation 2007;115(6):792-799.

58.   Zaragoza C, Gomez-Guerrero C, Martin-Ventura JL, Blanco-Colio L, Lavin B, Mallavia B, Tarin C, Mas S, Ortiz A, Egido J. Animal models of cardiovascular diseases. J Biomed Biotechnol 2011;2011:497841.

59.   Lutz TA, Woods SC. Overview of animal models of obesity. Curr Protoc Pharmacol 2012;Chapter 5:Unit5.61.

60.   Dong F, Zhang X, Yang X, Esberg LB, Yang H, Zhang Z, Culver B, Ren J. Impaired cardiac contractile function in ventricular myocytes from leptin-deficient ob/ob obese mice. J Endocrinol 2006;188(1):25-36.

61.   Lowell BB, V SS, Hamann A, Lawitts JA, Himms-Hagen J, Boyer BB, Kozak LP, Flier JS. Development of obesity in transgenic mice after genetic ablation of brown adipose tissue. Nature 1993;366(6457):740-742.

62.   Finck BN, Han X, Courtois M, Aimond F, Nerbonne JM, Kovacs A, Gross RW, Kelly DP. A critical role for PPARα-mediated lipotoxicity in the pathogenesis of diabetic cardiomyopathy: Modulation by dietary fat content. Proceedings of the National Academy of Sciences 2003;100(3):1226-1231.

63.   Klesges RC, Klesges LM, Haddock CK, Eck LH. A longitudinal analysis of the impact of dietary intake and physical activity on weight change in adults. Am J Clin Nutr 1992;55(4):818-822.

64.   Marshall JA, Hamman RF, Baxter J. High-fat, low-carbohydrate diet and the etiology of non-insulin-dependent diabetes mellitus: the San Luis Valley Diabetes Study. Am J Epidemiol 1991;134(6):590-603.

65.   Marshall JA, Hoag S, Shetterly S, Hamman RF. Dietary fat predicts conversion from impaired glucose tolerance to NIDDM. The San Luis Valley Diabetes Study. Diabetes Care 1994;17(1):50-56.

66.   Miller WC, Lindeman AK, Wallace J, Niederpruem M. Diet composition, energy intake, and exercise in relation to body fat in men and women. Am J Clin Nutr 1990;52(3):426-430.

67.   Winzell MS, Ahren B. The high-fat diet-fed mouse: a model for studying mechanisms and treatment of impaired glucose tolerance and type 2 diabetes. Diabetes 2004;53 Suppl 3:S215-219.

68.   Hariri N, Thibault L. High-fat diet-induced obesity in animal models. Nutr Res Rev 2010;23(2):270-299.

69.   Vandsburger MH, Epstein FH. Emerging MRI methods in translational cardiovascular research. J Cardiovasc Transl Res 2011;4(4):477-492.

70.   Berr SS, Roy RJ, French BA, Yang Z, Gilson W, Kramer CM, Epstein FH. Black blood gradient echo cine magnetic resonance imaging of the mouse heart. Magn Reson Med 2005;53(5):1074-1079.

71.   Gilson WD, Yang Z, French BA, Epstein FH. Complementary displacement-encoded MRI for contrast-enhanced infarct detection and quantification of myocardial function in mice. Magn Reson Med 2004;51(4):744-752.

72.   Gilson WD, Yang Z, French BA, Epstein FH. Measurement of myocardial mechanics in mice before and after infarction using multislice displacement-encoded MRI with 3D motion encoding. Am J Physiol Heart Circ Physiol 2005;288(3):H1491-1497.

73.   Gilson WD, Epstein FH, Yang Z, Xu Y, Prasad KM, Toufektsian MC, Laubach
        VE, French BA. Borderzone contractile dysfunction is transiently attenuated and
        left ventricular structural remodeling is markedly reduced following reperfused
        myocardial infarction in inducible nitric oxide synthase knockout mice. J Am Coll
        Cardiol 2007;50(18):1799-1807.

74.   Young AA, French BA, Yang Z, Cowan BR, Gilson WD, Berr SS, Kramer CM,
        Epstein FH. Reperfused myocardial infarction in mice: 3D mapping of late
        gadolinium enhancement and strain. J Cardiovasc Magn Reson 2006;8(5):685-
        692.

75.   Coelho-Filho OR, Shah RV, Neilan TG, Mitchell R, Moreno H, Jr., Kwong R,
        Jerosch-Herold M. Cardiac magnetic resonance assessment of interstitial
        myocardial fibrosis and cardiomyocyte hypertrophy in hypertensive mice treated
        with spironolactone. J Am Heart Assoc 2014;3(3):e000790.

76.   Beyers RJ, Smith RS, Xu Y, Piras BA, Salerno M, Berr SS, Meyer CH, Kramer
        CM, French BA, Epstein FH. T(2) -weighted MRI of post-infarct myocardial
        edema in mice. Magn Reson Med 2012;67(1):201-209.

77.   Vandsburger MH, Janiczek RL, Xu Y, French BA, Meyer CH, Kramer CM,
        Epstein FH. Improved arterial spin labeling after myocardial infarction in mice
        using cardiac and respiratory gated look-locker imaging with fuzzy C-means
        clustering. Magn Reson Med 2010;63(3):648-657.

78.   Naresh NK, Xu Y, Klibanov AL, Vandsburger MH, Meyer CH, Leor J, Kramer CM,
        French BA, Epstein FH. Monocyte and/or macrophage infiltration of heart after

myocardial infarction: MR imaging by using T1-shortening liposomes. Radiology 2012;264(2):428-435.

79. Himes N, Min JY, Lee R, Brown C, Shea J, Huang X, Xiao YF, Morgan JP, Burstein D, Oettgen P. In vivo MRI of embryonic stem cells in a mouse model of myocardial infarction. Magn Reson Med 2004;52(5):1214-1219.

80. Vandsburger MH, French BA, Kramer CM, Zhong X, Epstein FH. Displacement-encoded and manganese-enhanced cardiac MRI reveal that nNOS, not eNOS, plays a dominant role in modulating contraction and calcium influx in the mammalian heart. Am J Physiol Heart Circ Physiol 2012;302(2):H412-419.

81. Ruff J, Wiesmann F, Hiller KH, Voll S, von Kienlin M, Bauer WR, Rommel E, Neubauer S, Haase A. Magnetic resonance microimaging for noninvasive quantification of myocardial function and mass in the mouse. Magn Reson Med 1998;40(1):43-48.

82. Epstein FH, Yang Z, Gilson WD, Berr SS, Kramer CM, French BA. MR tagging early after myocardial infarction in mice demonstrates contractile dysfunction in adjacent and remote regions. Magn Reson Med 2002;48(2):399-403.

83. Bove CM, Gilson WD, Scott CD, Epstein FH, Yang Z, Dimaria JM, Berr SS, French BA, Bishop SP, Kramer CM. The angiotensin II type 2 receptor and improved adjacent region function post-MI. J Cardiovasc Magn Reson 2005;7(2):459-464.

84. Kim D, Gilson WD, Kramer CM, Epstein FH. Myocardial tissue tracking with two-dimensional cine displacement-encoded MR imaging: development and initial evaluation. Radiology 2004;230(3):862-871.

85.   Zhong X, Helm PA, Epstein FH. Balanced multipoint displacement encoding for DENSE MRI. Magn Reson Med 2009;61(4):981-988.

86.   Zhong X, Spottiswoode BS, Meyer CH, Kramer CM, Epstein FH. Imaging three-dimensional myocardial mechanics using navigator-gated volumetric spiral cine DENSE MRI. Magn Reson Med 2010;64(4):1089-1097.

87.   Zhong X, Gibberman LB, Spottiswoode BS, Gilliam AD, Meyer CH, French BA, Epstein FH. Comprehensive cardiovascular magnetic resonance of myocardial mechanics in mice using three-dimensional cine DENSE. J Cardiovasc Magn Reson 2011;13:83.

88.   Spottiswoode BS, Zhong X, Lorenz CH, Mayosi BM, Meintjes EM, Epstein FH. Motion-guided segmentation for cine DENSE MRI. Med Image Anal 2009;13(1):105-115.

89.   Gilliam AD, Epstein FH. Automated motion estimation for 2-D cine DENSE MRI. IEEE Trans Med Imaging 2012;31(9):1669-1681.

90.   Lustig M, Donoho D, Pauly JM. Sparse MRI: The application of compressed sensing for rapid MR imaging. Magn Reson Med 2007;58(6):1182-1195.

91.   Schneider JE, Lanz T, Barnes H, Stork LA, Bohl S, Lygate CA, Ordidge RJ, Neubauer S. Accelerated cardiac magnetic resonance imaging in the mouse using an eight-channel array at 9.4 Tesla. Magn Reson Med 2011;65(1):60-70.

92.   Coolen BF, Moonen RP, Paulis LE, Geelen T, Nicolay K, Strijkers GJ. Mouse myocardial first-pass perfusion MR imaging. Magn Reson Med 2010;64(6):1658-1663.

93.   van Nierop BJ, Coolen BF, Dijk WJ, Hendriks AD, de Graaf L, Nicolay K, Strijkers GJ. Quantitative first-pass perfusion MRI of the mouse myocardium. Magn Reson Med 2013;69(6):1735-1744.

94.   Makowski M, Jansen C, Webb I, Chiribiri A, Nagel E, Botnar R, Kozerke S, Plein S. First-pass contrast-enhanced myocardial perfusion MRI in mice on a 3-T clinical MR scanner. Magn Reson Med 2010;64(6):1592-1598.

95.   Jogiya R, Makowski M, Phinikaridou A, Patel AS, Jansen C, Zarinabad N, Chiribiri A, Botnar R, Nagel E, Kozerke S, Plein S. Hyperemic stress myocardial perfusion cardiovascular magnetic resonance in mice at 3 Tesla: initial experience and validation against microspheres. J Cardiovasc Magn Reson 2013;15(1):62.

96.   Campbell-Washburn AE, Price AN, Wells JA, Thomas DL, Ordidge RJ, Lythgoe MF. Cardiac arterial spin labeling using segmented ECG-gated Look-Locker FAIR: variability and repeatability in preclinical studies. Magn Reson Med 2013;69(1):238-247.

97.   Campbell-Washburn AE, Zhang H, Siow BM, Price AN, Lythgoe MF, Ordidge RJ, Thomas DL. Multislice cardiac arterial spin labeling using improved myocardial perfusion quantification with simultaneously measured blood pool input function. Magn Reson Med 2012.

98.   Kober F, Iltis I, Cozzone PJ, Bernard M. Myocardial blood flow mapping in mice using high-resolution spin labeling magnetic resonance imaging: influence of ketamine/xylazine and isoflurane anesthesia. Magn Reson Med 2005;53(3):601-606.

99. Nahrendorf M, Streif JU, Hiller KH, Hu K, Nordbeck P, Ritter O, Sosnovik D, Bauer L, Neubauer S, Jakob PM, Ertl G, Spindler M, Bauer WR. Multimodal functional cardiac MRI in creatine kinase-deficient mice reveals subtle abnormalities in myocardial perfusion and mechanics. Am J Physiol Heart Circ Physiol 2006;290(6):H2516-2521.

100. Streif JU, Nahrendorf M, Hiller KH, Waller C, Wiesmann F, Rommel E, Haase A, Bauer WR. In vivo assessment of absolute perfusion and intracapillary blood volume in the murine myocardium by spin labeling magnetic resonance imaging. Magn Reson Med 2005;53(3):584-592.

101. Troalen T, Capron T, Cozzone PJ, Bernard M, Kober F. Cine-ASL: a steady-pulsed arterial spin labeling method for myocardial perfusion mapping in mice. Part I. Experimental study. Magn Reson Med 2013;70(5):1389-1398.

102. Vandsburger MH, French BA, Helm PA, Roy RJ, Kramer CM, Young AA, Epstein FH. Multi-parameter in vivo cardiac magnetic resonance imaging demonstrates normal perfusion reserve despite severely attenuated beta-adrenergic functional response in neuronal nitric oxide synthase knockout mice. Eur Heart J 2007;28(22):2792-2798.

103. Naresh NK, Chen X, Roy RJ, Antkowiak PF, Annex BH, Epstein FH. Accelerated dual-contrast first-pass perfusion MRI of the mouse heart: Development and application to diet-induced obese mice. Magn Reson Med 2014.

104. Campbell-Washburn AE, Zhang H, Siow BM, Price AN, Lythgoe MF, Ordidge RJ, Thomas DL. Multislice cardiac arterial spin labeling using improved myocardial

perfusion quantification with simultaneously measured blood pool input function. Magn Reson Med 2013;70(4):1125-1136.

105. Epstein FH, Naresh NK, Antkowiak PF, Vandsburger MH, Chen X. (Abstract): Quantitative MRI of the Myocardial Microcirculation in Mice using FAIR Look-Locker Arterial Spin Labeling and a Gamma-variate Model of Blood Transit. Proceedings of International Society Magnetic Resonance in Medicine 2011;19(216).

106. Antkowiak P, Janiczek R, Gibberman L, Xu C, Kramer C, Meyer C, French B, Epstein F. Quantitative first-pass perfusion MRI of the mouse heart. Journal of Cardiovascular Magnetic Resonance 2010;12(Suppl 1):M10.

107. Calligaris SD, Lecanda M, Solis F, Ezquer M, Gutierrez J, Brandan E, Leiva A, Sobrevia L, Conget P. Mice long-term high-fat diet feeding recapitulates human cardiovascular alterations: an animal model to study the early phases of diabetic cardiomyopathy. PLoS One 2013;8(4):e60931.

108. Kim D, Cernicanu A, Axel L. B(0) and B(1)-insensitive uniform T(1)-weighting for quantitative, first-pass myocardial perfusion magnetic resonance imaging. Magn Reson Med 2005;54(6):1423-1429.

109. Chen X, Salerno M, Yang Y, Epstein FH. Motion-compensated compressed sensing for dynamic contrast-enhanced MRI using regional spatiotemporal sparsity and region tracking: Block low-rank sparsity with motion-guidance (BLOSM). Magn Reson Med 2013.

110. Lingala SG, Hu Y, DiBella E, Jacob M. Accelerated dynamic MRI exploiting sparsity and low-rank structure: k-t SLR. IEEE Trans Med Imaging 2011;30(5):1042-1054.

111. Al Jaroudi W, Iskandrian AE. Regadenoson: a new myocardial stress agent. J Am Coll Cardiol 2009;54(13):1123-1130.

112. Nunemaker CS, Chen M, Pei H, Kimble SD, Keller SR, Carter JD, Yang Z, Smith KM, Wu R, Bevard MH, Garmey JC, Nadler JL. 12-Lipoxygenase-knockout mice are resistant to inflammatory effects of obesity induced by Western diet. Am J Physiol Endocrinol Metab 2008;295(5):E1065-1075.

113. Rohrer M, Bauer H, Mintorovitch J, Requardt M, Weinmann HJ. Comparison of magnetic properties of MRI contrast media solutions at different magnetic field strengths. Invest Radiol 2005;40(11):715-724.

114. Kim WY, Walker PG, Pedersen EM, Poulsen JK, Oyre S, Houlind K, Yoganathan AP. Left ventricular blood flow patterns in normal subjects: a quantitative analysis by three-dimensional magnetic resonance velocity mapping. J Am Coll Cardiol 1995;26(1):224-238.

115. Janiczek RL, Blackman BR, Roy RJ, Meyer CH, Acton ST, Epstein FH. Three-dimensional phase contrast angiography of the mouse aortic arch using spiral MRI. Magn Reson Med 2011;66(5):1382-1390.

116. Cerqueira MD, Nguyen P, Staehr P, Underwood SR, Iskandrian AE. Effects of age, gender, obesity, and diabetes on the efficacy and safety of the selective A2A agonist regadenoson versus adenosine in myocardial perfusion imaging

integrated ADVANCE-MPI trial results. JACC Cardiovasc Imaging 2008;1(3):307-316.

117. Kramer SP, Powell DK, Haggerty CM, Binkley CM, Mattingly AC, Cassis LA, Epstein FH, Fornwalt BK. Obesity reduces left ventricular strains, torsion, and synchrony in mouse models: a cine displacement encoding with stimulated echoes (DENSE) cardiovascular magnetic resonance study. J Cardiovasc Magn Reson 2013;15:109.

118. Raher MJ, Thibault H, Poh KK, Liu R, Halpern EF, Derumeaux G, Ichinose F, Zapol WM, Bloch KD, Picard MH, Scherrer-Crosbie M. In vivo characterization of murine myocardial perfusion with myocardial contrast echocardiography: validation and application in nitric oxide synthase 3 deficient mice. Circulation 2007;116(11):1250-1257.

119. Richer C, Domergue V, Gervais M, Bruneval P, Giudicelli JF. Fluospheres for cardiovascular phenotyping genetically modified mice. J Cardiovasc Pharmacol 2000;36(3):396-404.

120. Trabold F, Pons S, Hagege AA, Bloch-Faure M, Alhenc-Gelas F, Giudicelli JF, Richer-Giudicelli C, Meneton P. Cardiovascular phenotypes of kinin B2 receptor- and tissue kallikrein-deficient mice. Hypertension 2002;40(1):90-95.

121. Ding S, Wolff SD, Epstein FH. Improved coverage in dynamic contrast-enhanced cardiac MRI using interleaved gradient-echo EPI. Magn Reson Med 1998;39(4):514-519.

122. Salerno M, Sica C, Kramer CM, Meyer CH. Improved first-pass spiral myocardial perfusion imaging with variable density trajectories. Magn Reson Med 2013;70(5):1369-1379.

123. Cannon RO, 3rd. Does coronary endothelial dysfunction cause myocardial ischemia in the absence of obstructive coronary artery disease? Circulation 1997;96(10):3251-3254.

124. Levy BI, Schiffrin EL, Mourad J-J, Agostini D, Vicaut E, Safar ME, Struijker-Boudier HAJ. Impaired Tissue Perfusion: A Pathology Common to Hypertension, Obesity, and Diabetes Mellitus. Circulation 2008;118(9):968-976.

125. Zhang H, Qiao H, Frank RS, Huang B, Propert KJ, Margulies S, Ferrari VA, Epstein JA, Zhou R. Spin-Labeling Magnetic Resonance Imaging Detects Increased Myocardial Blood Flow After Endothelial Cell Transplantation in the Infarcted Heart. Circulation: Cardiovascular Imaging 2012;5(2):210-217.

126. Banquet S, Gomez E, Nicol L, Edwards-Lévy F, Henry J-P, Cao R, Schapman D, Dautreaux B, Lallemand F, Bauer F, Cao Y, Thuillez C, Mulder P, Richard V, Brakenhielm E. Arteriogenic Therapy by Intramyocardial Sustained Delivery of a Novel Growth Factor Combination Prevents Chronic Heart Failure. Circulation 2011;124(9):1059-1069.

127. Hiller K-H, Ruile P, Kraus G, Bauer WR, Waller C. Tissue ACE inhibition improves microcirculation in remote myocardium after coronary stenosis: MR imaging study in rats. Microvascular Research 2010;80(3):484-490.

128. French BA, Li Y, Klibanov AL, Yang Z, Hossack JA. 3D perfusion mapping in post-infarct mice using myocardial contrast echocardiography. Ultrasound in Medicine and Biology;32(6):805-815.

129. Davenport R. The derivation of the gamma-variate relationship for tracer dilution curves. J Nucl Med 1983;24(10):945-948.

130. Harpen MD, Lecklitner ML. Derivation of gamma variate indicator dilution function from simple convective dispersion model of blood flow. Med Phys 1984;11(5):690-692.

131. Thompson HK, Jr., Starmer CF, Whalen RE, McIntosh HD. INDICATOR TRANSIT TIME CONSIDERED AS A GAMMA VARIATE. Circ Res 1964;14:502-515.

132. Chappell MA, Woolrich MW, Kazan S, Jezzard P, Payne SJ, MacIntosh BJ. Modeling dispersion in arterial spin labeling: Validation using dynamic angiographic measurements. Magnetic Resonance in Medicine 2013;69(2):563-570.

133. Williams DS, Detre JA, Leigh JS, Koretsky AP. Magnetic resonance imaging of perfusion using spin inversion of arterial water. Proceedings of the National Academy of Sciences 1992;89(1):212-216.

134. Ishida M, Ichihara T, Nagata M, Ishida N, Takase S, Kurita T, Ito M, Takeda K, Sakuma H. Quantification of myocardial blood flow using model based analysis of first-pass perfusion MRI: extraction fraction of Gd-DTPA varies with myocardial blood flow in human myocardium. Magn Reson Med 2011;66(5):1391-1399.

135. Tong CY, Prato FS, Wisenberg G, Lee TY, Carroll E, Sandler D, Wills J, Drost D. Measurement of the extraction efficiency and distribution volume for Gd-DTPA in normal and diseased canine myocardium. Magn Reson Med 1993;30(3):337-346.

136. Abdurrachim D, Ciapaite J, Wessels B, Nabben M, Luiken JJ, Nicolay K, Prompers JJ. Cardiac diastolic dysfunction in high-fat diet fed mice is associated with lipotoxicity without impairment of cardiac energetics in vivo. Biochim Biophys Acta 2014;1842(10):1525-1537.

137. Pettersson US, Waldén TB, Carlsson P-O, Jansson L, Phillipson M. Female Mice are Protected against High-Fat Diet Induced Metabolic Syndrome and Increase the Regulatory T Cell Population in Adipose Tissue. PLoS ONE 2012;7(9):e46057.

138. Louwe MC, van der Hoorn JW, van den Berg SA, Jukema JW, Romijn JA, van Dijk KW, Rensen PC, Smit JW, Steendijk P. Gender-dependent effects of high-fat lard diet on cardiac function in C57Bl/6J mice. Appl Physiol Nutr Metab 2012;37(2):214-224.

139. Billaud M, Lohman AW, Straub AC, Parpaite T, Johnstone SR, Isakson BE. Characterization of the thoracodorsal artery: morphology and reactivity. Microcirculation 2012;19(4):360-372.

140. Kuo L, Davis MJ, Chilian WM. Endothelium-dependent, flow-induced dilation of isolated coronary arterioles. Am J Physiol 1990;259(4 Pt 2):H1063-1070.

141. Stapleton PA, Minarchick VC, Cumpston AM, McKinney W, Chen BT, Sager TM, Frazer DG, Mercer RR, Scabilloni J, Andrew ME, Castranova V, Nurkiewicz TR.

Impairment of coronary arteriolar endothelium-dependent dilation after multi-walled carbon nanotube inhalation: a time-course study. Int J Mol Sci 2012;13(11):13781-13803.

142. Yamamoto E, Dong YF, Kataoka K, Yamashita T, Tokutomi Y, Matsuba S, Ichijo H, Ogawa H, Kim-Mitsuyama S. Olmesartan prevents cardiovascular injury and hepatic steatosis in obesity and diabetes, accompanied by apoptosis signal regulating kinase-1 inhibition. Hypertension 2008;52(3):573-580.

143. Al Suwaidi J, Higano ST, Holmes JDR, Lennon R, Lerman A. Obesity is independently associated with coronary endothelial dysfunction in patients with normal or mildly diseased coronary arteries. Journal of the American College of Cardiology 2001;37(6):1523-1528.

144. Battiprolu PK, Hojayev B, Jiang N, Wang ZV, Luo X, Iglewski M, Shelton JM, Gerard RD, Rothermel BA, Gillette TG, Lavandero S, Hill JA. Metabolic stress-induced activation of FoxO1 triggers diabetic cardiomyopathy in mice. J Clin Invest 2012;122(3):1109-1118.

145. Bostick B, Habibi J, Ma L, Aroor A, Rehmer N, Hayden MR, Sowers JR. Dipeptidyl peptidase inhibition prevents diastolic dysfunction and reduces myocardial fibrosis in a mouse model of Western diet induced obesity. Metabolism 2014;63(8):1000-1011.

146. Ge F, Hu C, Hyodo E, Arai K, Zhou S, Lobdell Ht, Walewski JL, Homma S, Berk PD. Cardiomyocyte triglyceride accumulation and reduced ventricular function in mice with obesity reflect increased long chain Fatty Acid uptake and de novo Fatty Acid synthesis. J Obes 2012;2012:205648.

147. Ghosh S, Rodrigues B. Cardiac cell death in early diabetes and its modulation by dietary fatty acids. Biochim Biophys Acta 2006;1761(10):1148-1162.

148. Noyan-Ashraf MH, Shikatani EA, Schuiki I, Mukovozov I, Wu J, Li RK, Volchuk A, Robinson LA, Billia F, Drucker DJ, Husain M. A glucagon-like peptide-1 analog reverses the molecular pathology and cardiac dysfunction of a mouse model of obesity. Circulation 2013;127(1):74-85.

149. Qin F, Siwik DA, Luptak I, Hou X, Wang L, Higuchi A, Weisbrod RM, Ouchi N, Tu VH, Calamaras TD, Miller EJ, Verbeuren TJ, Walsh K, Cohen RA, Colucci WS. The polyphenols resveratrol and S17834 prevent the structural and functional sequelae of diet-induced metabolic heart disease in mice. Circulation 2012;125(14):1757-1764, s1751-1756.

150. Turdi S, Kandadi MR, Zhao J, Huff AF, Du M, Ren J. Deficiency in AMP-activated protein kinase exaggerates high fat diet-induced cardiac hypertrophy and contractile dysfunction. J Mol Cell Cardiol 2011;50(4):712-722.

151. Yan J, Young ME, Cui L, Lopaschuk GD, Liao R, Tian R. Increased glucose uptake and oxidation in mouse hearts prevent high fatty acid oxidation but cause cardiac dysfunction in diet-induced obesity. Circulation 2009;119(21):2818-2828.

152. Zibadi S, Vazquez R, Moore D, Larson DF, Watson RR. Myocardial lysyl oxidase regulation of cardiac remodeling in a murine model of diet-induced metabolic syndrome. Am J Physiol Heart Circ Physiol 2009;297(3):H976-982.

153. Burcelin R, Crivelli V, Dacosta A, Roy-Tirelli A, Thorens B. Heterogeneous metabolic adaptation of C57BL/6J mice to high-fat diet. Am J Physiol Endocrinol Metab 2002;282(4):E834-842.

154. Wong C, Marwick TH. Obesity cardiomyopathy: diagnosis and therapeutic implications. Nat Clin Pract Cardiovasc Med 2007;4(9):480-490.

155. Kankaanpaa M, Lehto HR, Parkka JP, Komu M, Viljanen A, Ferrannini E, Knuuti J, Nuutila P, Parkkola R, Iozzo P. Myocardial triglyceride content and epicardial fat mass in human obesity: relationship to left ventricular function and serum free fatty acid levels. J Clin Endocrinol Metab 2006;91(11):4689-4695.

156. Wende AR, Abel ED. Lipotoxicity in the heart. Biochim Biophys Acta 2010;1801(3):311-319.

157. Glenn DJ, Wang F, Nishimoto M, Cruz MC, Uchida Y, Holleran WM, Zhang Y, Yeghiazarians Y, Gardner DG. A murine model of isolated cardiac steatosis leads to cardiomyopathy. Hypertension 2011;57(2):216-222.

158. Zhou YT, Grayburn P, Karim A, Shimabukuro M, Higa M, Baetens D, Orci L, Unger RH. Lipotoxic heart disease in obese rats: implications for human obesity. Proc Natl Acad Sci U S A 2000;97(4):1784-1789.

159. Szczepaniak LS, Dobbins RL, Metzger GJ, Sartoni-D'Ambrosia G, Arbique D, Vongpatanasin W, Unger R, Victor RG. Myocardial triglycerides and systolic function in humans: in vivo evaluation by localized proton spectroscopy and cardiac imaging. Magn Reson Med 2003;49(3):417-423.

160. Tikellis C, Thomas MC, Harcourt BE, Coughlan MT, Pete J, Bialkowski K, Tan A, Bierhaus A, Cooper ME, Forbes JM. Cardiac inflammation associated with a Western diet is mediated via activation of RAGE by AGEs. Am J Physiol Endocrinol Metab 2008;295(2):E323-330.

161. Ouchi N, Shibata R, Walsh K. Cardioprotection by Adiponectin. Trends in Cardiovascular Medicine 2006;16(5):141-146.

162. Ouchi N, Kihara S, Funahashi T, Matsuzawa Y, Walsh K. Obesity, adiponectin and vascular inflammatory disease. Curr Opin Lipidol 2003;14(6):561-566.

163. Shibata R, Ouchi N, Ito M, Kihara S, Shiojima I, Pimentel DR, Kumada M, Sato K, Schiekofer S, Ohashi K, Funahashi T, Colucci WS, Walsh K. Adiponectin-mediated modulation of hypertrophic signals in the heart. Nat Med 2004;10(12):1384-1389.

164. Avogaro A, de Kreutzenberg SV. Mechanisms of endothelial dysfunction in obesity. Clinica Chimica Acta 2005;360(1–2):9-26.

165. Wang H, Luo W, Wang J, Guo C, Wang X, Wolffe SL, Bodary PF, Eitzman DT. Obesity-Induced Endothelial Dysfunction Is Prevented by Deficiency of P-Selectin Glycoprotein Ligand-1. Diabetes 2012;61(12):3219-3227.

166. Wassmann S, Stumpf M, Strehlow K, Schmid A, Schieffer B, Bohm M, Nickenig G. Interleukin-6 induces oxidative stress and endothelial dysfunction by overexpression of the angiotensin II type 1 receptor. Circ Res 2004;94(4):534-541.